学位論文

Measurement of the In-flight Antiproton Annihilation Cross Section on Carbon at 100 MeV/c

(100 MeV/c における反陽子・炭素原子核消滅断面積の測定)

平成 28 年 12 月 博士 (理学) 申請

東京大学大学院理学系研究科
物理学専攻
村上 洋平

Abstract

The ASACUSA collaboration at the Antiproton Decelerator of CERN performed a measurement of the in-flight antiproton ($\overline{\mathrm{p}}$) annihilation cross section on carbon at a momentum of 100 MeV/c for the antiproton. This experiment aims to study anomalous enhancements of antineutron ($\overline{\mathrm{n}}$) annihilation cross sections on C, Al, Cu and Pb nuclei below 500 MeV/c.

We developed a new experimental setup which determined the cross section relative to the elastic scattering cross section. A pulsed beam of 100 MeV/c transversed a carbon foil of thickness $\sim$1 μm, and charged particles emerging from annihilations were detected by plastic scintillation bars. In a different run, we positioned a circler ring downstream of the target. Some antiprotons scattered elastically on the target and annihilated on the frame. The resulting charged particles were detected to determine the elastic scattering cross section. By comparing the numbers of detected particles with and without the frame, the annihilation cross section was derived.

To monitor the relative intensity of the beam to normalize the signals with and without the ring, we developed a Cherenkov counter with photodiode readout. We measured the photon yields of five crystals and selected lead fluoride crystals, which had a high refractive index of 1.84. Avalanche photodiodes were used to minimize the background caused by the nuclear counter effect. The detector was placed close to the beam dump, and measured the relative intensities of the beam with a precision of $\sim 2\%$.

The $\overline{\mathrm{p}}$-annihilation cross section on carbon targets at a momentum of 100 MeV/c was determined as 1.21 ± 0.31 barn. The result is consistent with a calculation based on the generalized optical potential within 1σ, and so no large enhancement like for the $\overline{\mathrm{n}}$ data was observed. The mass dependence of the cross sections at 100 MeV/c was studied using the past experimental data of Ni, Sn and Pt. The results follow theoretical calculations.

Contents

List of Figures

List of Tables

Chapter 1

Introduction

In this thesis, a measurement of the annihilation cross section of antiprotons on carbon targets at an antiproton momentum of 100 MeV/c is described. This data will be compared with those of antineutron annihilations in the same momentum region [1]. In this chapter, the $\overline{\mathrm{n}}$-annihilation cross sections, past experiments of $\overline{\mathrm{p}}$-annihilation cross sections and theoretical calculations used to describe them are presented.

1.1 Annihilation cross sections of antinucleon

Antiprotons ($\overline{\mathrm{p}}$) and antineutrons ($\overline{\mathrm{n}}$) are antiparticles of protons and neutrons. Past experiments show that when antiprotons and antineutrons strike a target nucleus, they annihilate with surface nucleons, in a way they makes the target behaves like a complete black disk [1]. The antinucleon-annihilation cross sections have been used to construct optical potentials between them [2].

Recent studies revealed that the $\overline{\mathrm{n}}$-annihilation cross sections on some nuclei (C, Al, Cu and Pb) at momenta $\sim$ 100 MeV/c show anomalous behaviors when compared to theoretical calculations of $\overline{\mathrm{p}}$-annihilation cross sections. Due to lack of the enhancement caused by Coulomb focusing effects, the $\overline{\mathrm{p}}$-annihilation cross sections were expected to be consistently larger than the $\overline{\mathrm{n}}$-annihilation cross sections for the same target and energy of the incident particle. However the $\overline{\mathrm{n}}$-cross sections measured by the OBELIX experiment [3] were larger than the expected values based on the generalized optical potential model [2], and in fact behaved like $\overline{\mathrm{p}}$-annihilation

cross sections. In Fig. 1.1 the black circles represent the $\overline{\mathrm{n}}$-annihilation cross sections, dashed and solid lines represent theoretical calculations for $\overline{\mathrm{p}}$ and $\overline{\mathrm{n}}$-annihilation cross sections. The difference between the experimental data and $\overline{\mathrm{n}}$-calculations were more than 5σ, the data was closer to the $\overline{\mathrm{p}}$-calculations. It has been discussed whether the enhancement had some physics reason or was caused by other experimental issues, but so far this deviation is not understood.

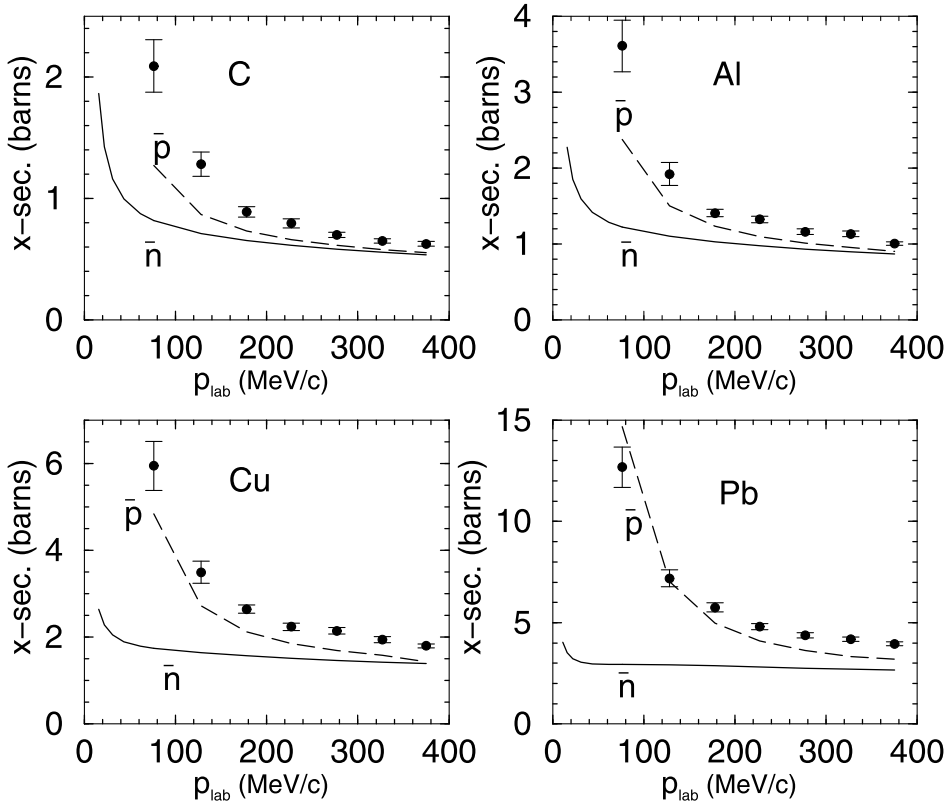

FIGURE 1.1: Annihilation cross sections of antineutrons on C, Al, Cu and Pb targets (black circles). Dashed lines indicate theoretical curve of $\overline{\mathrm{p}}$-nuclei annihilation cross sections, solid lines antineutron cross sections. These figures were taken from Ref. [1].

One possible reason for this enhancement is an existence of resonance states. Fig. 1.2 shows experimental data of the antineutron-proton annihilation cross section in the momentum region below 450 MeV/c [4]. They

measured total (indicated by black rectangle points) and annihilation (indicated by black circler points) cross sections of antineutron on a proton target. Theoretical calculations of the annihilation cross section (solid line) and total cross section (dashed line) are shown together. There is a small excess around 180 MeV/c, which was suspected to be caused by a near-threshold resonance [5]. The existence of such resonance are controversial.

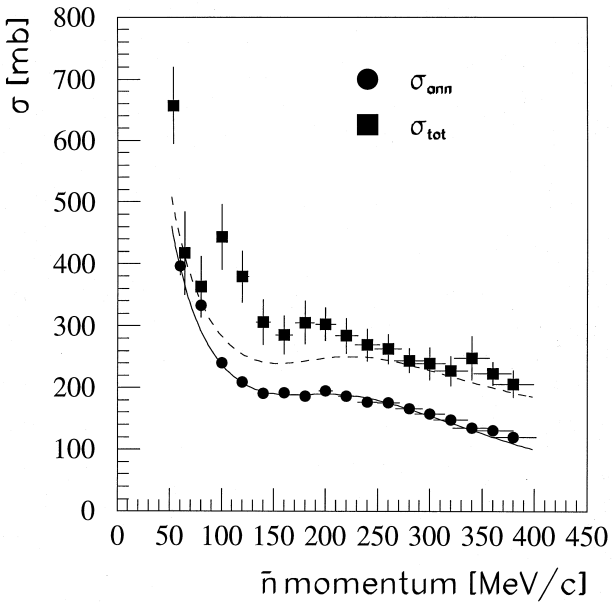

FIGURE 1.2: $\bar{n}$-annihilation cross sections (filled circles) and total gross sections (squares) on proton targets measured by the OBELIX. Theoretical calculations for the annihilation cross section (solid curves) and the the total cross section (dashed curves) are shown together. This figure is taken from Ref. [4].

In cases of heavier nuclei, the annihilations with the surface nucleon were affected by the Fermi motion of the nucleon. The resonance state disappeared and only a broad enhancement appeared to remain, but so far there is no explanation for the continuous enhancement seen in Fig. 1.1. Fig. 1.3 shows the cross sections of antineutrons on Cu, Sn and Pb as a function of the incoming momentum of an antiproton. In order to study the

dependence of cross sections on the momenta $p_{\overline{n}}$, the data were fit with the simple function.

$$\sigma_0 = a + b/p_{\overline{n}} \tag{1.1}$$

where a and b denote some parameters. The function (Fig. 1.3) reproduces the results for Cu, Sn and Pb targets well, and so that the annihilation cross section of antineutrons also obey the $1/v$ law like for antiprotons while we observed broad enhancements in Fig. 1.1.

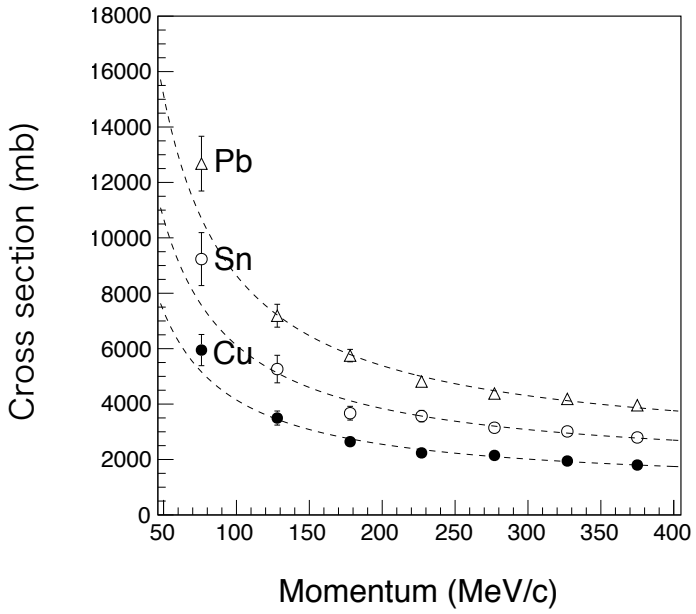

FIGURE 1.3: Cross sections of $\overline{n}$ on Cu, Sn and Pb. The data was fit by Eq. 1.1. This figure is taken from Ref. [3].

The generalized optical potential model used to fit the data of Fig. 1.1 has been used over a wide momentum region, to reproduce the width and shift of the antiproton-nuclei bound states (below the threshold), and scattering and annihilations with nuclei (above threshold) [6]. The $\overline{n}$-anninhilation cross section was obtained by setting the electric charge of the potential to zero. As antiprotons and antineutrons have isoscalar symmetry, it is difficult

to understand why the optical potential cannot reproduce the experimental data of $\overline{\mathrm{n}}$-annihilation cross sections.

1.1.1 Setup of experiments using antineutrons

Since an antineutron has no charge, it can not be transported the antineutrons from a production target of an accelerator facility. Instead a liquid gas target was installed just upstream of experimental apparatus, and antineutrons were produced via the charge exchange reaction,

$$\overline{\mathrm{p}} + \mathrm{p} \rightarrow \overline{\mathrm{n}} + \mathrm{n}. \tag{1.2}$$

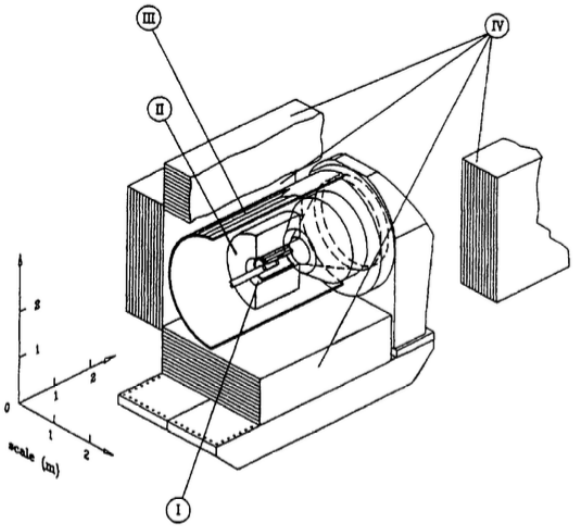

FIGURE 1.4: A schematic view of the OBELIX spectrometer. In order to reconstruct vertex of the annihilation-point, internal (I) and external (III) scintillator barrels, a jet drift chamber (II) and an electromagnetic calorimeter (IV) were used. This figure is taken from Ref. [7].

The measurements using antineutrons were carried out by the OBELIX collaboration at CERN with the experimental setup shown in Fig. 1.4. OBELIX was developed as a general purpose magnetic spectrometer surrounding a solid angle of $\sim 3\pi$ seen from the experimental target. The

emitted antineutrons were tagged by measuring the energy and position of an associated neutron emitted in the reaction of Eqn. 1.2. By calculating two-body kinematics of the reaction, the four-momentum of $\overline{\mathrm{n}}$ was derived. A lead collimator was installed downstream of the LH_2 volume which defined the antineutron beams. The production rate of antineutrons against the incident antiprotons was $\sim 10^{-6}$. Details of the OBELIX experiment are described in Appendix. A. Due to this experimental apparatus, there was difficulty in tracking the emerging particle, and they suffered from low statistics.

1.1.2 Annihilation cross sections of antiprotons

Direct comparisons of experimental $\overline{\mathrm{p}}$- and $\overline{\mathrm{n}}$-annihilation cross sections were performed for only p and Sn targets because these were the only data sets available.

As shown in Fig. 1.5, the $\overline{\mathrm{p}}$-annihilation cross sections on the proton target are consistently larger than the $\overline{\mathrm{n}}$ cross sections at the same momentum. In this region no enhancement of the type shown in Fig. 1.1 was observed.

Among the four target nuclei used for $\overline{\mathrm{n}}$ experiments in Fig. 1.1, the corresponding data for $\overline{\mathrm{p}}$ exists only for Sn (Fig. 1.6). The $\overline{\mathrm{p}}$ cross sections were well described by the theoretical curve, and was smaller than $\overline{\mathrm{n}}$-annihilation cross sections. If the enhancements shown in Fig. 1.1 are real, this implies that $\overline{\mathrm{n}}$-annihilation cross sections are larger than the corresponding $\overline{\mathrm{p}}$-annihilation cross sections for heavier target nuclei, i.e. the behavior inverts.

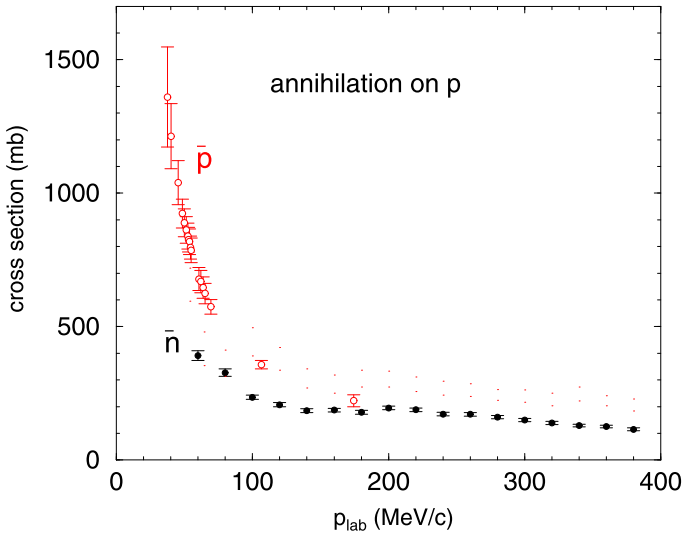

FIGURE 1.5: Annihilation cross sections of antiprotons and antineutrons on proton targets. This figure is taken from Ref. [2].

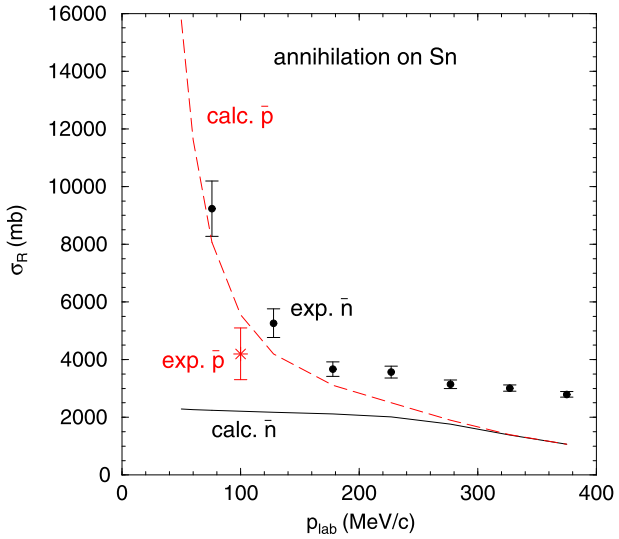

FIGURE 1.6: Annihilation cross section of antiprotons on Sn targets at 100 MeV/c (red star) [8]. Experimental data of antineutrons on Sn (filled circles) [3] are shown together. The dashed curve indicate the result of theoretical calculations of $\overline{\mathrm{p}}$ cross sections, and a solid curve is the one for $\overline{\mathrm{n}}$. This figure is taken from Ref. [1].

1.1.3 Studies using antiprotons

We may summarize the above discussion in the following way.

- The experimental $\overline{\mathrm{n}}$-annihilation cross sections were much (5σ) larger than the theoretical values, which are based on the generalized optical potential of antiprotons in the momentum region from 100 MeV/c to 500 MeV/c. On the other hand the potential reproduced the experimental data at momenta above 1 GeV/c and the region of bound states and nuclei where the total energy was negative.

- Antineutrons must be produced by the charge exchange reaction and require tracking for particle identification.

- Direct comparisons of experimental data of antiprotons and antineutrons were carried out for only two types of targets. The experimental data of $\overline{\mathrm{n}}$-annihilation cross sections were smaller than for the antiprotons with a proton target, while they became larger in the case of a Sn one. This implies that at a certain mass number the $\overline{\mathrm{n}}$-annihilation cross section becomes larger than the antiproton values.

There is a general lack of $\overline{\mathrm{p}}$ experimental data which can be compared with the existing $\overline{\mathrm{n}}$ data. Of particular importance is the measurement of four types of nuclei which should enable the direct comparison with the corresponding experimental data of antineutrons. As the possible enhancement and inversion of $\overline{\mathrm{p}}$ and $\overline{\mathrm{n}}$ annihilation cross sections apparently depends on the mass number, it is necessary to measure them with various nuclei.

1.2 Past measurements of antiproton-nuclei annihilation cross sections

We next review the existing data and theories of antiproton annihilations on various target nuclei.

1.2.1 Past experiments using antiprotons

Measurements of antiproton-nucleus annihilation cross sections were carried out since the 1980s by various methods. The cross sections of of H [9–12], D [13–15], ^{3}He [16], ^{4}He [17] and Ne [18] targets have been measured in the momentum region p > 40 MeV/c at the Low Energy Antiproton Ring (LEAR), where a continuous beam of 10^6 s^{-1} antiprotons was produced.

The annihilation cross section of antiprotons on proton targets have been measured over a wide momentum region from 10 MeV/c to 1 GeV/c. The initial purpose of the experiments was to discover any resonance or bound states of $p\overline{p}$ which relate to new particles, such as glueballs [19, 20]. The experiments counted the number of charged pions emerging from the annihilations in a liquid hydrogen target by using scintillator hodoscopes [9–11], which identified the events by the timings and energy loss of the pions. In the other measurements a streamer chamber was used to detect the charged particles [17].

Measurements of ^{3}He and ^{4}He were carried out using a helium gas target and plastic scintillator hodoscopes which tracked the trajectories of secondary particles emerging from antiproton annihilations in the target [9]. In an other experiment, a drift chamber and stereocamera were used for measurements of the cross sections [13, 16]. Annihilation cross sections of deuterium in the momentum region from 300 to 600 MeV/c were measured using a bubble-chamber [15]. The OBELIX experiment carried out measurements of deuterium targets in the momentum region from 36 to 70 MeV/c [7]. The spectrometer consisted internal and external scintillator barrels, jet drift chamber and an electromagnetic calorimeter to reconstruct the

vertex point of the position of an antiproton-nucleus annihilation. A bubble chamber was also used for the measurement using a deuterium gas target [13].

The annihilation cross section on C, Al and Cu nuclei were measured in the momentum region from 470 to 880 MeV/c [21]. The experiments were carried out in the low-momentum separated beam (K3) produced by the 12-GeV proton synchrotron at the National Laboratory for the High Energy Physics (KEK), BNL and LEAR at CERN.

For these heavier nuclei, the tracking method applied for the measurements of H, ^{3}He, ^{4}He and deuterium could not be used due to the high multiplicities. Therefore transmission methods which compared the incident and transmitted antiprotons were used. In the measurement, the annihilation cross sections were determined by using the relationship, $N_{in}e^{-\rho\sigma_{anni}} = N_{trans}$, where ρ denotes the density of the target. The trajectories of incoming and outgoing charged particles were measured by multi-wire proportional chambers (MWPC's). The outgoing charged particles were also detected by scintillator detectors. A Cherenkov counter surrounding the target was also used.

In the momentum region $\sim$ 500 MeV/c, the cross sections on C, Ca and Pb were measured [22]. Using a magnetic spectrometer called SPES Ⅱ. Inelastic and elastic scattering differential cross sections were measured to construct an optical potential between them. A Schroedinger equation was then solved to derive the cross section.

Using the Antiproton Decelerator (AD) [23], the annihilation cross sections on Mylar, Ni, Sn and Pt were measured at 100 MeV/c by the ASACUSA (Atomic Spectroscopy And Collisions Using Slow Antiproton) in 2011 [8]. The main backgrounds in the momentum region of 100 MeV/c were annihilations of antiprotons at rest in the target. Therefore thin target foils of $\sim 1\ \mu\mathrm{m}$ were used. The foils were installed in a vacuum chamber, and a vertex detector consisting of scintillation fibers was positioned around the vessel and the target. The detector consisted of two cylindrical shells, and

each shells was made of 3 layers of scintillators which tracked the charged particles from antiproton-nucleus annihilations.

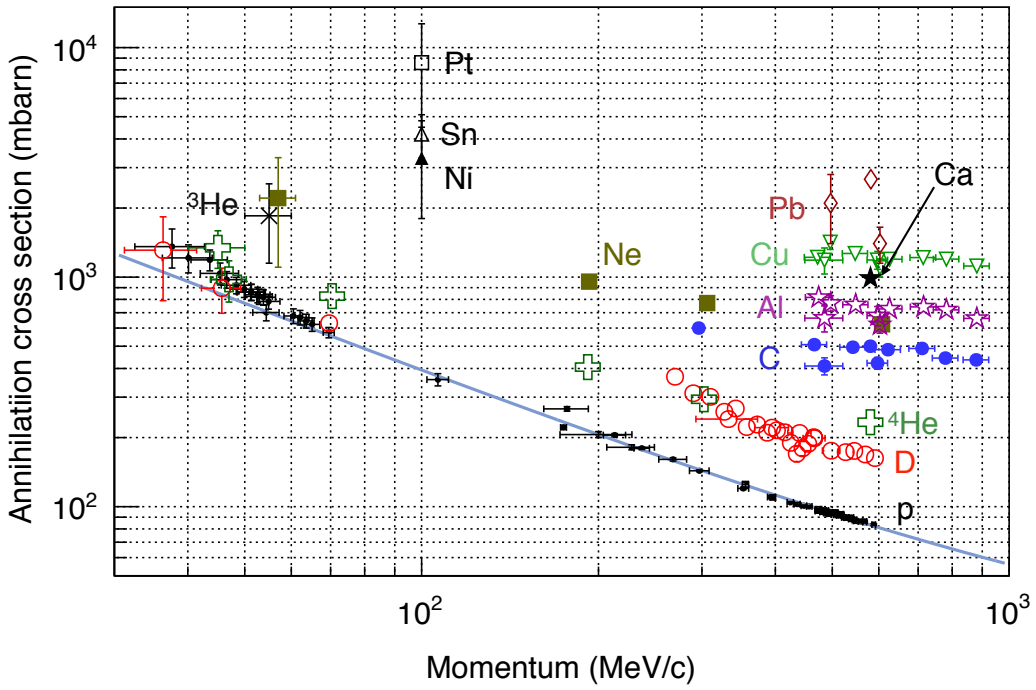

FIGURE 1.7: Annihilation cross sections of antiprotons on various target nuclei at momenta below 500 MeV/c. It is known that the behavior of each cross section can be described by the usual $1/v$ law and the Coulomb focusing effect. This figure is taken from Ref. [8].

1.2.2 Black disk model

The interactions of low-energy antiprotons with nuclei can be expressed by a simple tρ potential (Appendix. D). The potential was constructed to reproduce the annihilation cross sections in Section. 1.2.1 and the data sets of X-ray spectroscopy of the antiprotonic atoms [6, 24]. The results show two main features which describe the characteristics of the interactions.

- The imaginary part of the $t\rho$ potential is large and the real part is negligible.This means that the incident antiproton is completely absorbed if its impact parameter is smaller than the radius of the target nucleus. The target nucleus can be assumed to be a black body for the antiproton, i.e. the so called "black disk model".

- The annihilation cross section of antiprotons can be describe by two effects. One is the usual $1/v$ law which relates to the Black disk model, and the other is the Coulomb focusing effect. Coulomb focusing causes antiprotons whose impact parameter is larger than the radius of the radius of the target nucleus. This effect in the low energy region can be described by a semiclassical approach proposed by Blair [25].

Based on the characteristics above, the annihilation cross section of an antiproton $\sigma_{\rm anni}$ on a nucleus can be written as a following (see Ref. [2]).

$$\sigma_{\rm anni} \;=\; \pi R^2\left(1+\frac{Z\alpha\hbar c}{ER}\right) \tag{1.3}$$

where R and Z are the radius and electrical charge of the target nucleus, E is the energy of the incident antiproton. The first term in Eqn. 1.3 represents a geometrical cross section seen from the antiproton. The second term represents the Coulomb focusing effect.

This equation has been used to describe the annihilation cross section of an antiproton in a wide momentum range. For example, if the energy of the

incident antiproton is enough large, the second term in Eqn. 1.3 is negligible comparing to the first one, and it can be changed as a following.

$$\begin{aligned} \sigma_{\mathrm{anni}} &\rightarrow \pi R^2 \\ &\propto A^{\frac{2}{3}} \end{aligned} \tag{1.4}$$

where A is the mass number of the target nucleus, and we used $R \sim A^{\frac{1}{3}}$. On the other hand, the Coulomb focusing effect becomes dominant and the equation becomes as below in the low momentum region.

$$\begin{aligned} \sigma_{\mathrm{anni}} &\rightarrow \pi R^2 \cdot \frac{Z\alpha\hbar c}{ER} \\ &\propto RZ \\ &\propto A^{\frac{4}{3}} \end{aligned} \tag{1.5}$$

Here we used $Z \sim \frac{1}{2}A$. Therefore by plotting the cross section of various nuclei with their mass numbers, and fit to see the A dependence, it is possible to understand if this naive assumption of the Black disk model, which had been used in a wide momentum range, can also apply to the lower momentum region we are discussing now.

Fig. 1.8 shows annihilation cross sections at various momenta as a function of the mass number of the target nuclei.To see the mass dependence described above, the data points were fit with a function $\sigma = \sigma_0 A^{\alpha}$ which is represented by solid lines. The results shows that $\alpha \sim 2/3$. This value is compared with classical view of the target being a black disk, where all incident particles are absorbed when they hit the target nucleus. Therefore, it is essential to see the mass dependence of the $\overline{\mathrm{p}}$ annihilation cross sections at a certain incoming momentum to study if the black disk model works well in the given region.

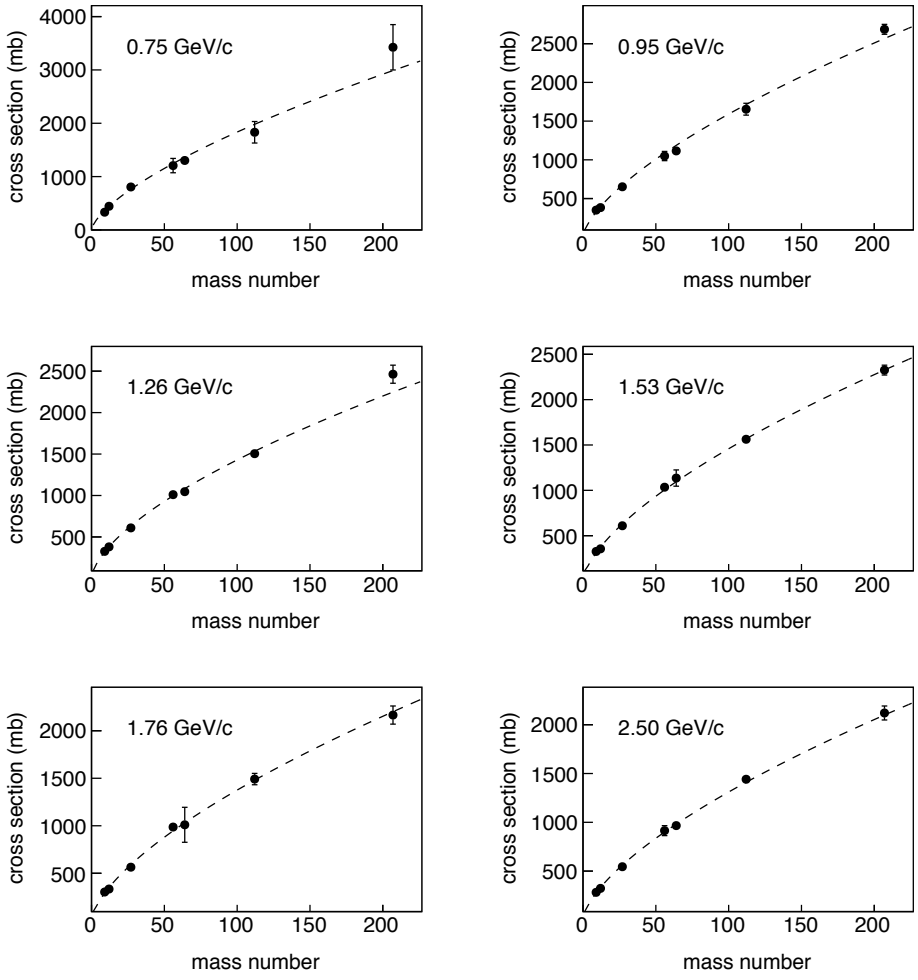

FIGURE 1.8: Annihilation cross sections of antiprotons on Be, C, Al, Fe, Cu, Cd and Pb as a function of their mass numbers. The cross sections at momenta of 0.7, 0.95, 1.26, 1.53, 1.76 and 2.5 GeV/c are shown. The data were fitted by $\sigma = \sigma_0 A^{\alpha}$. The value of α at 0.7, 0.95, 1.26, 1.53, 1.76 and 2.5 GeV/c were determined to 0.700 ± 0.028, 0.650 ± 0.019, 0.636 ± 0.016, 0.645 ± 0.014, 0.646 ± 0.014 and 0.653 ± 0.009. The value of α is consistent with 2/3, which corresponds to the geometrical size of the target nucleus. These data are taken from Ref. [26].

1.2.3 Experimental challenge

There were some technical challenges in carrying out this experiment. In order not to make antiprotons slow down and coming to rest in the foil, the thickness of the target had to be thin (less than 1μm). Manufacturing such a thin foil was difficult, and its precise thickness can not be measured easily.

In our experiment we decided to use a carbon target due to some experimental reasons. As mentioned above an experiment of antiprotons at 100 MeV/c needs a thin foil less than 1 μm to reduce the energy loss in the foils. Especially foils made of heavier nuclei like Ni, Sn Pt are needed to be $\sim$ 100 nm, and such thin foils are not self-supporting. They will be deposited on a solid material, and a carbon foil of $\sim$ 1 μm is used for the reason since the carbon is rigid. Therefore cross sections of Ni, Sn and Pt will be measured with the cross section of carbon, and will be derived by subtracting the carbon's cross section. For these reasons, a precise measurement of carbon's cross section is necessary.

The probability of signal annihilations in the target foil is low ($\sim 10^{-5}$). Most of the antiprotons transversed and scattered at the foils. The antiprotons which hit the experimental apparatus made inevitable backgrounds. Past experiments used a tracking detector to solve this problem, but due to difficulties in tracking the particles, the measured $\overline{\mathrm{p}}$-annihilation cross sections of Ni, Sn and Pt had experimental uncertainties of $\sim$ 50 %, and it was difficult to compare the results with the black disk model.

Experiment of antiprotons at 100 MeV/c can be an unique approach to study the enhancement of the antineutron data. The past study comparing the antiproton and antineutron annihilation cross sections on proton target revealed that the difference of two cross sections becomes larger in the low momentum region due to the Coulomb focusing effects. We expect that the difference between the antineutron and antiprotons can be observed clearly in the low momentum region, thus comparisons at 100 MeV/c, which had not be measured with enough accuracy, will show the difference and effects of enhancement clearly. In terms of the physics of antiprotons, no method to

measure the annihilation cross section at 100 MeV/c has developed. Therefore the annihilation cross section measurement at 100 MeV/c has a meaning to supplement the general lacks of antiproton data at the region.

1.2.4 Thesis objective

In this thesis, the measurement of $\overline{\mathrm{p}}$-annihilation cross section at 100 MeV/c with a carbon target, which is one of the nuclei under discussion (see Fig. 1.1), is described.

The experiment was carried out with the INFN group and members from the Max Planck Institute in the ASACUSA (Atomic Spectroscopy And Collisions Using Slow Antiprotons) collaboration of CERN. The conceptional design was proposed by the INFN group and the author. We performed a new experiment specialized to cross section measurement. This was explained in Chapter 2. A new Cherenkov counter was developed for our measurement. The responsibility of the constructions belongs to the author and described in detail in the same Chapter. Data analysis and discussions were carried out by the INFN group and the author. In Chapter 3, we present the data analysis to determine the cross section. Then in Chapter 4, the obtained cross section was compared to the past $\overline{\mathrm{n}}$ data and theoretical calculations. The mass dependence of the cross sections at 100 MeV/c was also studied there. Finally a conclusion and a future outlook were given in Chapter 5.

The author's main contributions and achievements are as follows.

- Proposal of an experiment specialized to cross section measurements.
- Development of a Cherenkov counter which monitored the relative beam intensities with a precision of $\sim$2%.
- Installation of experimental apparatus in the beam line.
- Operation of the experiment during the beam time. For this experiment the full width of the antiproton pulsed beam was tuned to $\sim$50 ns to reduce inevitable background events.

- Development of the analysis programs.
- Determination of the $\overline{\mathrm{p}}$-annihilation cross section on carbon at 100 MeV/c with a precision of $\sim$10%. The precision was improved by a factor of five comparing to past values with other nuclei targets.
- Obtainment of a future outlook to determine the annihilation cross sections on other nuclei with enough accuracy, which will be necessary to deepen the discussion.

Chapter 2

Experimental method

2.1 Principle of the experiment

In past experiments, the annihilation cross sections were derived from the following equation,

$$\sigma_{\mathrm{anni}} = \frac{\mathrm{N}_{\mathrm{inflight}}}{\rho \mathrm{N}_{\overline{\mathrm{p}}}} \tag{2.1}$$

where σ_{anni} denotes the antiproton-annihilation cross section on a target nucleus, $\mathrm{N}_{\mathrm{inflight}}$ the number of antiprotons that annihilated in the target, ρ the density of the target in atom/cm^2 and $\mathrm{N}_{\overline{\mathrm{p}}}$ the number of incident antiprotons. Values for $\mathrm{N}_{\mathrm{inflight}}$ and $\mathrm{N}_{\overline{\mathrm{p}}}$ were determined during the experiment, but due to low statistics, difficulties of tracking the emerging particles and particle identification, it was difficult to determine those values with sufficient accuracy.

In this new measurement we measured two kinds of signals, annihilations on the target and elastic scatterings on the same target. The cross sections of elastic scattering can be derived numerically by using the Rutherford scattering formula. The $\overline{\mathrm{p}}$-annihilation cross section was calculated with respect to the elastic scattering cross section.

The experimental setup is shown in Fig. 2.1. The incident antiproton beam of p = 100 MeV/c, which corresponds to β (= v/c where v and c are velocities of an antiproton and light) $\sim$ 0.1, was allowed to transverse the target foil. Some (3$\sim$4) charged particles were emitted per an annihilation. To determine the number of annihilations in the target, the emerging charged

particles were detected (N_{anni}). These had velocities $\beta \sim 1$, and hit the detector immediately after the annihilation occurred. This creates the peak indicated by the red solid line in Fig. 2.1.

The elastic scattering of antiprotons was measured by a method called "2nd ring method". A circular ring was positioned downstream of the target. Some antiprotons underwent Rutherford scattering in the target and annihilated on the frame. The resulting peak indicated by the red dashed line contains events originating from annihilations in the target and on the frame. By subtracting the annihilation counts measured using only the target, the contribution from the elastic scattering (N_{Ruth}) was derived.

By using these values the annihilation cross section (σ_{anni}) can be derived using a equation,

$$\frac{\sigma_{anni}}{\sigma_{Ruth}} = \frac{N_{anni}}{N_{Ruth}} \tag{2.2}$$

where σ_{Ruth} denotes the elastic scattering cross section calculated by the Rutherford scattering formula. In this formula there is no dependence on the thickness of the target foil.

Most of the antiprotons transversed the foil and annihilated at the beam dump. The charged particles produced here were detected and is represented by the blue solid line in Fig. 2.1. The background peak can be discriminated from the signals of annihilations at the target position using the time-of-flight method.

For this experiment, the following issues were considered.

- In order to reduce the effect of the small difference of solid angles seen from the target position and the 2nd ring, distances from these positions to the detectors should be large. This is also important to guarantee identical efficiencies of detectors seen from the target and 2nd ring, which depend on the incident angle of the charged particles.

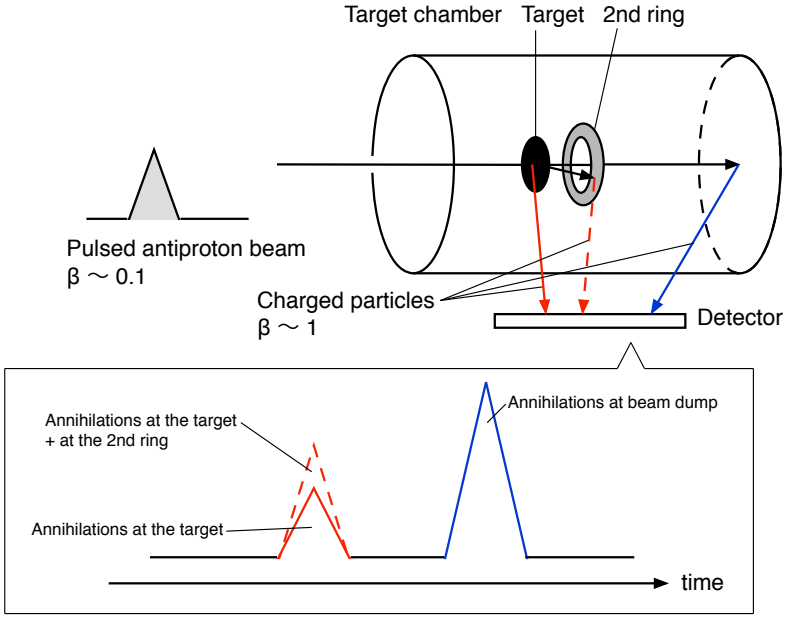

FIGURE 2.1: Overview of the experimental setup. The antiproton pulsed beam passed through a target carbon foil. Some antiproton annihilated in the target and the secondary particles were detected as signals of the annihilations (solid red peak). Some antiprotons underwent Rutherford scattering in the foil and annihilated on the 2nd ring (dashed red peadk). Resulting events are shown by a dashed red line. Most of antiprotons passed through target and annihilated at the beam dump (blue peak).

- Some antiprotons scattered and annihilated on the lateral wall of the target chamber, and produced backgrounds. This background was estimated by simulations.

- Two runs with and without the 2nd ring were carried out. Each spectrum was normalized by the beam intensity. The charged particles emerging from the beam dump (correspond to the blue spectrum in Fig. 2.1) contains the information of the beam intensity. However due to a large difference of the numbers of annihilations at the target position ($\sim$10 events per antiproton pulse) and at the beam dump ($\sim 10^6$ events), the charged particles from the beam dump saturated the detectors and can not be used to monitor the relative intensities of the beam. Therefore, a Cherenkov counter was placed close to the beam dump additionally to monitor relative intensities of the beam. In order to determine the cross section with a precision of 10 %, the linearity of the detector against the intensity of the beam had to be within a few percent. The details of this detector are discussed in Section. 2.5.

2.2 CERN and the Antiproton Decelerator

The Antiproton Decelerator (AD) is the only facility which provides a pure antiproton beam of momentum 100 MeV/c [27]. It is a 188-m-circumference synchrotron (Fig. 2.2). Antiprotons were produced by colliding a bunch containing 1.5×10^{13} protons of 26 GeV/c from the CERN proton Synchrotron (PS) with an iridium or tungsten target. The antiprotons were created via the following reaction,

$$\mathrm{p(Beam)} + \mathrm{p(Target)} \rightarrow \mathrm{p} + \mathrm{p} + \mathrm{p} + \overline{\mathrm{p}}. \tag{2.3}$$

The antiprotons of 3.5 GeV/c were captured by a magnetic horn so that 5×10^7 antiprotons were produced per proton bunch. Those antiprotons were decelerated to 100 MeV/c after they passed through the AD. Since during

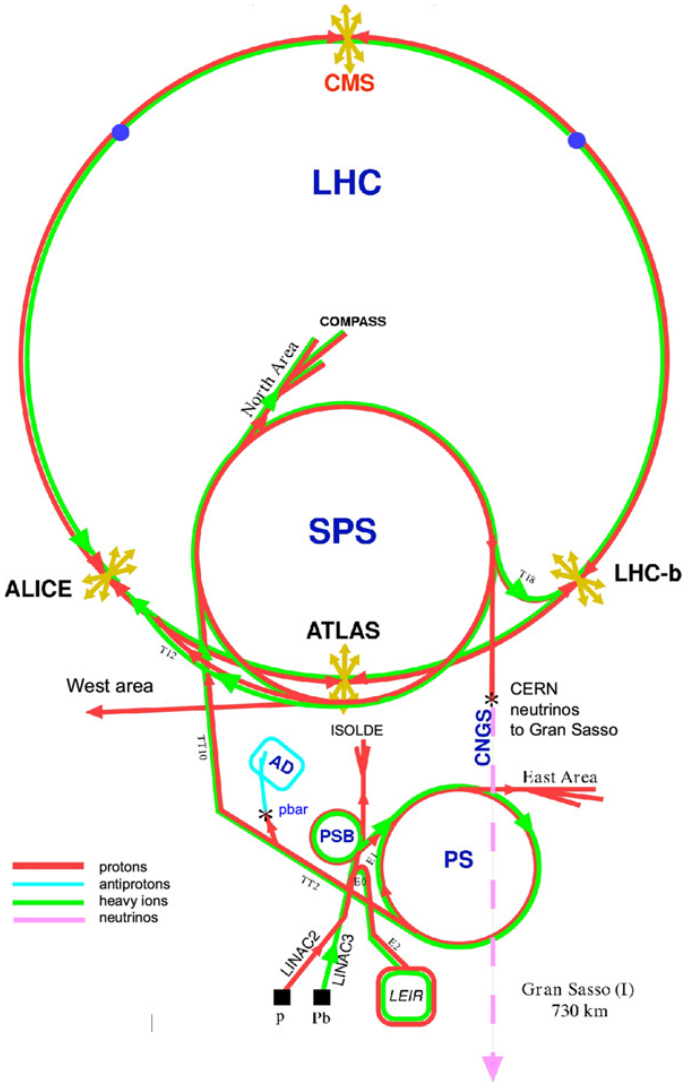

FIGURE 2.2: Schematic layout of CERN's accelerator complex (not to scale). The LINAC2 provided pulsed proton beam of 50 MeV produced from Hydrogen gas source. Proton Synchrotron Booster (PSB) accelerated the beam up to 1.4 GeV and injected it to Proton Synchrotron (PS) which accelerated the beam to 26 GeV/c. For this measurement the beam was sent to the AD where it smashed an iridium target and produced antiproton pulsed beam. This figure is taken from Ref. [28]

.

deceleration the beam the geometrical size of the beam increases due to conservation of phase space, stochastic [29] and electron cooling [30] were used to compensate for the increase of the emittance. A schematic diagram of the AD is shown in Fig. 2.3.

In Fig 2.4 a typical deceleration cycle of the AD is shown. The emittance and momentum spread of the beam at 3.5 GeV/c were initially $\sim$ 200 π mm·mrad and $\sim$ 6 %. After deceleration and coolings they were reduced to $\sim$ 0.3 π mm·mrad and $\sim$ 0.01 % at 100 MeV/c. Finally the AD provided antiproton pulsed beams containing 3 $\times$ $\sim 10^7$ antiprotons at a repetition rate of 0.01 Hz (see Table. 2.1).

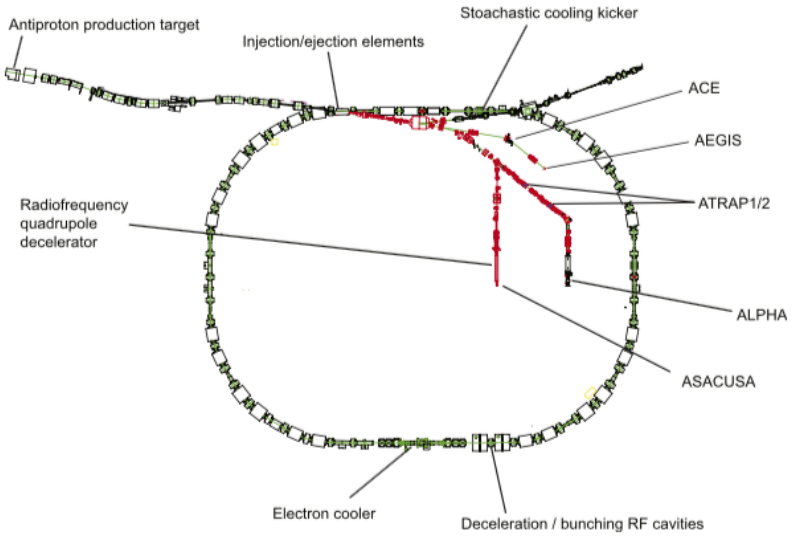

FIGURE 2.3: Schematic top view of the Antiproton Decelerator (AD) in 2012. The antiprotons emerging from the production target are injected into the AD and decelerated to 100 MeV/c with a repetition rate is $\sim$ 100s. Antiprotons at 5.3 MeV(correspond to 100 MeV/c) are injected to the experimental area of the ASACUSA. Overviews of each experiment are written in [23], and this figure is also taken from Ref. [23].

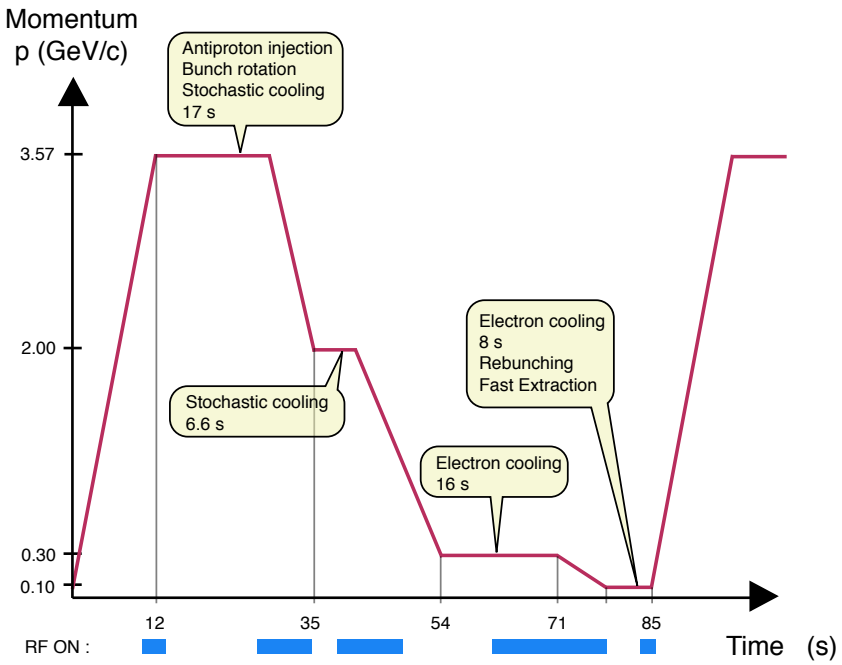

FIGURE 2.4: Typical machine cycle of Antiproton Decelerator, showing the momentum of an antiproton as a function of time elapsed. The timings and durations of the stochastic and electron cooling are indicated.

Momentum (GeV/c)	Transverse emittance (π mm mrad)	Δp/p (%)	Cooling time (s)
3.5	$200 \rightarrow 5$	$1.5 \rightarrow 0.1$	17
2.0	$9 \rightarrow 5$	$0.18 \rightarrow 0.03$	6.6
0.3	$33 \rightarrow 2$	$0.2 \rightarrow 0.1$	16
0.1	$6 \rightarrow 1$	$0.3 \rightarrow 0.01$	8

TABLE 2.1: Stochastic and Electron cooling steps at AD. Antiprotons of 3.5 GeV/c were decelerated by using two stochastic and electron coolings, and antiprotons of 100 MeV/c were produced every 100 seconds.

2.3 Apparatus in the ASACUSA area

2.3.1 Beam line

Fig. 2.5 shows beamline in the ASACUSA area. Three GEM based profile monitors [31] measured the position of the beam. Since they were destructive detectors, the first and second monitors were inserted when they monitored the beam, and removed for the cross section measurement. The last detector was operated during the actual measurements, and functioned as a beam dump. Between the first and the second GEM detectors, quadrupole magnets were placed to focus and guide the antiproton beam to the target position.

Target chambers were placed between the second and third GEM detectors. Inside the chambers target foils were installed. Details of the target system are described in Section 2.4.3.

In this experiment, four kinds of detectors were operated. The GEM detector was used for the beam steeling. The annihilations at the target positions were detected by plastic scintillation counters set besides the target chamber. A Cherenkov counter was set close to the beam dump to monitor relative intensities of the beams. An another Cherenkov counter was under the target chamber. Before the experiment we stopped all antiprotons at the target position, and resulting charged particles were detected by this Cherenkov counter to monitor the time width of the beam. The beam width was adjusted to $\sim$ 50 ns by changing the kicker timing of the AD and by monitoring the beam profile with this Cherenkov counter. Details of these Cherenkov counter are described in the following sections.

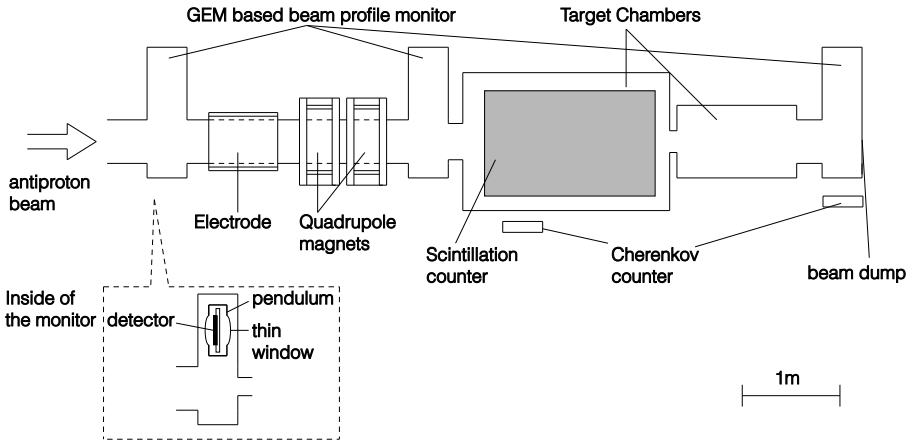

FIGURE 2.5: Experimental setup in the ASACUSA area. Three GEM-based beam profile monitors [31] (described details in the next subsection) were used to steer the beam through the center of the chamber. Dipole and quadrupole magnets were used to modify its trajectory. The last beam profile monitor functions as a beam dump, and a Cherenkov counter was placed close to it.

2.3.2 Beam monitor

Three Gas Electron Multiplier (GEM) beam profile monitors were installed in the beam line to guide the antiproton pulsed beam to the target foil. The first, second and third GEM counters in Fig. 2.5 from the upstream of the beam line were called GEM28, GEM45 and GEM47.

The active area of the detector was $10\times10\text{cm}^2$. The argon-dimethylether (DME) in the proportion 90-10 was used as a gas buffer. The antiproton hit the cathode plane and produced electrons, and the number of electrons was multiplied with a gain of a few hundreds. The transverse beam profile was measured by the XY-readout. The cross section of the detector is shown in Fig. 2.6.

The beam profile was strongly influenced by the multiple scattering and secondary particles produced at the window of the GEM counter. The early study showed that the beam of σ = 3 mm became 10 mm when the beam

profile was measured with this GEM counter. Therefore when we discuss distributions of the beams their upper limit was used.

The GEM counter completely stopped the beam when it monitored the beam profile. Therefore, the beam was put in and out during the beam steering. At the beginning of the steering, the profile at GEM27 was adjusted to the central position so that its central mean value became within ± 1 mm. In the next step GEM45 was installed and also steered the beam to its center. The GEM47 was used to monitor the relative positions of the beams to check fluctuations of the beam positions.

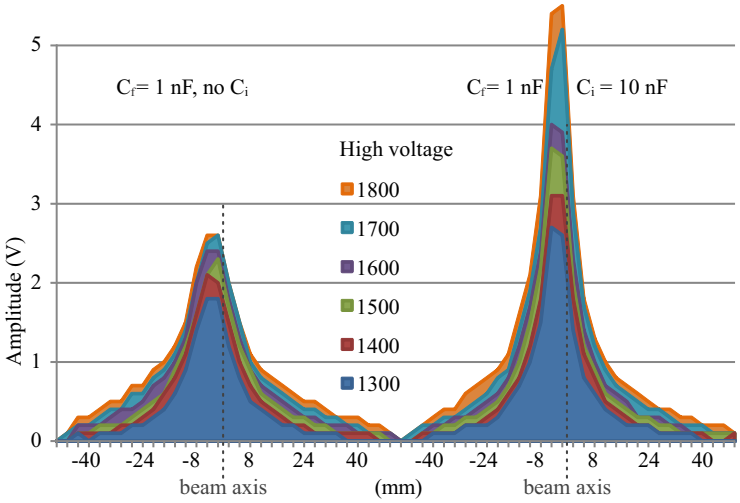

FIGURE 2.6: Beam profile measured by the GEM detector with various applied voltages. This figure was taken from Ref. [31].

2.3.3 Target chamber and target system

Some details of the target chambers are illustrated in Fig. 2.7. In order to insert sufficient distance between the target and beam dump, two stainless steel chambers of diameters d = 1.2 m and 0.6 m, and lengths l=1.7 m and 1.3 m, were connected together. The thicknesses of their walls were $\sim$ 5 mm.

The target foils were attached to a ring frame of diameter d = 12 cm. The 2nd ring, with inner and outer diameters of 6 cm and 11 cm respectively, was placed 15 cm downstream from the target position. The rings were large enough to make the annihilations on them caused by any beam halo negligible. The foils were suspended by rotational manipulation arms of thickness 1.5 mm. Annihilations on the arms were also negligible. The target was placed 60 cm from the entrance of the chamber. Its position was controlled by positioning the arms with a precision of $\pm$1 mm. A picture of the target folder and manipulation arms are shown in Fig. 2.9. A turbo pump and an ion pump evacuated the system to a pressure of 10^{-7} mb.

Details of the scintillation planes will be described in the following section, but geometrical setup of the planes are shown in fig. 2.8. We used three scintillation planes named P6, P8 and P13. They covered $\sim$30% of the total solid angle. A picture of the experimental setup is shown in Fig. 2.10. Scintillation detectors (black plates in the figure) surrounded the target chamber.

2.3.4 Cherenkov counter under the target chamber

An acrylic Cherenkov counter of $48\times16\times2$ cm^3 made of Bicron BC-800 was set under the target chamber. The distance was 40 cm from the target position and the solid angle seen from the target position was 1%. This was used to measure the time width of the beam before the data taking. For the purpose we stopped all antiprotons at the target position by using a blank target. Charged particles emerging from the annihilations were detected by this Cherenkov counter, and the time information of the beam was obtained.

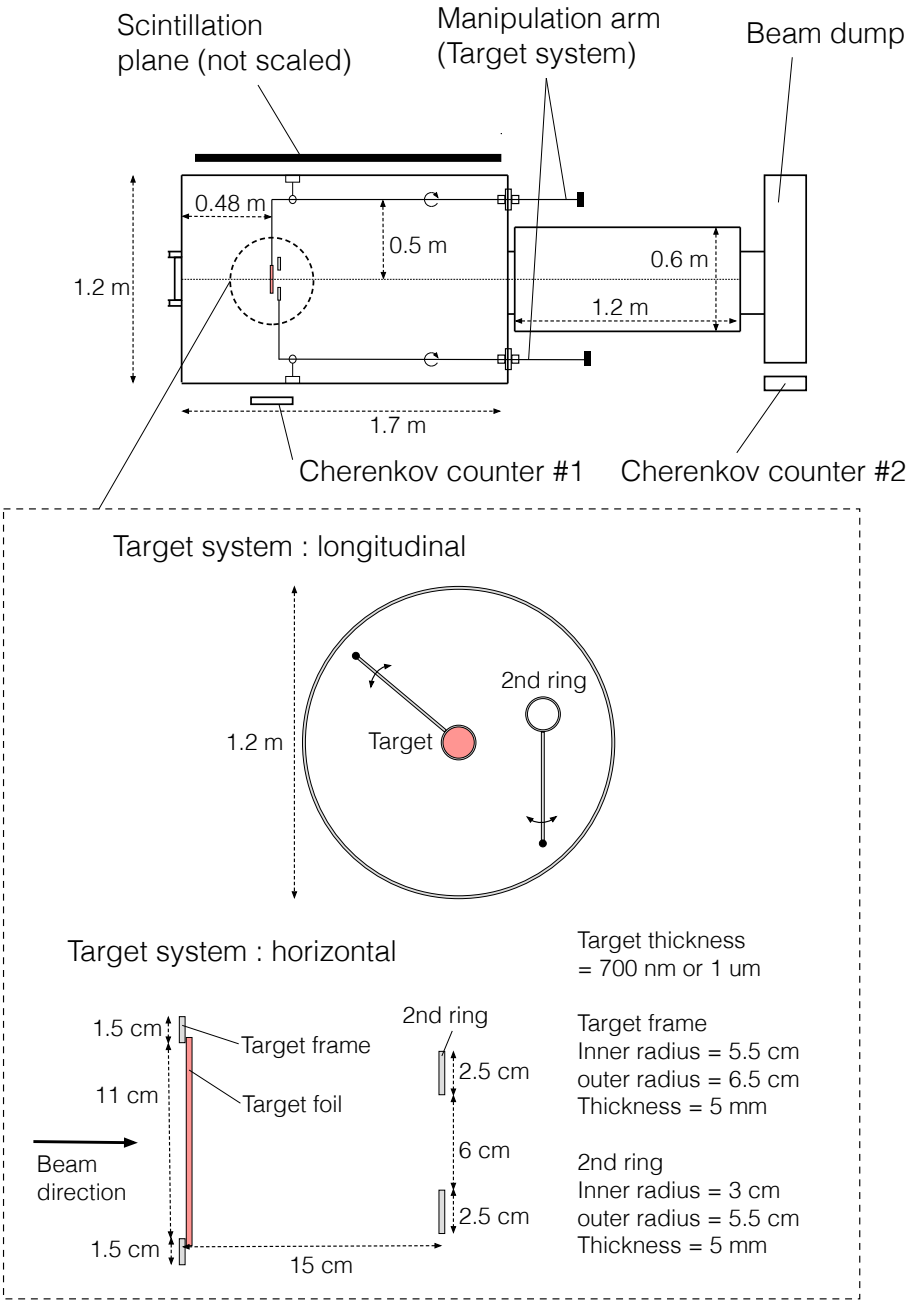

FIGURE 2.7: Experimental layout of the target chambers. Two chambers were connected together to ensure a sufficient the time of flight of an antiproton from the target to the beam dump. Target foils and 2nd ring were moved by manipulation arms. View seen from the beam line axis, and details of positions of the target system are shown together.

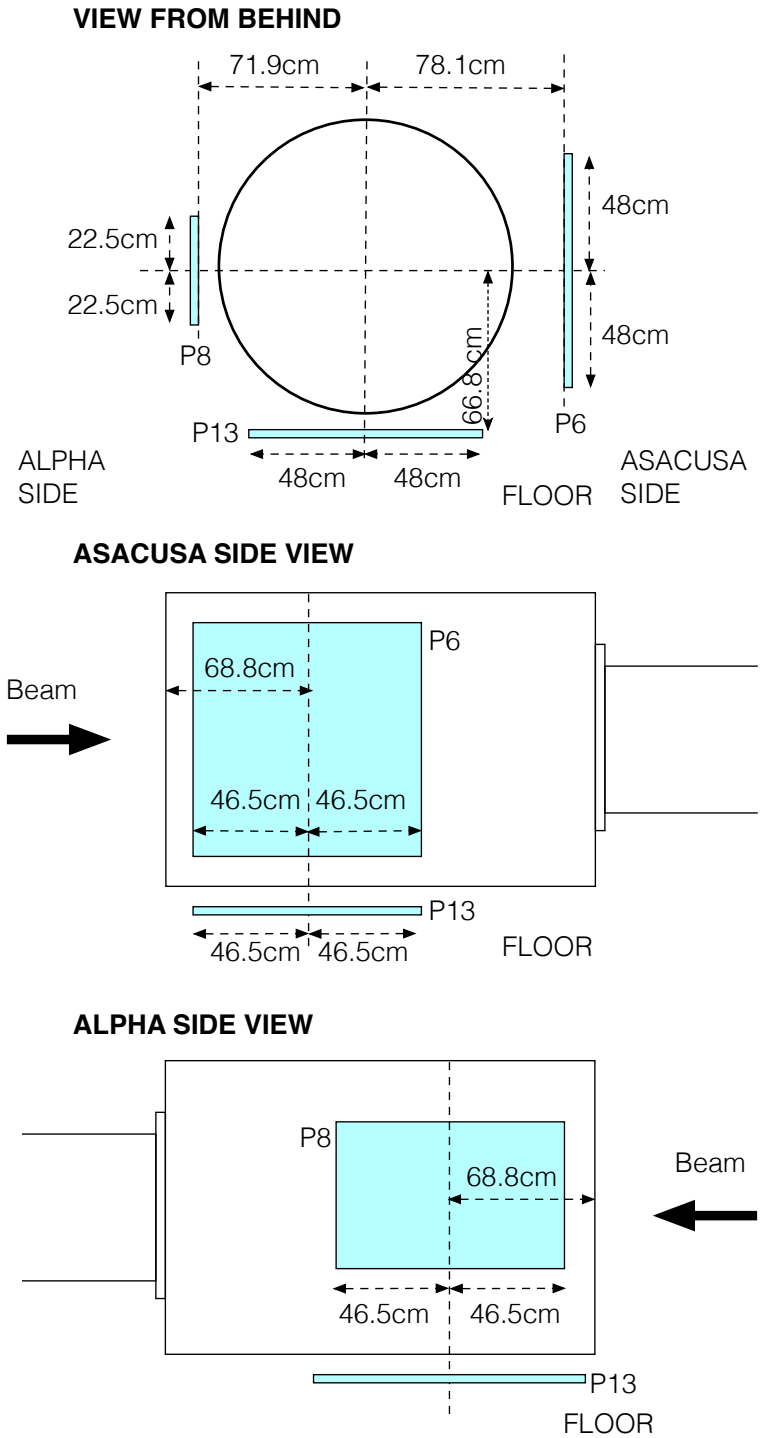

FIGURE 2.8: Exact positions of each scintillation plane. Back and top views are shown. The planes covered more than 30% of the total solid angle.

FIGURE 2.9: Photos of a target and a manipulation arm. The inside the target chamber is shown.

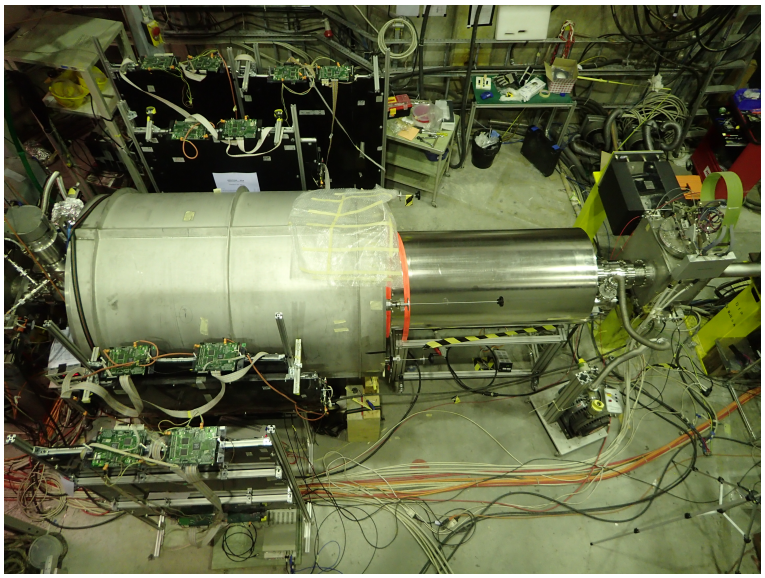

FIGURE 2.10: Photos of the target chamber, beam profile monitors and detectors.

We monitored to beam profile by changing the kicker timing of the AD and derived correct AD timing to make the full pulse width of ∼50 ns.

The refractive index of the Cherenkov material was 1.49 and detected charged particles of $\beta > 0.7$. The readout of the signal was done by a photomultiplier tube (PMT, R5505G-ASSY) originally developed for the antiprotonic helium experiment [32]. Inside the PMT 15 fine mesh dynodes were installed. The photocathode connected to a high voltage power supply with a low output impedance, and it supplied 15 V. A diagram of the voltage divider of the PMT is shown in Fig. 2.11.

The obtained waveform was recorded using an oscilloscope with a bandwidth of 1GHz. After the steeling we obtained a spectrum like in Fig. 2.12 which showed that the full time-width of the beam was less than 50 ns.

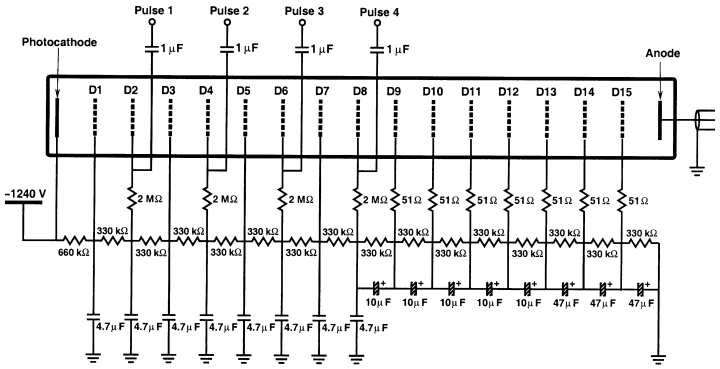

FIGURE 2.11: A diagram of the voltage of the fine-mesh photomultiplier (R5005G-ASSY). This figure was taken from Ref. [32].

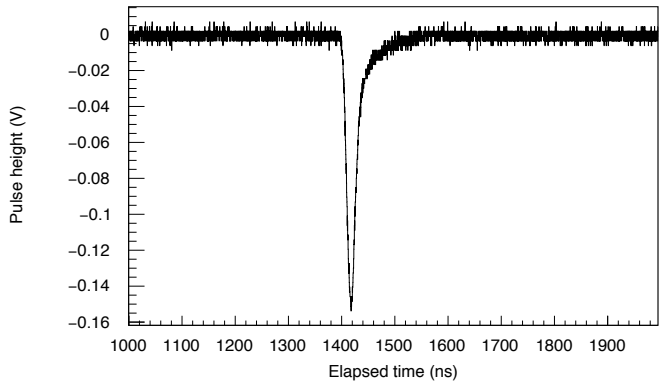

FIGURE 2.12: Time profile of the beam used for this experiment. The spectrum was measured by the acrylic Cherenkov counter.

2.4 Scintillation detectors

The scintillation detectors were constructed and operated by collaborators from INFN (Istituto Nazionale di Fisica Nucleare)[1]. The detector had been used for antiproton-nucleus annihilation cross section measurement [33, 34], and its details are described in Ref. [35].

Three planes composed of scintillation bars were used in the experiment. Two had a sensitive area of $\sim$ 1 m^2 and composed of 62 scintillation bars, whereas one had a size of $\sim$ 0.5 m^2 and consisted of 32 bars. Those scintillation bars were manufactured at Fermi lab[2], and they are shown in Fig. 2.13. They are composed of Polystyrene Dow Styron 663 W + 1 % and PPO + 0.03 % POPOP and white TiO_2 coating. Scintillation light was collected and read out using Kuraray[3] wavelength shifting (WLS) fibers of 1mm diameter. A hole of 1.5 mm diameter was made for each scintillation bar, and the fibers were installed in them. The size of each bar was 96 cm^2 and 1.5 $\times$ 1.9 cm^2 [36].

[1] http://home.infn.it/it/
[2] http://www.fnal.gov/
[3] http://www.kuraray.co.jp/en/

The WLS fibers were read out by several multi-anode Hamamatsu 64 channel H7546-B PMTs. In order to reduce the cross talks, each channels was read out by two PMTs. The signal readout was carried out by a custom front-end board (FEB) with a MAROC3 ASIC. On the FEB board two FPGAs (Altera Cyclone II) and a 12 bit ADC were installed, and the digital signals were sampled by FPGAs with its 300 MHz sampling time.

The scheme of the data taking is shown schematically in Fig. 2.14. When the DAQ system was triggered from the AD's starting signal, signals from the PMTs were sampled with a sampling rate of 300 MHz and provided 0/1 signals when the signal was below or above a certain threshold. The starting point (when the pulse exceeded the threshold) and the length of the signals (which were assumed to be proportional to the pulse height) were used to count the number of hits.

The positions of each plane are shown in Fig. 2.8. The detectors covered more than 30% of a total solid angle. Since one annihilation emitted ~ 3 charged particles, this setup enabled us to detect at least 1 of those particles per annihilation.

2.4.1 Efficiency of the scintillation counter

Efficiencies of the scintillation counters were measured at T9 beam line of CERN. The proton bunch from PS collided with a target to produce varieties of secondary particles to be used for the measurement. The process produced electrons, positrons, muons, pions, kaons and (anti) protons. The particle had momenta from 0.5 to 10 GeV, those were typical values of the charged particles (mostly pions) [32]. The maximum rate of the beam was 10^6 particles per second. In the beam line, gas jet Cherenkov counters were used to identify the particle, and timing was measured by plastic scintillators set upstream and downstream of the detector to be tested. The test revealed that the efficiency of the scintillation counters were better than 90%. The

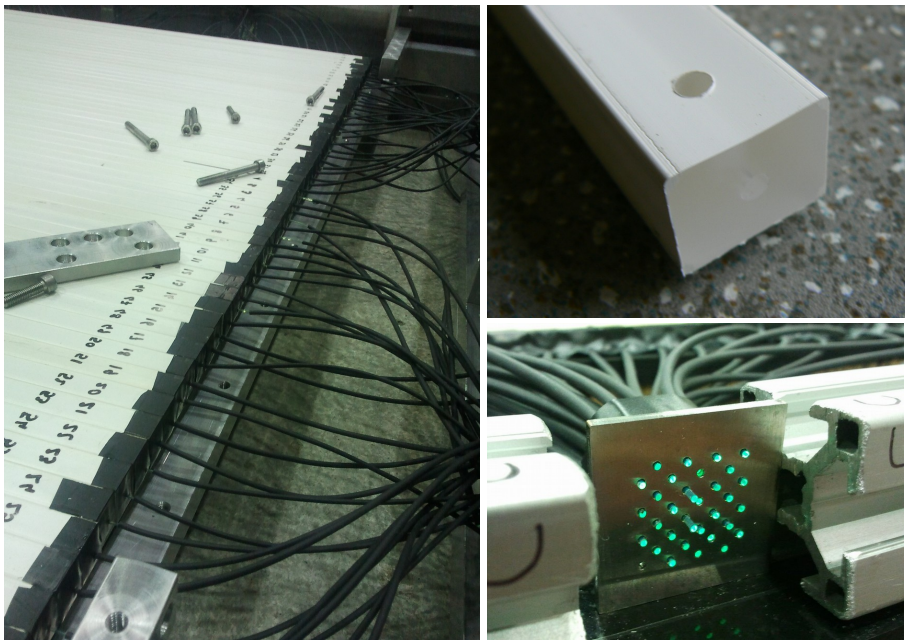

FIGURE 2.13: Right top: the scintillator bars used in the detector. Right bottom: Each WLS fibers were collected by using an aluminum plate. Left: a scintillator plane made of 62 bars. These photos were taken from Ref. [34]

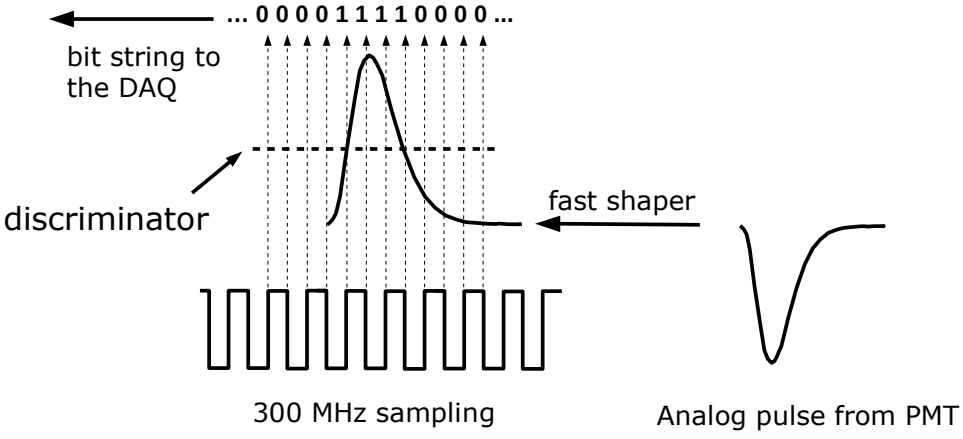

FIGURE 2.14: Details of the digital acquisition scheme on the FEB. String data set of 0 or 1 was stored when the signal was above or below the threshold. This figure was taken from Ref. [34].

applied voltage of -750 V was used for this experiment, and the same value was applied also for this experiment.

The timing resolution of the scintillation counter is critical since we identify the hit of the particle by only the timing information. The timing resolution of the whole system was calculated using the experimental data, which will be discussed in the analysis part of this thesis.

2.4.2 Cherenkov counter at the beam dump

The Cherenkov counter for the normalizations of the spectra was positioned 30 cm below the beam dump (Fig. 2.15 and in Fig. 2.16). In order to determine the cross section with a precision of $\sim 10\%$, we needed to monitor the relative beam intensities with a precision of a few percent. For that reason we developed a Cherenkov counter consisting lead fluoride crystals and avalanche photodiodes.

The AD generated a master trigger signal every ~ 100 seconds, which started the waveform acquisition over a 2 μs interval. A VME64X bus was used with a controller connected to a PC in which the data was acquired. We tested some types of radiators, types of photodiodes and their combinations.

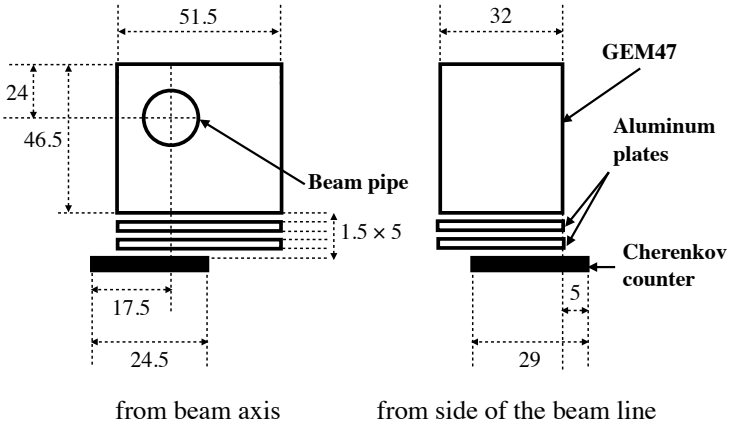

FIGURE 2.15: Position of the Cherenkov counter are shown in centimeters. It was placed 30 cm away from the target position. Views along the beam axis and from the side are shown.

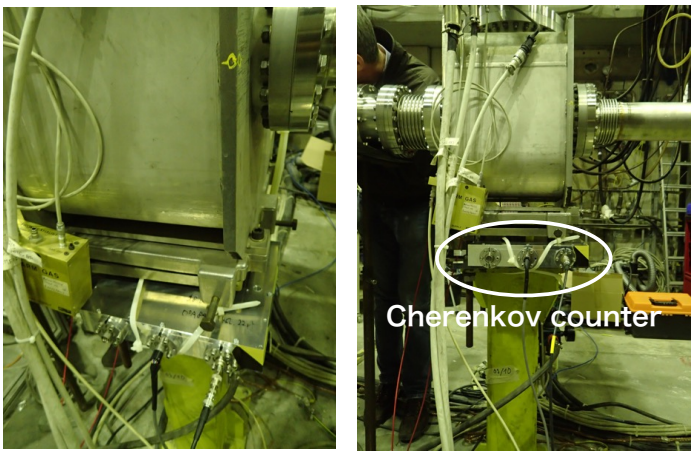

FIGURE 2.16: Photos of the Cherenkov counter. It was placed under GEM47 which functioned as a beam dump.

2.4.3 Target foil

The largest backgrounds were caused by annihilations of antiprotons on the lateral walls of the target chamber. The antiprotons that scattered on the target reached the lateral wall before the antiprotons that reached the beam dump. The solid angle seen from the lateral wall is larger than the one seen from the target position.

In order to visualize the effects of the shape of the beam to the analysis, we carried out toy Monte-Carlo simulations. The results are shown in Fig. 2.17. The process of the simulation was as followings.

- When antiprotons were injected to the target some antiprotons scattered and annihilated at the lateral wall.
- The resulting charged particles hit the detector. The branching ratios of the emitted charged particles were implemented into the simulation to reproduce the past data of antiproton annihilations [32].
- In this simulation we just count the timing of hits, and no particle identifications were done.
- We assume that the cross section of the antiproton annihilation on carbon at 100 MeV/c should be 1 barn to follow the theoretical calculations. The cross section was also implemented.
- The obtained spectrum contains both the background and signals from the target positions.
- We tested the pulse width of 200 ns and 300 ns. 200 ns is a typical pulse width of the beam from the antiproton decelerator.

In Fig. 2.17 (a) the background was simulated with the expected annihilation spectrum in the target. The solid line represents signals caused by annihilations at the target position. The annihilation cross section was assumed to be 1.0 barn. The background from the lateral wall is represented

by a dashed line. A pulsed beam containing $\sim 10^8$ antiprotons full width at half maximum of 200 ns was simulated. The antiprotons took > 20 ns to reach the lateral wall. This fiducial region which was indicated by the dashed lines in Fig. 2.17 (a) and (b), was used to count the annihilation signals in the target.

However if the pulsed antiprotons had a larger slope in time, it would be hard to select the 20 ns interval correctly. In Fig 2.17 (b) shows results when we used a 300 ns long pulsed beam. In this case it would be necessary to expand the range of integration taking into account the backgrounds.

Two issues are here important. The first is the reduction of background events from the lateral wall. Since the number of scattered antiprotons is smaller for targets of low mass number, we decided to use a carbon target. Thin carbon foils of 700 nm and 1000 nm were used to minimize the effects of energy loss ($\sim$10 keV for 5.3 MeV/c antiprotons [37]). We also tuned the timing of the kicker and reduced the pulse width of the antiproton beam to $\sim$ 50 ns.

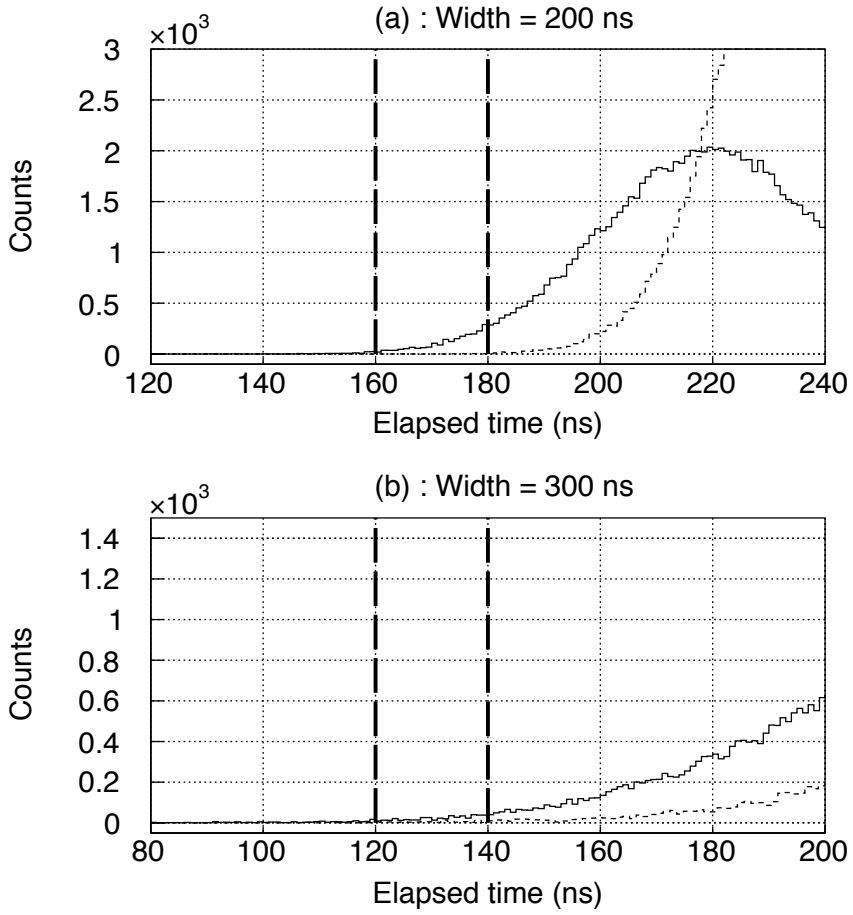

FIGURE 2.17: Simulated background events caused by annihilations on the lateral wall of the target chamber. A carbon foil of 1 μm thickness and incident 10^8 antiprotons particles were assumed. Solid lines in both figures show signals of antiproton-annihilations in the target foil. The dashed histogram corresponds to background caused by annihilations on the lateral wall. Area defined by vertical lines represents the no-background regions. Different pulse lengths of the antiproton beam (200 ns in Fig (a) and 300 ns in Fig (b)) were used.

2.4.4 Extraction of the beam

In order to reduce the beam intensity per antiproton pulse, the AD was operated in the so called "multiple extraction" mode. In the usual mode of operation, the AD decelerates a single bunch containing 3×10^7 antiprotons every 100s. In multiple extraction mode the bunch was divided into six pulses each containing 5×10^6 antiprotons. The pulse width was adjusted to $\sim$ 50 ns with a rise time of $\sim$ 15 ns by tuning the timing of the kicker magnet in AD.

2.4.5 Material of the 2nd ring

For target nuclei of large mass number, charged pions emerging from antiproton annihilations are absorbed in the nuclei with a high probability. This caused a difference of multiplicities depending on whether the antiproton annihilated in the target (carbon) or in the stainless steel (SUS304).

D. Polster $et.al$ observed a decrease of the number of detected charged pions when the mass number of the target was increased [38]. The multiplicity of carbon target was 4.5 % larger than with Fe target (Fe is a main component of the stainless steel (see Appendix E).

This difference of multiplicities of antiproton-nucleon annihilation on various nuclei was studied by J. Cugnon $et.al$. They studied the absorption mechanism of pions, produced by an antiproton-nucleon annihilation but absorbed before they were emitted outside of the target nucleus [39]. A simple model in which a target nucleus is assumed to be a black disk reproduced the experimental multiplicity well [40].

In order to avoid this multiplicity problem, carbon fibers manufactured by MICROCOMPOSIT [4] of thickness 1.5 mm were used for a material of the 2nd ring. Since the fiber contained small amount of other materials, small corrections of multiplicity were applied as systematic errors.

[4] http://www.microcompositi.it/

2.5 Construction of a Cherenkov counter

2.5.1 Overview of the Cherenkov counter

In order to determine the cross section with a precision of $\sim$10%, it was necessary to monitor the relative intensities of the beam with a precision of a few percents. For this purpose, a Cherenkov counter using photodiodes was constructed.

In past measurements of annihilation cross sections, an acrylic Cherenkov counter read out by a photomultiplier tube (PMT) was used [32]. For this measurement, we used photodiodes due to their compact size, high linearity and high gain stability. Linearities and backgrounds of two types of p-i-n photodiodes and an avalanche photodiode against the pulsed antiproton beam were studied. The photon yields of five types of radiators and their combinations with photodiodes were also tested.

To maximize the Cherenkov photon yield, lead fluoride crystals (PbF2), which have a high refractive index of 1.89 was used [13, 41–44].

The main backgrounds of the photodiodes against the pulsed antiproton beam were caused by direct hits of pions to their depletion layers. This is called the nuclear counter effect [45]. In order to reduce the backgrounds, avalanche photodiodes, with depletion layer thickness of a few μm, were used.

2.5.2 Apparatus

Fig. 2.18 shows a schematic view of the Cherenkov counter. Five radiators of size 3 cm $\times$3 cm$\times$16 cm were installed in a 25 cm$\times$30 cm $\times$ 16 cm aluminum box of wall thickness 5 mm. The box was hermetically sealed and put with nitrogen to avoid moisture condensation on the cooled photodiode. The radiators were covered by two layers of reflectors (Immobilon-P Membrane, IPVH00010[5]). Each crystal was read out by a photodiode. The photodiodes were mounted on a copper block.

[5]http://www.tgk.co.jp/info/0719233707.html

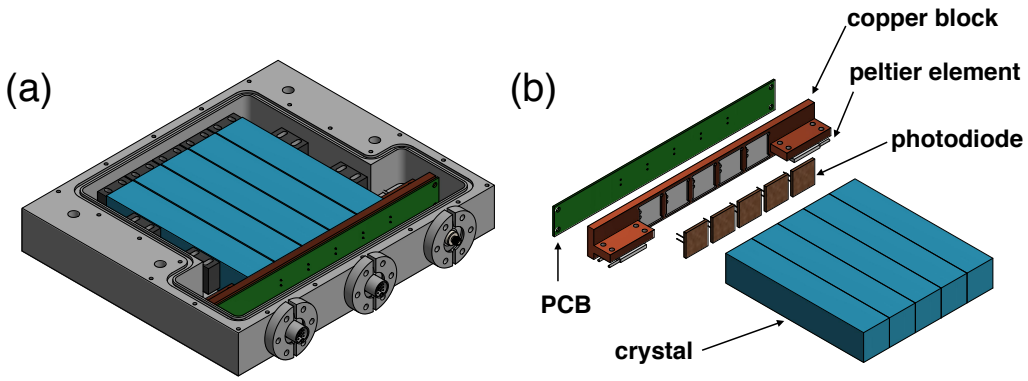

FIGURE 2.18: Schematic view of the Cherenkov counter. All components were installed inside hermetically aluminum box. (b)Details of the Cherenkov counter. The Cherenkov photons were readout by photodiodes. They were attached to a copper block together with two Peltier units and an electrical circuit board.

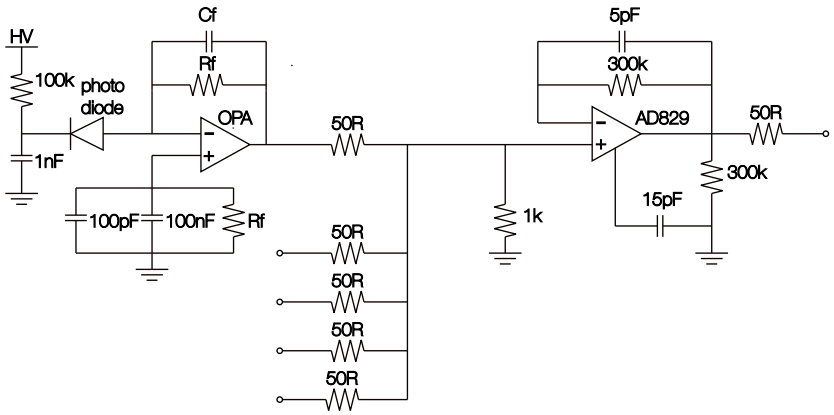

FIGURE 2.19: Circuit diagram for the readout of the detector. Cf, Rf and OP represent feedback capacitors, feedback resistors and an operational amplifier. Their types were optimized for each photodiode.

The readout electronics are schematically shown in Fig. 2.19. The cathodes of the photodiodes were biased through 100-kΩ resistors and 1-nF storage capacitors. The anode signals from each photodiode was read out by a transimpedance preamplifier. The output signals of the five preamplifiers were summed using a resistor network, before being further amplified by an operational amplifier (Analog Devices AD829AR) with a bipolar transistor input stage, which was used as a non-inverting follower of gain 2. The five photodiodes, six amplifiers, direct current (DC) linear voltage regulators, and high voltage biasing circuits were mounted on a single 4-layer printed circuit board (PCB) of size 30 mm x 200 mm and thickness 1.6 mm made of Panasonic Electronic Works R1705 type glass epoxy.

For the avalanche and larger-sized p-i-n photodiodes which produced relatively large signal amplitudes, we used transimpedance amplifiers that contained an operational amplifier (Texas Instruments OPA842IDB) with a bipolar transistor input stage and an open-loop gain bandwidth product of $f_b = 200$ MHz. As the capacitance of the detectors were relatively large C_D, at low values of the feedback resistor (R_f =1 kΩ for S8664-1010 and 3 kΩ for S3590-08) the output signal showed excessive ringing and oscillation. This was reduced by introducing a compensating feedback capacitor (C_f = 22 pF for S8664-1010 and 12 pF for S3590-80). For the smaller-area p-i-n photodiode with a faster timing response and smaller signal amplitude, an amplifier (OPA843IDB) of larger open-gain bandwidth product $f_b = 800$ MHz in conjunction with a larger feedback resistor $R_f = 3$ kΩ and smaller capacitor $C_f = 2$ pF were used.

Two Peltier units (MELCOR, CP1.0-63-05) and temperature sensors (Analog Devices, AD590MH) were mounted to the copper block to monitor and control the temperature of photodiodes. The maximum current for the Peltier unit were 3.9 A, and its cooling power 16.6 W. The summed signal was read out via a sma feedthrough connected to one side of the chamber. Temperature sensors and Peltier units were controlled through the second feedthrough.

2.5.3 Types of radiators

The photon yields of five types of radiators (Lead fluoride, fused silica (T-4040), acrylic (CLAREX) a lead glass (SF57HTTULTRA) and an eco-glass (S-TIH53W) were tested. The dfferences of photon yields against various directions of the incident particles entering the detector were studied. The types of radiators, their refractive indexes and densities are summarized in Table. 2.2.

Radiator Material	Refractive index	density[g/cm^3]
Lead Fluoride	1.89	8.45
Eco Glass (S-TIH53W)	1.84	3.54
Lead Glass (SF57HHT ULTRA)	1.84	7.77
Fused Silica (T-4040)	1.49	1.18
Acrylic (CLAREX)	1.46	2.20

TABLE 2.2: Five types of radiators and their refractive indexes and densities.

Lead fluoride (PbF2) crystals have been used in nuclear physics experiment as Cherenkov counters and calorimeters [46, 47]. It has a very high refractive index of 1.84, and density (8.45 g/cm^3), a short radiation length (9.3 mm) and a small Moliere radius (22 mm).

A Cherenkov counter with PbF2 crystals was used for positron annihilation life time spectroscopy (PALS) [48] by detecting the γ rays emitted from the annihilation. Initially the experiments used $PbWO_4$ crystals (lead tungsten) as a scintillator radiator, but the timing resolution was limited to the decay time of its scintillation around 20 ns. In the case of a Cherenkov counter, a timing resolution of $\sim$ 3.5 ns was achieved.

The H1 collaboration at DESY (Deutsches Elektronen-Synchrotron) studied its optical properties, radiation hardness, position resolution and spatial homogeneity against pion and electron beams [47]. The efficient separation of electromagnetic and hadronic showers was demonstrated. The A4 collaboration studied PbF2 crystals for use in a Cherenkov calorimeter in a parity violation experiment at MAMI [41, 49]. The number of photoelectron ($p.e.$)

per MeV read by a hybrid photomultiplier tube (HPMT) was between 1.7 and 1.9. Anderson $et.al.$[50] showed that PbF2 had a higher radiation resistantance than usual lead glass, and the p.e. response almost fully recovered after a short exposure to UV light.

The g-2 experiment at Fermilab, studied an electromagnetic calorimeter which consisted of an array of 54 PbF2 Cherenkov crystals read by large-area silicon photomultipliers (SiPM) [51]. The response against 2.0 - 4.5 GeV electrons under a variety of using beam, impact position, angle and wrapping of crystals was studied. They found that using white-diffused wrapping, an energy resolution σ/E of (3.4$\pm$0.1) % $\sqrt{E/\mathrm{GeV}}$ was achieved.

On the other hand, some cracks and defects were reported on the surfaces of the PbF2 crystals due to its brittleness. These defects became worse in larger sized crystals. The A4 experiment investigated photon scatterings, absorption and surface damages of 1000 crystals [44]. Ren $et.al.$ reported that contamination, mainly oxygen, affected the light yield, transmission [42] and growth of the crystal by using the non-vacuum Bridgman method [43].

Some other radiation materials that were tested are listed in Table. 2.2. S-TIH53W was an artificial glass with a high refractive index of 1.84 and a small Abbe number of 23.8. Schott SF57HHT-ULTRA, which improved transmission comparing to SF57HHT, and its transmission is almost 100 % for wave lengths between 400 to 700 nm. , has been previously used for electromagnetic calorimeters. Due to restrictions on the use of lead in commercial products, so-called unleaded "eco glass" having similar refractive indexes and Abbe numbers as traditional leaded glass such as S-TIH53W were developed. Those eco glasses suffered from poor transmission in the blue regime, but S-TIH53. It has almost same refractive index of PbF2 but a slightly lower density.

The compositions of lead fluoride crystals (PbF2), lead glass (Pb-O-SiO_2) and acrylic is well known, but a composition of the eco glass (S-TIH53W) was not documented. We measured the composition using X-ray photoelectron spectroscopy (XPS). The results of the measurement are described in Appendix. F. We found that the glass consisted of Ba, Ti and Nb.

In past ASACUSA experiments, an acrylic Cherenkov counter was used [32]. It was positioned under the target position and detected charged pions emerging from antiproton annihilations. Its refractive index was 1.46 and its density 1.18. The acrylic Cherenkov counter detected charged particles whose β was larger than 0.7.

A crystal of fused silica manufactured by CoorsTek KK was also tested. It has a refractive index of 1.46 and density 2.20.

2.5.4 Transmission measurement

To have the highest photon yield, the wavelength and position dependences of the optical transmission of each crystal was measured. The measurement was carried out using a spectrometer of the CMS group at CERN.

The measurement scheme is shown in Fig. 2.20. A light beam was fired thorough a sample crystal. A PMT was placed at the injection position and monitored its intensity. At the other side of the crystal another PMT was measured the transmitted light. The wavelength of the light was scanned from 305 nm to 750 nm in 5 nm steps. We measured the longitudinal transmission by injecting the light along the long crystal axis. Three transverse transmissions, at positions 2 cm, 8 cm and 14 cm from the edges were measured to study the spacial dependence. The transmissions includes the contributions from surface reflections.

Fig. 2.21 shows the transmissions of the fused silica crystal (T-4040). The longitudinal and transverse transmissions were both around 94%, which was higher than the other crystals.

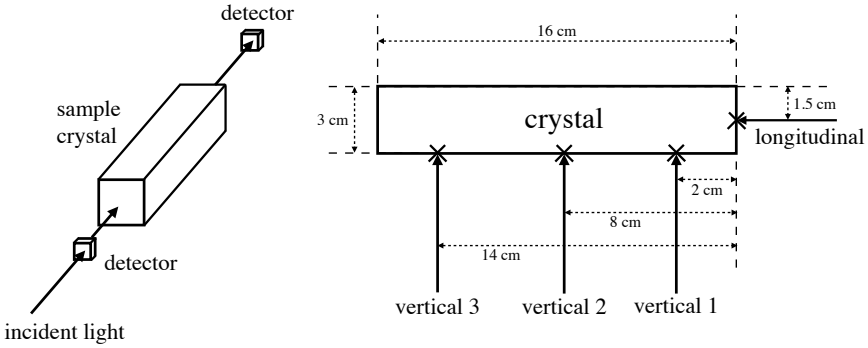

FIGURE 2.20: Schematic layout of the transmission measurement. A probe beam of wavelength from 300 nm to 700 nm was transmitted through the sample crystal, and the light that reached the other end was detected. Intensities of both incident and transmitted light were measured by PMTs. We measured one longitudinal and three transverse points.

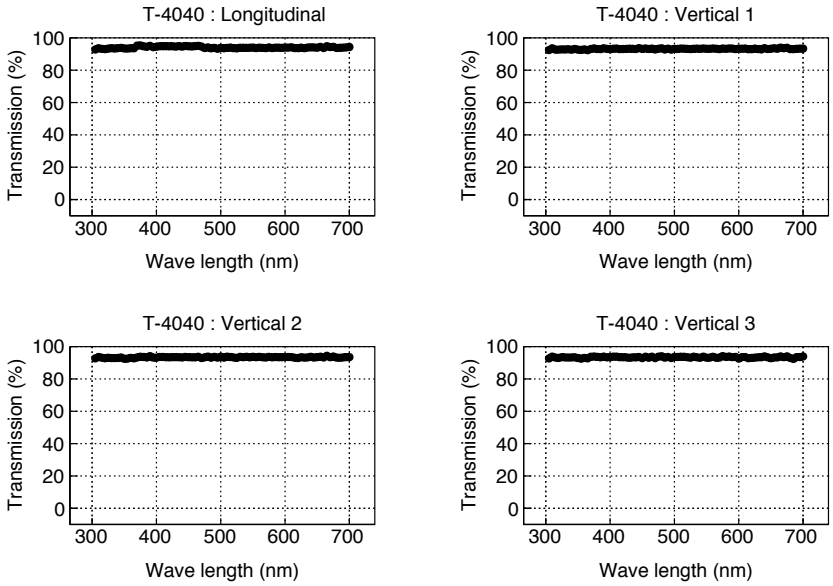

FIGURE 2.21: Transmissions of fused silica (T-4040). One longitudinal and three transverse transmissions were measured.

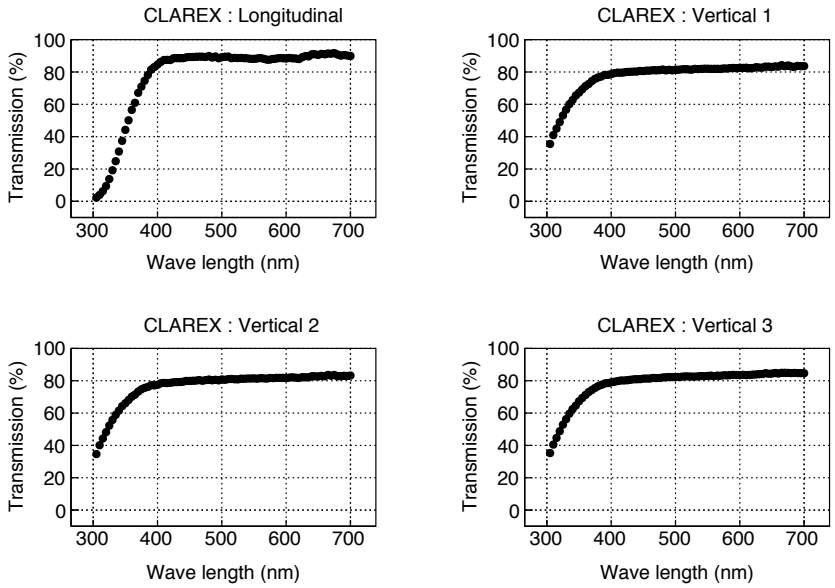

FIGURE 2.22: Transmissions of an acrylic plate (CLAREX). One longitudinal and three transverse transmissions were measured.

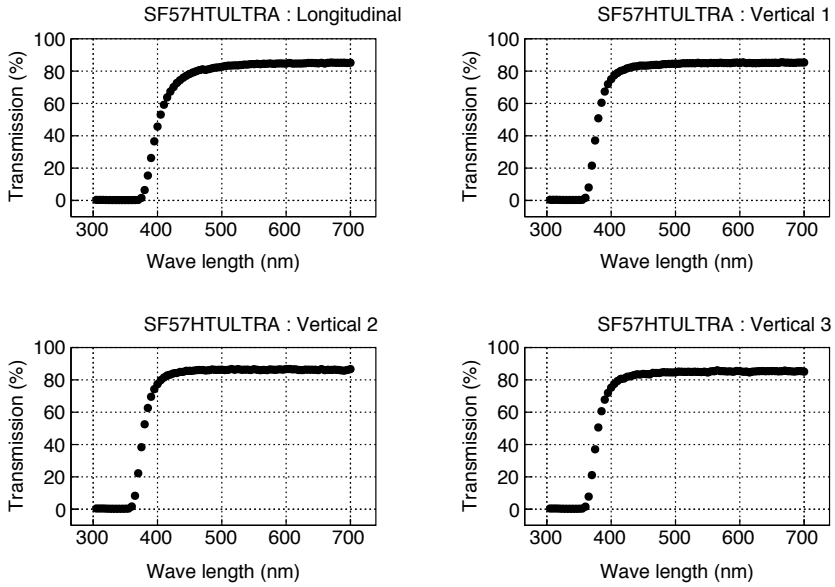

FIGURE 2.23: Transmissions of a lead glass crystal (SF57HTULTRA). One longitudinal and three transverse transmissions were measured.

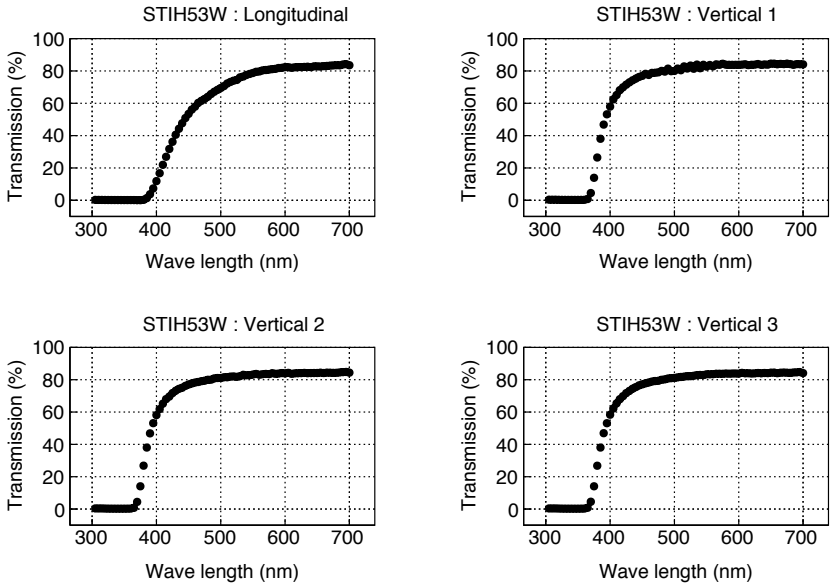

FIGURE 2.24: Transmissions of an eco glass crystal (STIH53W). One longitudinal and three transverse transmissions were measured.

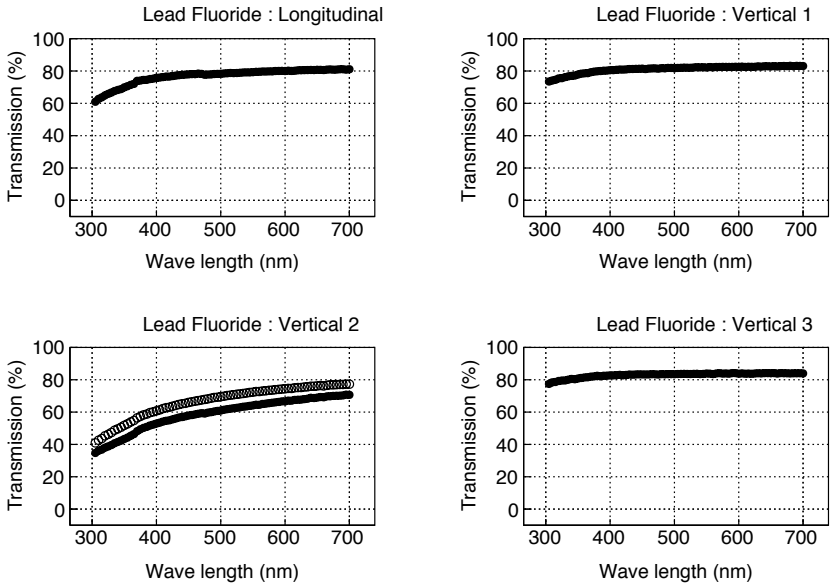

FIGURE 2.25: Transmissions of lead fluoride crystal. One longitudinal and three transverse transmissions were measured. White circles in the left bottom figure represent transverse transmissions measured 1 cm from the crystal center.

Fig. 2.22 shows transmissions of the acrylic plate (CLAREX). The longitudinal transmission was 90% in a wavelength region from 400 nm to 700 nm. When the wavelength became smaller than 400 nm the transmission was gradually reduced and reached 0% at 305 nm. The vertical transmissions were 80% at wavelengths above 400 nm and 35% at 305 nm.

The Transmission of the lead glass (SF57HTULTRA) are shown in Fig. 2.23. The longitudinal transmission was 85% above 600 nm, and became 0% at 370 nm. The vertical transmissions started to reduce below 470 nm and reached 0% at 360 nm.

In Fig. 2.24, the data of eco glass (STIH53W) are shown. The longitudinal transmission was around 85% at wavelength > 650 nm, decreased to 0% at 380 nm. The vertical transmissions was 85% at $lambda$ > 600 nm and decreased to 0% at 370 nm.

The transmissions of the lead fluoride crystals are shown in Fig. 2.25. Its longitudinal transmission was $\sim$ 80% at 700 nm, and decreased continuously. The minimal value was 60% at 305 nm. The transverse transmissions had a strong positional dependence, which was assumed occur during manufacturing. At position 1 and 3 transmissions were $\sim$74% and 78% at 305 nm. At point 2, we observed poor transmissions of 35 % at 305 nm, which was about half of the corresponding transmissions of at position 1 and position 3. We measured another point which was 1 cm off from the center of the crystal as a reference. The data points are shown by white points in the same figure. The transmissions were 8% higher than at the center. We assume that these were due to imperfections either on the surface or interior of the crystal.

2.5.5 Setup of photon yields measurements

The yields of Cherenkov photons against antiproton annihilations were measured using the setup of Fig. 2.26 [52, 53].

The AD provided a 200 ns long pulsed beam containing (2$\sim$3)$\times 10^7$ antiprotons with a kinetic energy of 5.3 MeV and a repetition rate of 0.01 Hz.

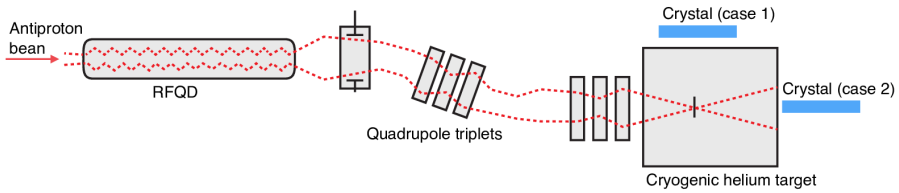

FIGURE 2.26: Experimental setup to measure responses of crystals against antiproton annihilations (not to scale). Dashed lines show trajectory of the antiproton beam. The incident beam was decelerated from 5.3 MeV to 70 keV, and transported by an achromatic analyzer to the target volume filled with liquid helium. In order to study differences when secondary particles came into the crystal from the largest and the smallest side, the tests were carried out at two different positions (case 1 and case 2 in this figure).

About 30 % of the beam was decelerated when it passed through the radio frequency quadrupole decelerator (RFQD). The analyzer consisting of three 1-T solenoid magnets was used to select only the 70 keV antiprotons. The $\sim$70% undecelerated antiprotons annihilated on the wall of the analyzer. The trajectory of the beam was measured by microwire secondary electron emission detectors [54, 55].

The beam was transported to a target chamber filled with ^{4}He gas at temperature $T \sim$ 15K and pressure $p \sim$ 1 mbar. Most of the antiprotons annihilated immediately when they arrived at the target volume. The resulting charged pions were used to investigate the photon yields of radiators against the antiproton beam.

A fine-mesh photodiode (Hamamatsu, R5505GX-ASSYII) was used for this test. The directional dependences according to the incoming charged particles were tested by changing the angle of the radiators relative to the target volume. In case 1 in Fig. 2.26, the short axis of the crystal pointed to the center of the target chamber. In case 2, a smallest side (3 cm$\times$3 cm) pointed to the center of the target chamber. The distance from the center of

the target volume to the entrance surface of the crystal was 15 cm in both cases.

Measurements with and without a transparent rubber sheet made of two-component silicone (Shinetsu Silicone CAT-103 and KE-103) were carried out in case 1. The rubber sheet was placed between the crystal and photo-multiplier to reduce the difference of refractive indexes. The rubber sheets were not used for the case 2.

An acrylic Cherenkov counter (sub Cherenkov counter) was also positioned to monitor the relative intensity and to be used for normalization of the signal strength.

2.5.6 Results of photon yields measurements

Fig. 2.27 (a) shows signal intensities measured for each radiator, normalized by using the signals of the auxiliary Cherenkov counter. For case 1, the number of Cherenkov photons in the PbF2 crystals was the highest due to its high refractive index. The yields for the fused silica and the acrylic plate were about one third of PbF2. The photon yield for the glasses (S-TIH53W and SF57HTULTRA) were less than one fifth compared to the yields in PbF2. The white circles represent the results the same measurements carried out with the transparent rubber, for which no significant difference was observed.

Fig. 2.27 (b) shows the results in case 2. The yields in the fused silica were almost the same as for PbF2. This is due to the lower photon transmission in PbF2. In the experiment of the antiproton-nucleus annihilation cross section measurements, it was necessary to cover a large solid angle. Therefore the short axis of the crystal (3 cm$\times$16 cm) pointed to the center of the beam dump as in case 1.

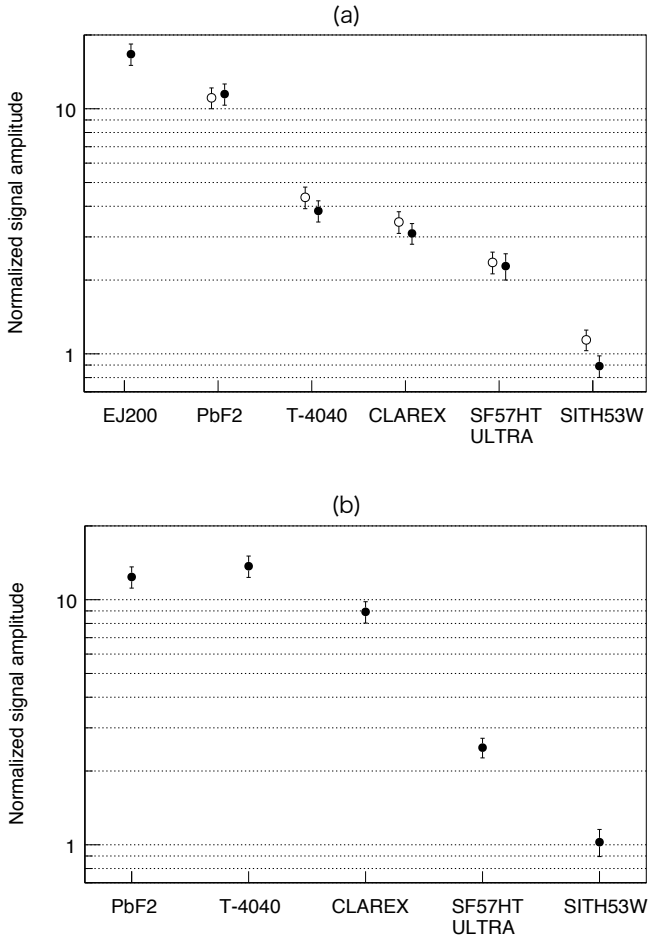

FIGURE 2.27: Relative signal intensity of each crystals. The crystal was positioned as, (a) for case 1 or (b) for case 2 (see text). The signals were normalized by a different Cherenkov counter. White points shows relative intensities, and black points results show results of same measurement but with rubber transparent sheet. Results of measurement with a scintillation bar (EJ-200) is also shown as a reference in the case of Figure (a).

2.5.7 Types of photodiodes

The two p-i-n photodiodes and an avalanche photodiode tested in this study are listed in Table. 2.3.

Photodiodes	Size [mm×mm]	Depletion layer [μm]
p-i-n photodiode (S3204-08)	18×18	300
p-i-n photodiode (S3590-08)	10×10	300
avalanche photodiode (S8664-1010)	10×10	5

TABLE 2.3: Three types of photodiodes, their sizes and thicknesses of the depletion layers

A schematic cross section of a p-i-n photodiode is shown in Fig. 2.28 (a). When a reversed bias is applied to the P and N layers the depletion layer thickness enlarges to typically $\sim$ 300 μm, and so its capacitance C_t decreased. The timing response f_c of the photodiode increases since it is inversely proportional to the capacitance. The fast timing would be an advantage during the annihilation cross section measurement in which a number of particles ($\sim 10^6$) would hit the detector in a short time duration ($\sim$ 200 ns).

We tested the S3204-08 (Hamamatsu Photonics) p-i-n photodiode. It had an active area of 18 mm $\times$ 18 mm with a surface covered by epoxy resin. Its C_t and f_C was 130 pF and 20 MHz. The sensitive spectral range λ_s was from 340 to 1100 nm, and its peak sensitivity was at 960 nm. The other p-i-n photodiode S3090-08 had a smaller active area of 10 mm $\times$ 10 mm. Its C_t and f_C was 40 pF and 40 MHz. Its sensitive wavelengths λ_s was also from 340 to 1100 nm, and its peak sensitivity was at 960 nm. In both cases the thicknesses of depletion layers were 300 μm.

An avalanche photodiode, S8664-1010, was also tested. It multiplies the carriers generated by incident photons (Fig. 2.28 (b)). An electron and a hole were collected to the N and the P layer. The drift speed of the electron increased with the supplied voltage. At a certain voltage, the probability to hit lattices in the avalanche layer increases and the drift speed was saturated.

If the applied voltage becomes higher, the carrier produced another electron-hole pair via ionization when it hit the lattice, which leads to the avalanche multiplication. This called ionization. It is possible to make this process repeat itself with even higher voltage. The multiplication is called avalanche multiplication. Avalanche photodiodes therefore achieve better signal to noise ratio (S/N ratio) than for p-i-n photodiodes. Since the gain of the avalanche photodiode depends on their temperatures (see Appendix. G), it is essential to control the temperature with a precision of ± 1 degrees to make the systematic error less than 5 %.

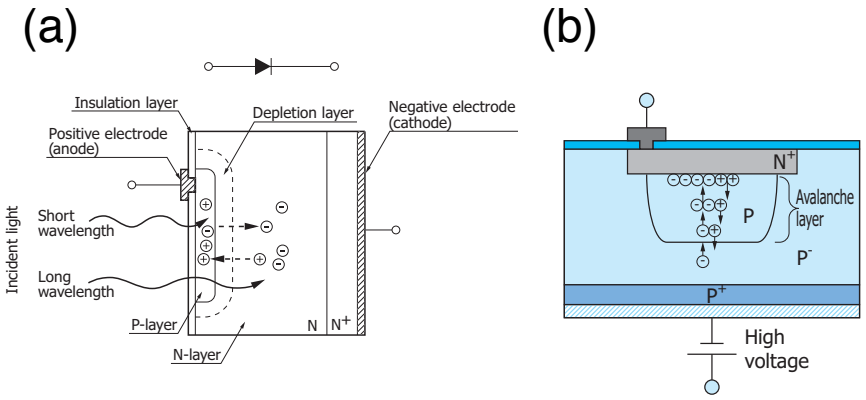

FIGURE 2.28: (a) Schematic cross sectional view of the p-i-n photodiode. This figure was taken from a handbook of Hamamatsu photonics [56]. (b) Schematic view of an avalanche photodiode taken from a handbook of Hamamatsu Photonics [57].

2.5.8 Linearities of photodiodes

The linearities of the photodiodes were measured using the setup shown in Fig. 2.29. This method is called double aperture method [58, 59].

A light emitted diode (LED, ROHM SLI-506) produced a 100 ns long light pulse of emission wavelength 470nm, and emission angle 40 degrees. A neutral density filter wheel (NDC-100C-4M) of diameter 100 mm and an optical density range d = 0.0∼4.0 was used to adjust the light intensity. A 50 mm diameter integral sphere (Thorlabs IS200) with an internal surface reflectivity of 99% was placed just downstream of the filter. Its internal sphere was covered with a white diffusive coating, where the incident light underwent multiple scatterings, randomizing its direction and polarization.

Part of the light was extracted from the sphere using two optical fiber bundles made of fused silica. The coupling positions and angles of each bundle inside the chamber was identical to produce similar beams. The signal produced by the photodiode was read by the same setup in Fig. 2.18. The analog signal was measured using an oscilloscope. The detected waveform was recorded, and the total intensities (S) was obtained by integrating it.

We then blocked one of two light beams using a rubber sheet and the intensity (S_1) recorded. We next removed the sheet and blocked the other incident beam instead, recording the resulting signal S_2. If the signal is linear against a certain intensity of the incident light, S should be the sum of two signals, i.e. $S = S_1 + S2$. But if the photodiodes were saturated it leads to $S < S_1 + S_2$.

Results of linearity measurements are shown in Fig. 2.30. In the horizontal axis, intensities of the incident photons in pC are shown. The vertical axis ratio describes $S/(S_1+S_2)$. The upper, middle, lower figures represent the results with a large p-i-n photodiode (S3509-08), a small p-i-n photodiode (S3204-08) and the avalanche photodiode (S8664-1010). The avalanche photodiode saturated at 40 pC. For the p-i-n photodiodes, saturation could not be observed up to > 200 pC.

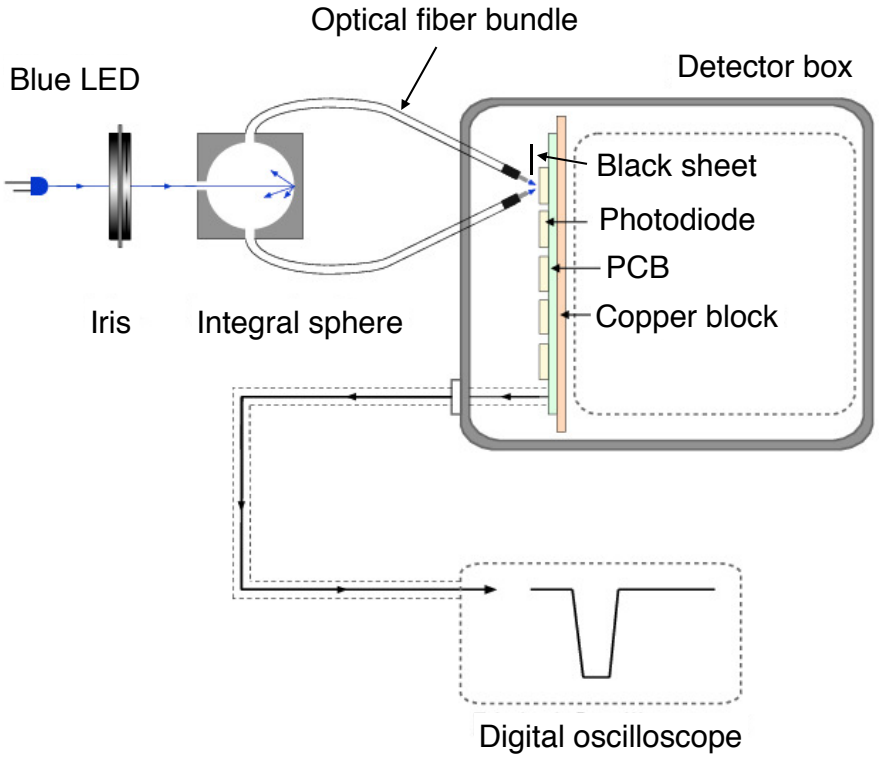

FIGURE 2.29: Setup of the measurement of the linearity of the photodiodes. Light from a blue LED enters an integral sphere after it passed through an iris. The output from the sphere was transmitted along a pair of optical fiber bundles. The light irradiated the photodiode. The obtained signal was read by a digital oscilloscope.

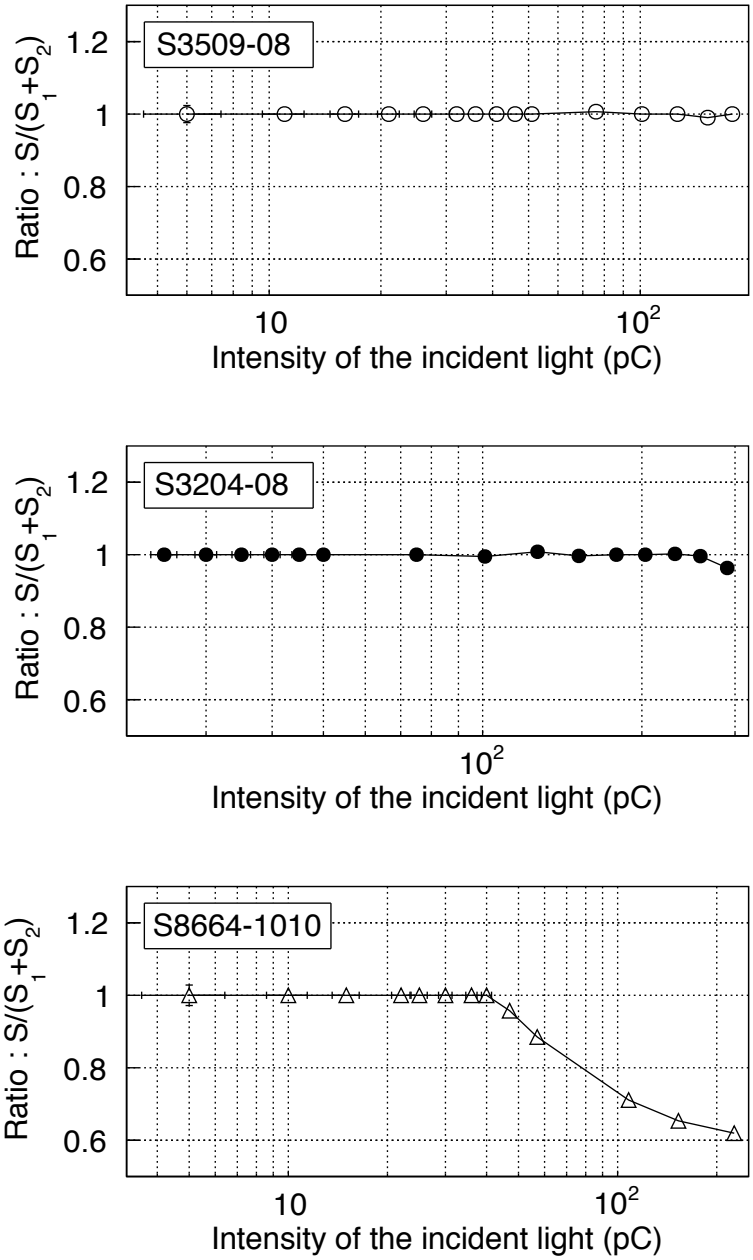

FIGURE 2.30: Results of linearity measurements. Horizontal axis indicates intensities of the incident light in pC. In the vertical axis, the ratio $S/(S_1+S_2)$, is shown. Triangles indicate the results of APD, A black circles the small p-i-n photodiodes (S-3590-08), white circles the large p-i-n photodiodes (S3204-08).

2.5.9 Responses of photodiodes against the antiproton pulsed beam

We measured the nuclear counter effect (NCE) against antiproton annihilations, for the three types of photodiodes in Table. 2.3. The background measurements were carried out with and without crystals for each photodiode.

Fig. 2.31 shows spectra obtained with PbF2 crystals. Spectra with and without the PbF2 crystals are indicated by black and red lines. The left, middle and right figures correspond to the result with large p-i-n photodiodes (S3509-08), small p-i-n photodiodes (S3204-08) and an avalanche photodiodes (S8664-1010). For p-i-n photodiodes, most of the signals originated from NCE. This is caused by direct hits of charged particles on the 300 μm depletion layer [45]. The avalanche photodiode has a relatively thin depletion layer of $\sim$ 3 μm, so that the NCE is reduced. Its intensity was $\sim$ 15 % of the total signal measured with PbF2 crystals.

Fig.2.32 show the results of background measurements with plastic scintillators (EJ-200). The black spectra were obtained with scintillators, and red spectra were measured without them. Two p-i-n photodiodes (S3509-08 and S3204-08) and an avalanche photodiode (S8664-1010) were also tested. Due to the larger photon yield of the scintillators, the contributions of the NCE became much smaller.

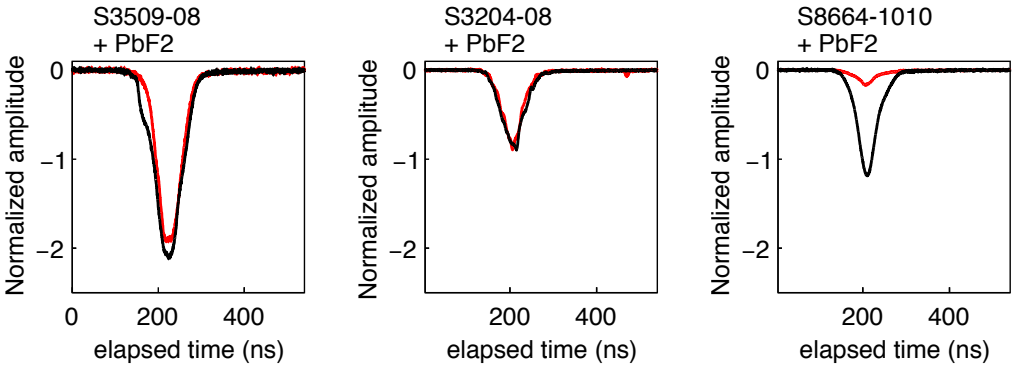

FIGURE 2.31: Measurements of NCE backgrounds of photodiodes. Black lines are spectra with PbF2 crystals and red spectra show results of background measurements with no crystal.

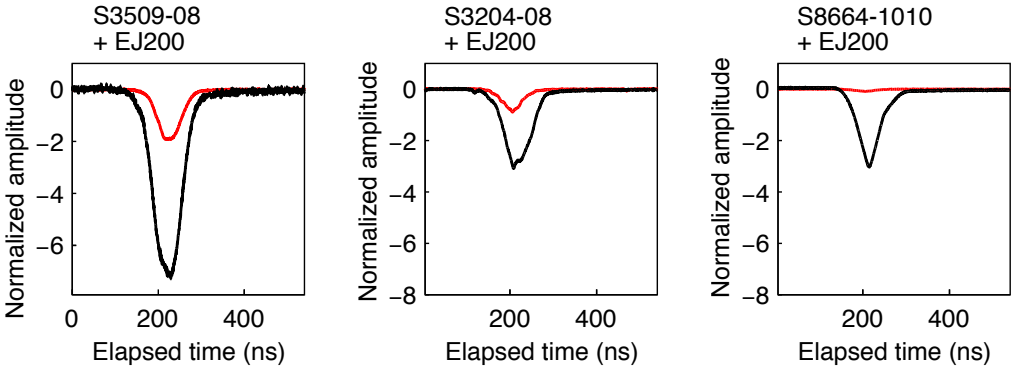

FIGURE 2.32: Measurements of NCE backgrounds of photodiodes. Black lines are spectra with scintillators (EJ200) and red spectra show results of background measurements. with no scintillators

We decided to use avalanche photodiodes to reduce the NCE and the PbF2 crystals as radiators to maximize the photon yield. The ratio between the signal and NCE could be increased by the applied voltage. We measured this effects under a same experimental setup in Fig. 2.26.

The white circles of Fig. 2.33 indicate the signals of NCE measurements without any radiator for anode voltages of 50 V to 400 V applied to the photodiode. The black circle indicate the results with the PbF2 crystals. White triangles are data with the scintillators. The signals were normalized by the spectra obtained by the auxillary Cherenkov counter as in Section. 2.5.5.

The NCE effect was linear to the antiproton intensity. It however introduces a background whose statistical fluctuations differs relative to the case of NCE = 0. The NCE/signal ratio was 15 % at 400 V, and 60 % at 50 V.

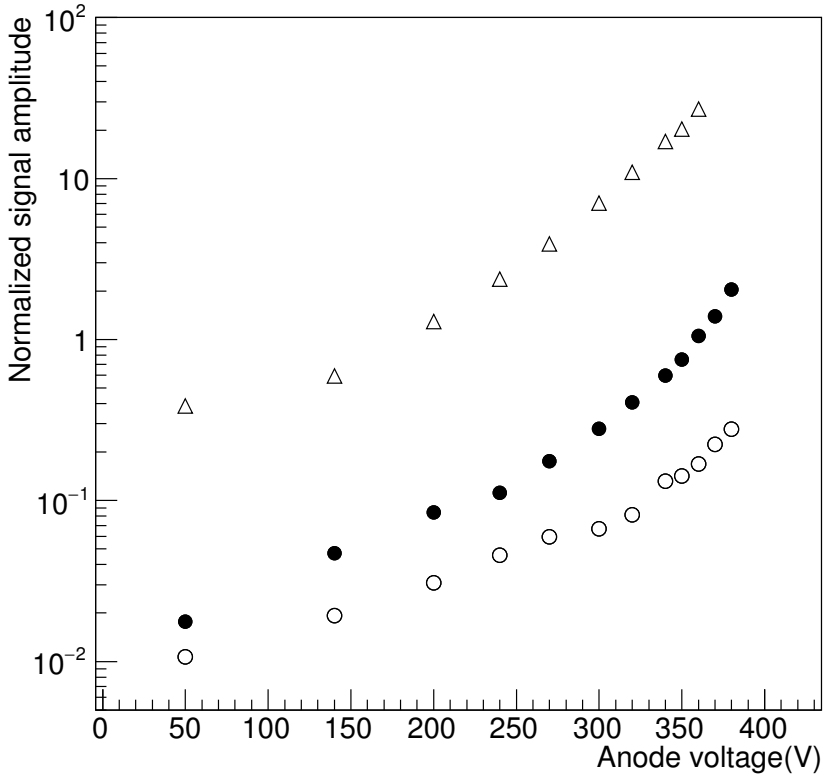

FIGURE 2.33: Normalized Cherenkov signal as a function of the anode voltage applied to the avalanche photodiode. The Cherenkov counter used in the antiprotonic helium was also used to normalize the signals. Triangles indicate results when scintillation bars were used. Black circles indicate signal strength of PbF2 radiators, white points the background measurements with no radiator.

Chapter 3

Data analysis

As shown in Eqn. 2.2, the ratio between $\mathrm{N_{anni}}$ and $\mathrm{N_{Ruth}}$, i.e. ,the number of hits from the target and from the 2nd ring, are necessary to derive the annihilation cross section. They were measured in different experimental runs, and the data normalized by the beam intensities.

The absolute value of the elastic scattering cross section (σ_{Ruth}) was derived numerically, and systematic errors caused by the beam shape and uncertainties of the positions of the experimental apparatus were estimated.

Data was measured over three shifts. Since the thicknesses of the target foils, beam were varied daily, we derived the annihilation cross section for each day and calculated the weighted mean value.

3.1 Data set

The measured data sets and the configuration of targets are shown in Table 3.1. $\mathrm{N^{shot}_{C+2nd}}$, $\mathrm{N^{shot}_{C}}$ and $\mathrm{N^{shot}_{BG}}$ represent the number of antiproton shots measured with a target and the 2nd ring, with only a target, and with an empty ring of inner diameter of 4 cm. The diameter was smaller than for the 2nd ring and frame for the target, so that any backgrounds caused by the halo of the beam could be measured. Two thicknesses of carbon foils (700 nm and 1 μm) were used.

Date	N^{shot}_{C+2nd}	N^{shot}_{C}	N^{shot}_{BG}	Thickness of target
Nov18	68	57	12	1 μm
Nov19	51	60	16	700 nm
Nov22	35	85	22	1 μm

TABLE 3.1: Data sets used for the analysis. They are shown with the numbers of antiproton pulses, types of targets. N^{shot}_{C+2nd}, N^{shot}_{C} and $N^{shot}_{background}$ represent the number of pulses with the target and 2nd ring, with only the target, and with the ring whose inner diameter of 4 cm for background measurements respectively.

3.2 Time spectra of antiproton annihilations

Time spectra of antiproton annihilations were obtained by counting timings of the hits on each scintillator bar. Fig. 3.1 shows the raw time spectra obtained on Nov22 by summing all the hits detected by each bar.

Fig. 3.1 (a) is a spectrum measured with the target and 2nd ring. Around $500 \sim 570$ ns, there is a peak which corresponds to the annihilations of antiprotons in the target and 2nd ring. The peak is clearly separated from the large signal starting from 600 ns, which was generated by annihilations at the beam dump. The signal was saturated due to a large number of annihilations ($\sim 10^6$) there.

Fig. 3.1 (b) shows the time spectrum with a target but without the 2nd ring. Signals in the target can be observed as well. After the peak, there is a continuous spectrum between the two peaks. This corresponds to annihilations of antiprotons at the lateral wall.

Fig. 3.1 (c) shows a result of a background measurement using the empty ring. No annihilations were observed at the target position. Therefore we concluded that the effect of the beam halos was negligible.

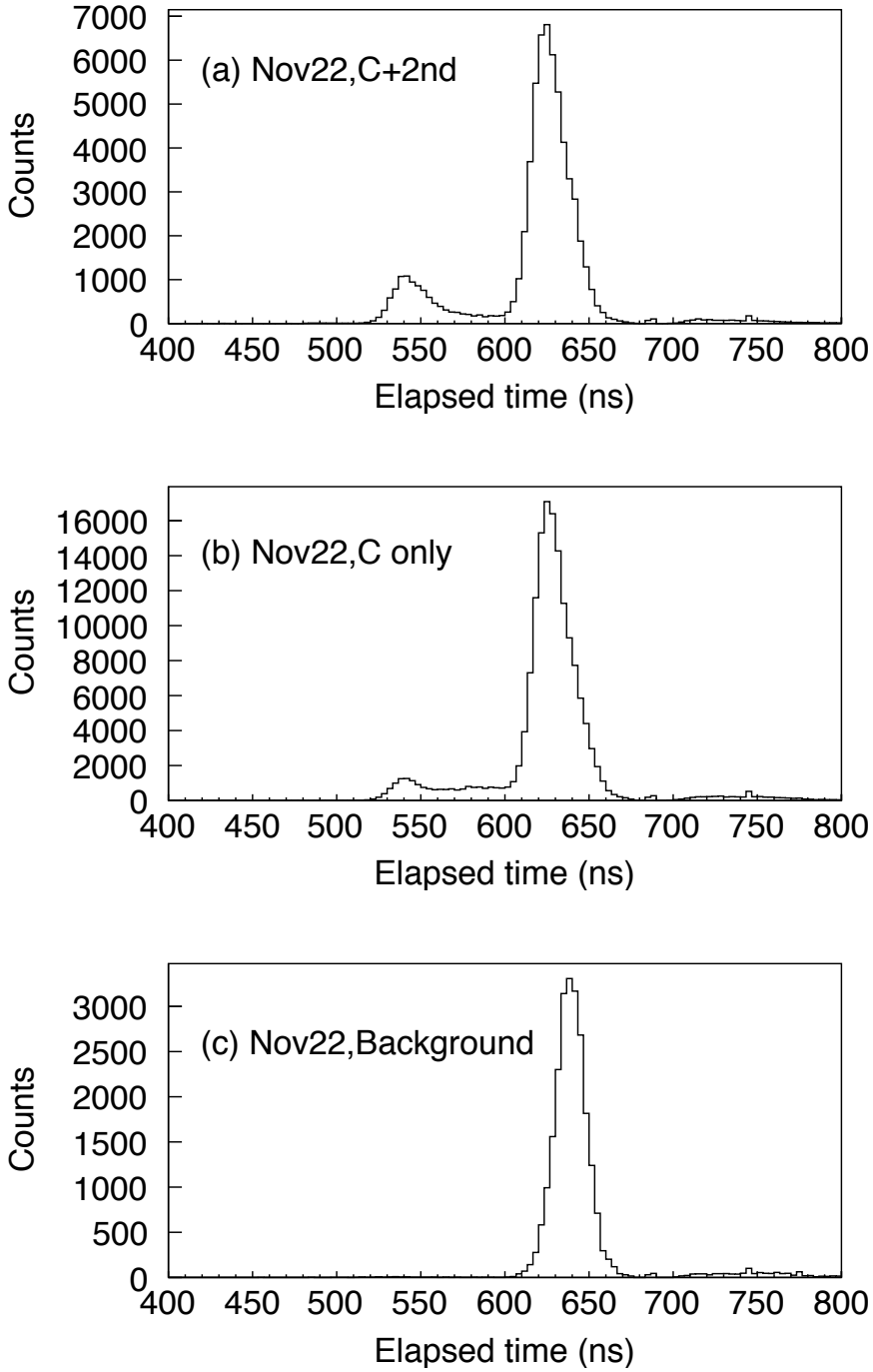

FIGURE 3.1: Spectra obtained by plastic scintillators. Figure (a) shows a spectrum when a carbon foil of 1000 nm thickness and 2nd ring were used. Figure (b) shows a spectrum without 2nd ring but with the same foil. Figure (c) is a background measurement.

3.2.1 Analysis of signals detected by scintillation planes

3.2.2 Scintillation planes

Since the signals at the target position was well separated from the backgrounds, no analysis to reconstruct the vertex of the annihilation point was necessary. Therefore, in this analysis we used only the hits on scintillator P6, P8 and P13 (see Fig. 2.8) were placed along the sides of the target chamber and covered solid angles of 8%, 5% and 10%. When a scintillation bar counted the hit, the DAQ scheme recorded the timing when 0 changed to 1. We assume that this timing corresponds to the time when a particle hit the counter. We summed all the timings of hits of P6, P8 and P13 and made time spectra.

In this process to count the hits, the following corrections were necessary to be taken into account.

3.2.3 Corrections for the numbers of hits

The dead time of each scintillation bar was $\sim$50 ns. Therefore if one scintillation bar accept one hit it was not possible to take the second hit within the integration range of 15 ns, which is explained in the following section. In order to calculate the actual number of hits from the number of detected particles, Monte-Carlo simulations were carried out by the INFN group and occupancy correction factors were estimated.

In the simulation, not only the saturation effects but also the probability of a single pion being doubly counted by neighboring bars was estimated. Since each bar closed to each other one charged particle may pass the two bars at the same time. For these reasons the occupancy corrections were calculated for each plane.

The Monte-Carlo simulation was carried out as followings.

- The geometries of each plane P6, P8 and P13 were generated to reproduce the real experimental setup as shown in Fig. 2.7. They covered 8%, 5% and 13% of the total solid angles.

- P6, P8 and P13 consisted of 56, 62 and 62 scintillation bars.
- A given number of annihilations was generated and six pions were generated per one annihilation. We assume these pions are isotropically generated, thus the number of pions which hit the detector is exactly determined by the detectors' solid angles.
- If a pion hit the detector, it does on a random position (= random bar number). If a bar is hit, also the next bar is hit 20% of the cases. This is due to the fact that the detector has 3d-dimentsional bars which cause a crossing pion to pass through more than one bar.
- Once a bar counted the hit it can not take the next hit, which represents the saturation effects.
- The numbers of annihilations and resulting charged particles were changed by hand. We plot the numbers of the actual hits and detected hits. The results are shown in Fig. 3.2.
- In Fig. 3.2, the number of annihilations at the target position is described in the horizontal axis. The red and blue lines correspond to the number of actual hits on the planes and the number of detected particles.
- In order to convert the detected number to the actual number, a coefficient (occupancy correction number) was calculated for each number of detected particles. Factors to calculate the number of actual hits (red) from the number of detected particles (blue line) were calculated for each number of detected particles.
- Same procedures were carried out for P6, P8 and P13. Therefore we obtain three occupancy corrections for each plane.

Fig. 3.3 shows results of correction coefficients for each plane. In the horizontal axis the number of detected hits on the scintillators is shown. The

vertical axis represents the actual number of hits estimated by Monte-Calro simulations. When the number of hits on a plane is smaller than ~ 15, the number of hits needed to be decreased due to eliminate events which caused multiple hits. On the other hand when the number of hits becomes large the effect of saturation becomes large and the actual number is larger than the detected one. This simulation was carried out for P6, P8 and P13.

Those corrections were applied for the data shot by shot. We found that the number of hits when we used both the target and 2nd ring was estimated to be lower. This is because of the additional annihilations on the ring. Comparing to the data with only the target, the number of hits with the target and with the 2nd ring needed to be increased by 9%,7% and 11%.

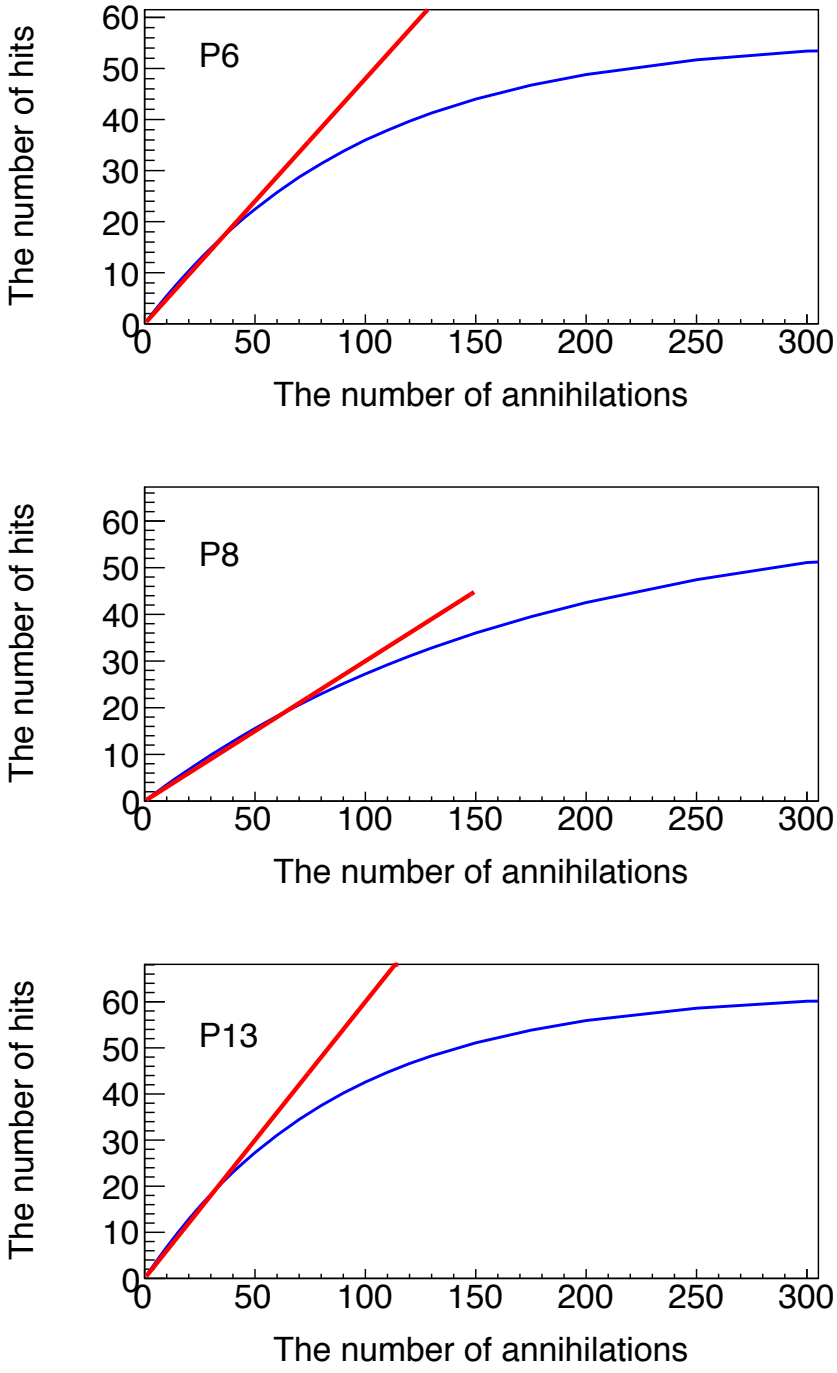

FIGURE 3.2: ctions for the numbers of hits for each scintillator plane. The coefficient numbers to derive the number of actual hits from the number of detected particles during the experiment are shown. The correction coefficients are simulated for each plane.

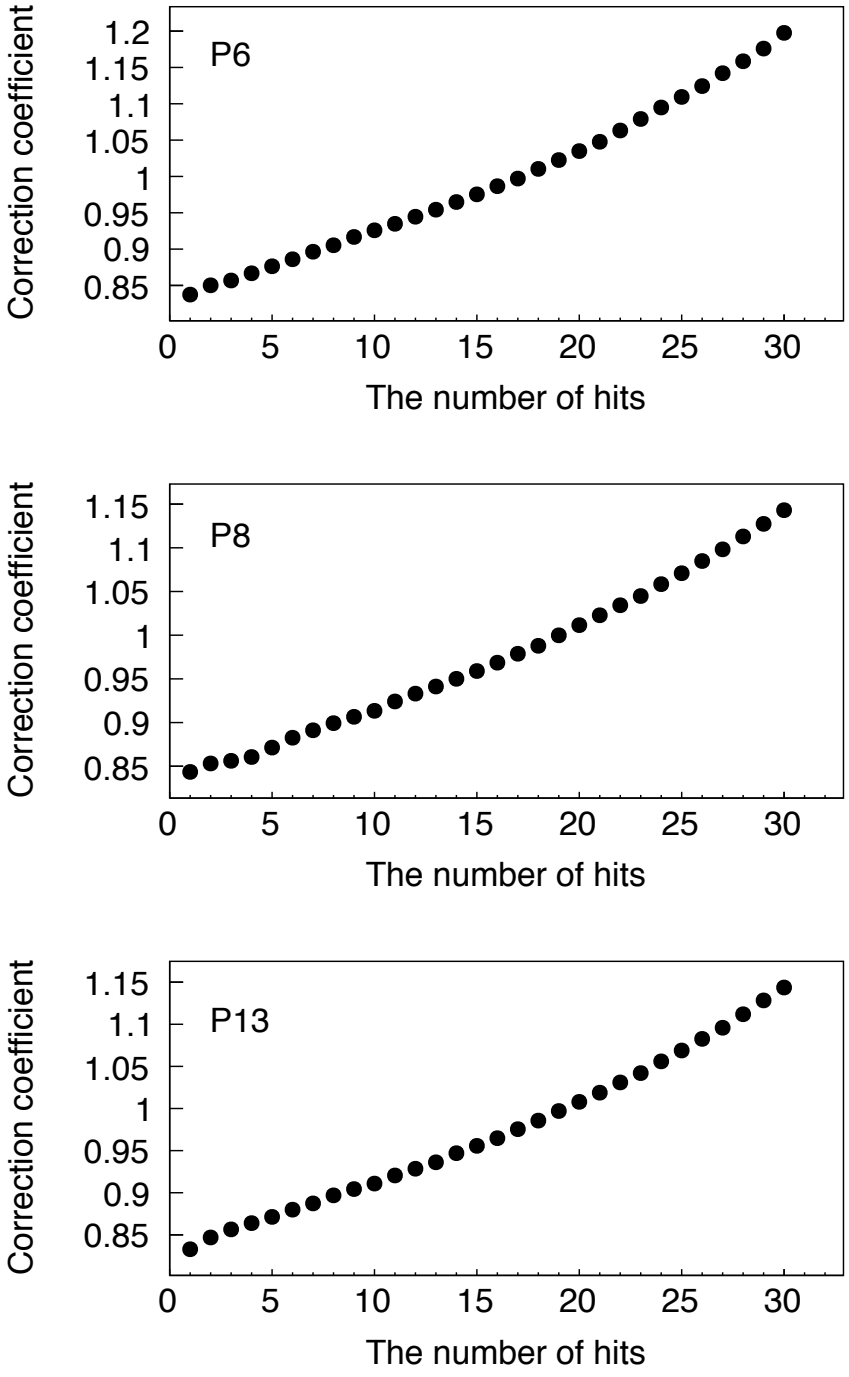

FIGURE 3.3: Corrections for the numbers of hits for each scintillator plane. The coefficient numbers to derive the number of actual hits from the number of detected particles during the experiment are shown. The correction coefficients are simulated for each plane.

3.3 Beam intensity

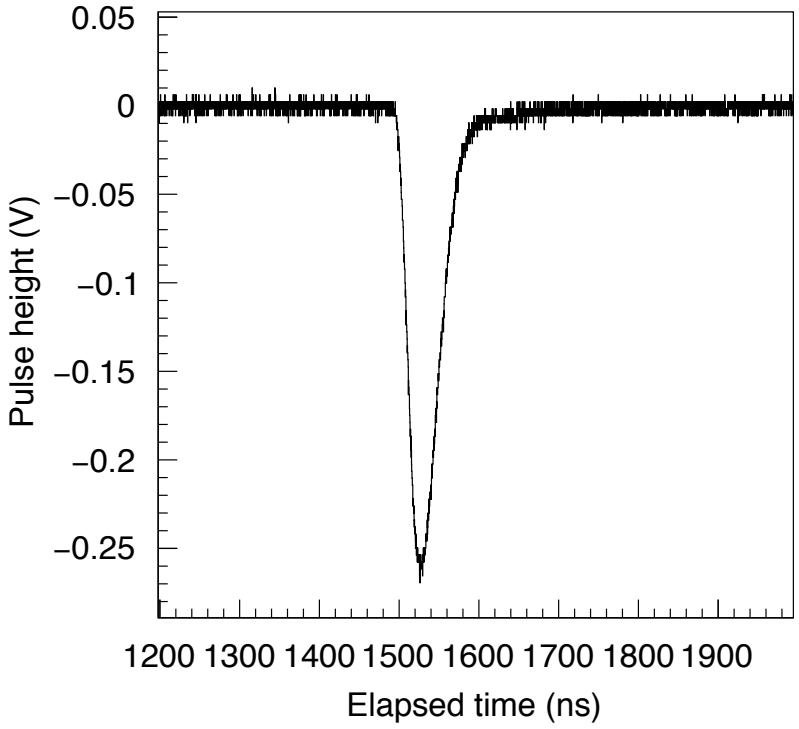

FIGURE 3.4: Typical spectrum of the antiproton pulsed beam measured by the Cherenkov counter. The relative intensity of the beam was measured by integrating this spectrum.

Fig. 3.4 shows a typical time spectrum obtained by the Cherenkov counter for an antiproton pulse. The weighed center of the signal was determined by fitting the following formula which represents both rising and falling edges of the signal.

$$f(x:\mu,\sigma,\lambda) = \frac{\lambda}{2} e^{\frac{\lambda}{2}(2\mu+\lambda\sigma^2-2x)} \times \mathrm{erfc}\Big(\frac{\mu+\lambda\sigma^2-x}{\sqrt{2}\sigma}\Big) \tag{3.1}$$

where λ and σ denote parameters. Here μ denotes the mean of the Gaussian distribution which is close to the time where the signal height is maximized. The erfc in Eqn. eqn:EMG is a complementary error function.

$$\mathrm{erfc}(x) = \frac{2}{\sqrt{\pi}} \int_x^\infty e^{-t^2} dt \tag{3.2}$$

The signal intensity was obtained by integrating the spectrum from μ-50 ns to μ+100 ns. Small contributions from its DC offset was estimated and included in the errors of the obtained signal strength.

Fig. 3.5 shows the intensities of each antiproton pulse during the experiment in pC. We rejected events when the beam intensity was less than 1 pC due to issues of the accelerator.

The statistical error due to the number of particles which hit the detector was 0.3%. Shifts in the gains of photodiodes caused by a temperature fluctuations ($\pm$ 0.5 degrees) caused an error of 1.9%. Resolution of a digital oscilloscope (0.3%), reading errors of the linearity-measurement (0.3%), contributions from the DC offset ($\sim$ 0.8%) and a linearity of the pre-amplifiers (0.1%) were taken into account.

The uncertainties of intensity caused by NCE was dominated by the statistical error. The avalanche photodiode detect $\sim$ 400 charged particles, and its statistical error was 5%. The component from NCE was $\sim$15% of the total intensity, and the error caused by the NCE was derived to $\sim$0.8% to the total intensity.

The errors are summarized in the Table. 3.2.

Selections of data with and without the ring are shown in Fig. 3.5. Those intensities were summed and used to normalize the spectra. In Table. 3.3 sums of the Cherenkov intensities during each measurement are listed.

Gain shift due to fluctuations of temperature	1.9 %
Statistical error (the number of pion' hits)	0.3 %
DC offset	0.3 %
Resolution of a digital oscilloscope	0.2 %
Reading error of linearity measurements	0.2 %
Linearity of preamplifier	0.1 %
Nuclear counter effect	0.8 %
Total	2.3 %

TABLE 3.2: Typical errors contribute to the total error of the beam intensity are listed. Gain shift of the avalanche photodiode was estimated to 1.9 % using the data book of Hamamatsu-photonics (see Appendix G). Statistical errors were derived by the number of hits of charged particles. DC offset was evaluated from the spectrum during the beam tuning as $\sim$ 0.5 pC. Other small contributions, a reading error of the linearity measurement, resolution of the oscilloscope and a linearity of the preamplifier (OPA842) are listed. This value was estimated for the case when the intensity was 14 pC.

	Nov18	Nov19	Nov22
C+2nd (pC)	945.60(2.64)	704.20(2.27)	463.3(1.83)
C Only (pC)	785.41(2.39)	840.12(2.50)	1003.06(2.59)

TABLE 3.3: Beam intensities for each day. The date and intensities of the beam are listed together.

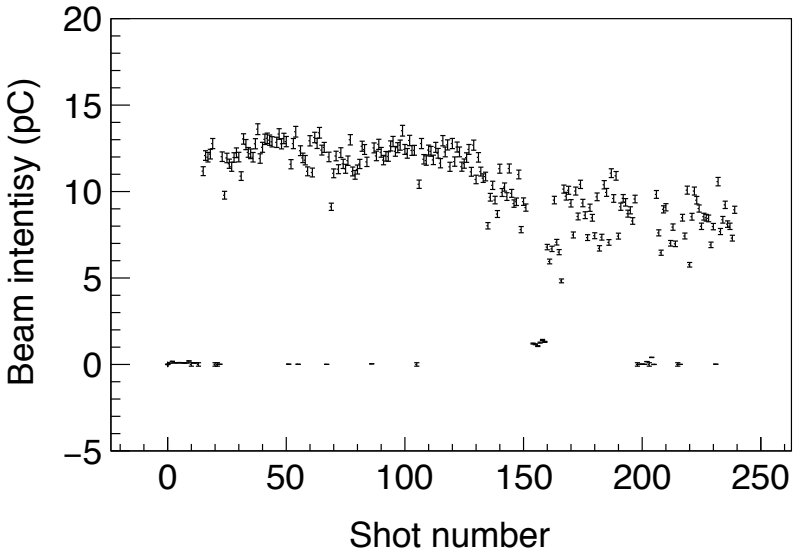

FIGURE 3.5: The beam intensity for each antiproton pulse. The first 25 shots were used for a beam tuning. Form shot 27 to shot 63, a carbon target of 1 μm thickness and 2nd frame were inserted. From shot 64 to shot 69, only the second frame was used for the background measurement. From shot 70 to 241, only a target foil was used. The last 6 shots from 251 to 256 were used for a background measurement again to study the reproducibility.

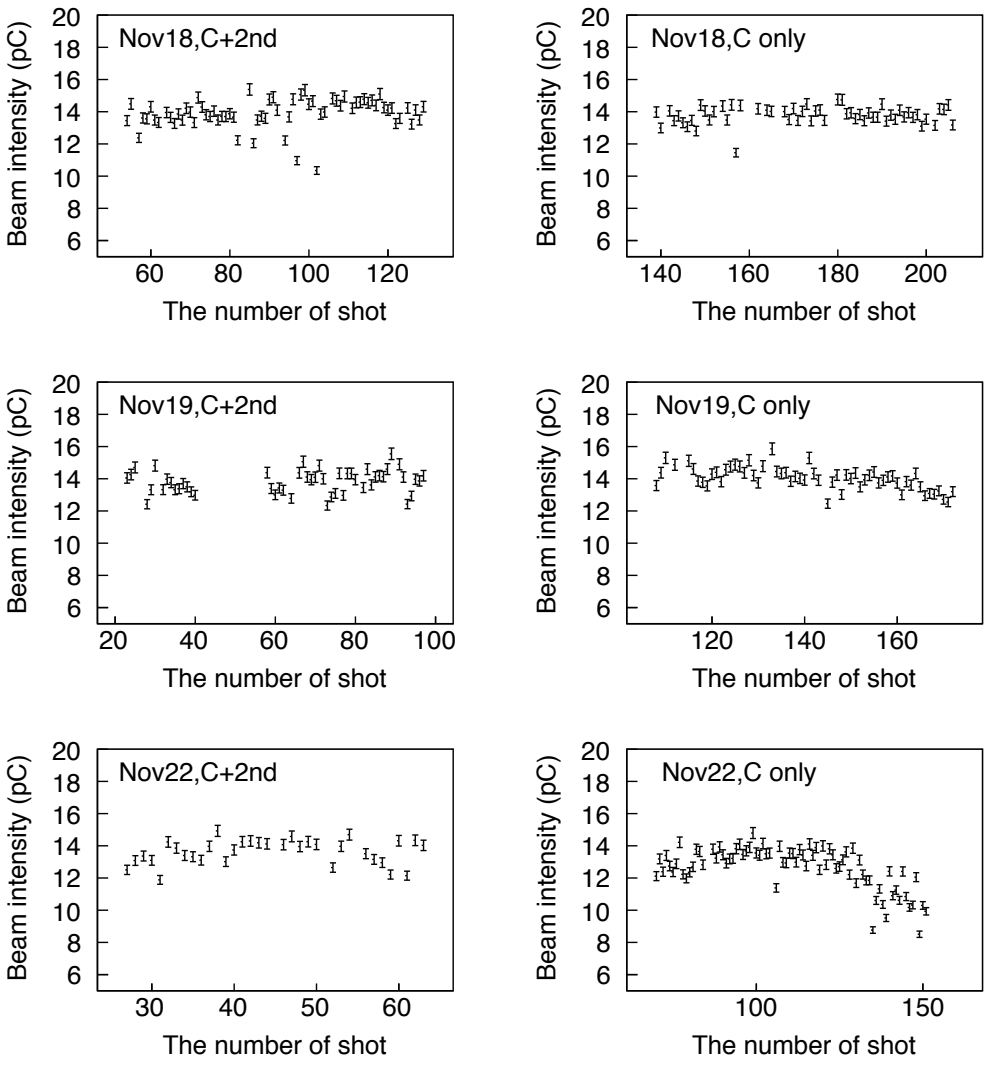

FIGURE 3.6: Intensities of antiproton beams with and without the 2nd ring on each day measured by the Cherenkov counter.

3.4 Normalized spectra

The spectra of each day after normalization are shown in Fig. 3.7. The solid line correspond to data with only the target, and the dashed line represents a spectrum with the target and the 2nd ring.

A ratio of $\mathrm{N_{anni}}$ and $\mathrm{N_{Ruth}}$ can be derived as,

$$\frac{\mathrm{N_{anni}}}{\mathrm{N_{Ruth}}} = \frac{\mathrm{T}}{\mathrm{F} - \mathrm{T}'} \tag{3.3}$$

where T denotes the number of counts caused by annihilations at the target, which can be derived by integrating the spectra shown in solid lines in the corresponding range, F the counts from the target and the 2nd ring obtained by integrating the spectra indicated by dashed lines. T' denotes the counts from the target which was included in F.

3.4.1 Start timing of integration

Antiprotons that annihilated at the beam dump saturated the detectors. The time-of-flight between the target position and the beam dump was 80 ns, from which the arrival time of the antiprotons at the target was derived.

The timing was determined by fitting the slope of the saturation by a linear function indicated by a solid line in Fig. 3.8. It shows that the detectors saturated at 600 ns (t_{dump}), and the timing when the pulsed beam reached at the target (t_{target}) was estimated to be 520 ns.

3.4.2 Integration range to count the number of hits

We integrated a 15 ns time window for the 50 ns long antiproton pulsed beam to avoid counting background events from the lateral wall. The reasons for selecting 15 ns was as follows.

- It took at least 20 ns for the scattered antiprotons to reach the lateral wall. The time range of integration has to be smaller than this.

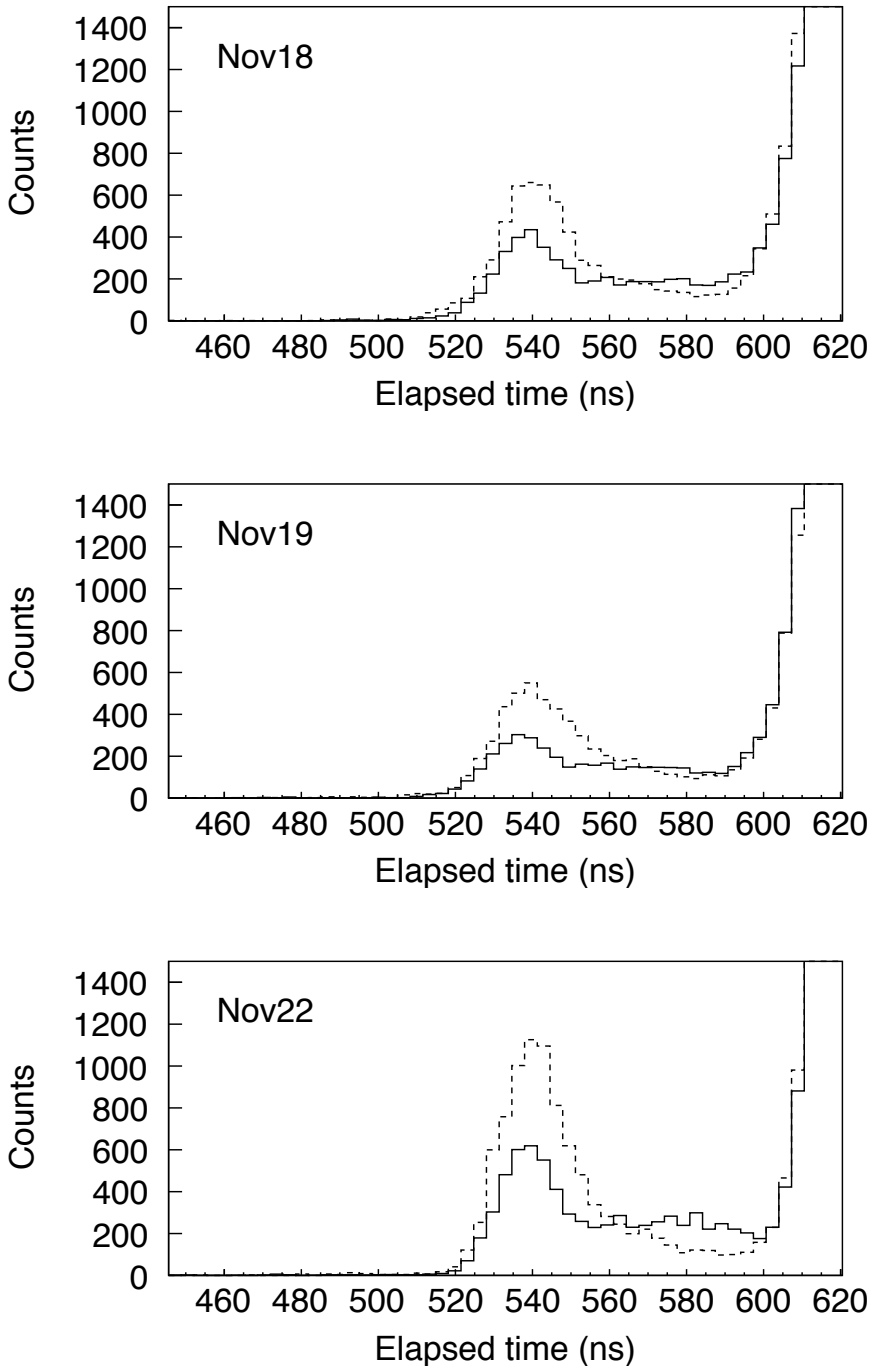

FIGURE 3.7: Time spectra obtained by the scintillation detectors. They are normalized by the beam intensities. The solid line indicates signals with only the carbon target, and the dashed line represents signals with the target and the 2nd ring. Three spectra for each day are shown.

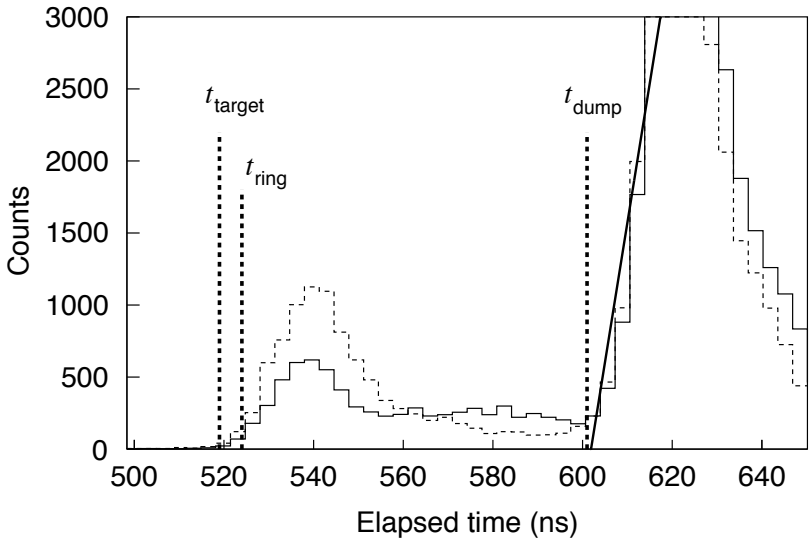

FIGURE 3.8: Method to determine the start timing of the integration. A linear function was used to fit the slope of the histogram and derive the timing when the beam reached the beam dump. The time when the front edge of the pulsed beam reached the target was calculated.

- The second frame was positioned 15 cm downstream of the target. This corresponds to a time-of-flight 5 ns. In order to count the number of hits on the 2nd ring, the time range of integration needs to be extended 5 ns backwards with respect to the target only runs ($t_{\rm ring}$ in Fig. 3.8).

- To derive T' we integrated the spectrum in a same time range used to count F. Since this range starts 5 ns later than $t_{\rm target}$, a 15 ns time region avoids counting the hits from the lateral wall.

3.5 Uncertainties of the timings

In this experiment we identify the particles by using only the timing information. Therefore it is important to consider the dependences of the ratios on the timing uncertainties, and we need to put correct systematic errors. In order to evaluate them, we took care of two issues. One is the uncertainties of the starting point of the integrations, and the other is the synchronization of two histograms with and without the 2nd ring.

3.5.1 Uncertainties of the start timing

In Fig. 3.8 the $t_{\rm start}$ was evaluated from the time of flight of antiprotons from the target position to the beam dump, however the $t_{\rm start}$ had some uncertainties caused by the timing resolution of the scintillation counters as a whole. A rough estimation of the resolution was done by using the peak structures obtained by the scintillation counters and a time-profile of the beam measured by the acrylic Cherenkov counter.

Fig. 3.9 shows the comparison. The FWHM measured by the Cherenkov counter was 16 ns (FWHM1), but in the case of the spectrum obtained by the scintillation counters it became 18 ns (FWHM) due to its timing resolution. Therefore, the resolution of the detector ($\sigma_{\rm detector}$) as a whole was derived by the following equation.

$$\sigma_{\mathrm{detector}} = \sqrt{\mathrm{FWHM2}^2 - \mathrm{FWHM1}^2}/2.35 = 3.5\mathrm{ns}. \tag{3.4}$$

As a uncertainty of the start timing, we decide to put 5 ns uncertainty conventionally. When we change the t_{start} we moved it earlier timing. In the region the statistics would be decreased while the contributions of the backgrounds would also be smaller. The scanning to the earlier timing will enabled us to make a good reference in the low statistic region. There we changed the start timing from 515 ns to 520 ns and studied the fluctuations of the ratio.

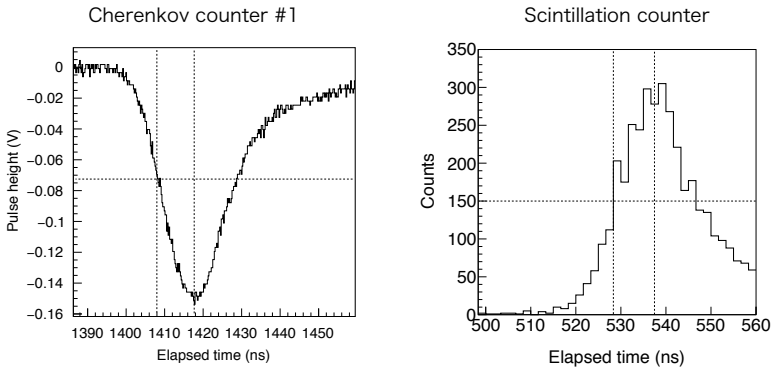

FIGURE 3.9: Time profiles of the beams measured by the Cherenkov counter under the target volume (left) and scintillation counters (right). The dashed lines were shown to indicate positions of FWHMs.

3.5.2 Synchronization of the spectra

We discuss the timing difference of the spectra with and without the 2nd ring here. This systematics is necessary to be taken into account since we focused on the rising edge of the spectra, and it changed drastically day by day and time to time. In Fig. 3.10 the normalized spectra in a long scale

are shown, and they showed that the shapes of the rising edged are different day by day. We assume that this is caused by the kicker timing of the AD and trajectories of the beams. In order to guarantee the same shapes of the beam with and without the 2nd ring on each day, synchronizations of the spectra were important especially at the rising edge since at the rising edge the changes of the slope will change the number of counts drastically.

To study the uncertainties of the synchronizations, we fit the peaks at the target positions and at the beam dump with and without the 2nd ring by the gaussian functions. By comparing the mean values with and without the 2nd ring, the accuracy of the synchronizations were evaluated. In Table. 3.4 shows the results of fit. This reveals that the synchronization was guaranteed within 1 ns. Therefore we assumed that the synchronization was guaranteed within 1 ns conservatively.

In order to study effects of the difference of 1 ns, we carried out a following analysis. We fix the timing of the solid spectra (run with only the target) and changed the timing criteria of the dashed spectra (run with the 2nd ring) $\pm$ 1 ns and calculated the ratios in a same way as described above. The difference of the synchronization is estimated as systematic errors.

	Nov18	Nov19	Nov22
T+2nd (Target position)	540.7(0.5)	540.3(0.6)	540.1(0.5)
T only (Target position)	539.5(0.8)	538.9(0.9)	539.2(0.8)
T+2nd (beam dump)	620.1(0.2)	620.8(0.4)	623.7(0.2)
T only (beam dump)	620.3(0.3)	620.3(0.5)	623.9(0.3)

TABLE 3.4: Peak positions at the target and beam dump on each day. The peaks at the beam dump and at the target position were fit by the gaussian functions and their mean values are listed to study the synchronization of spectra with (T+2nd) and without the 2nd ring (T only).

3.5.3 Derivation of ratios for each day

Summarizing above we carried out following studies. We changed the start timing ($t_{\rm start}$) from 515 to 520 ns. At each time we changed the criteria of

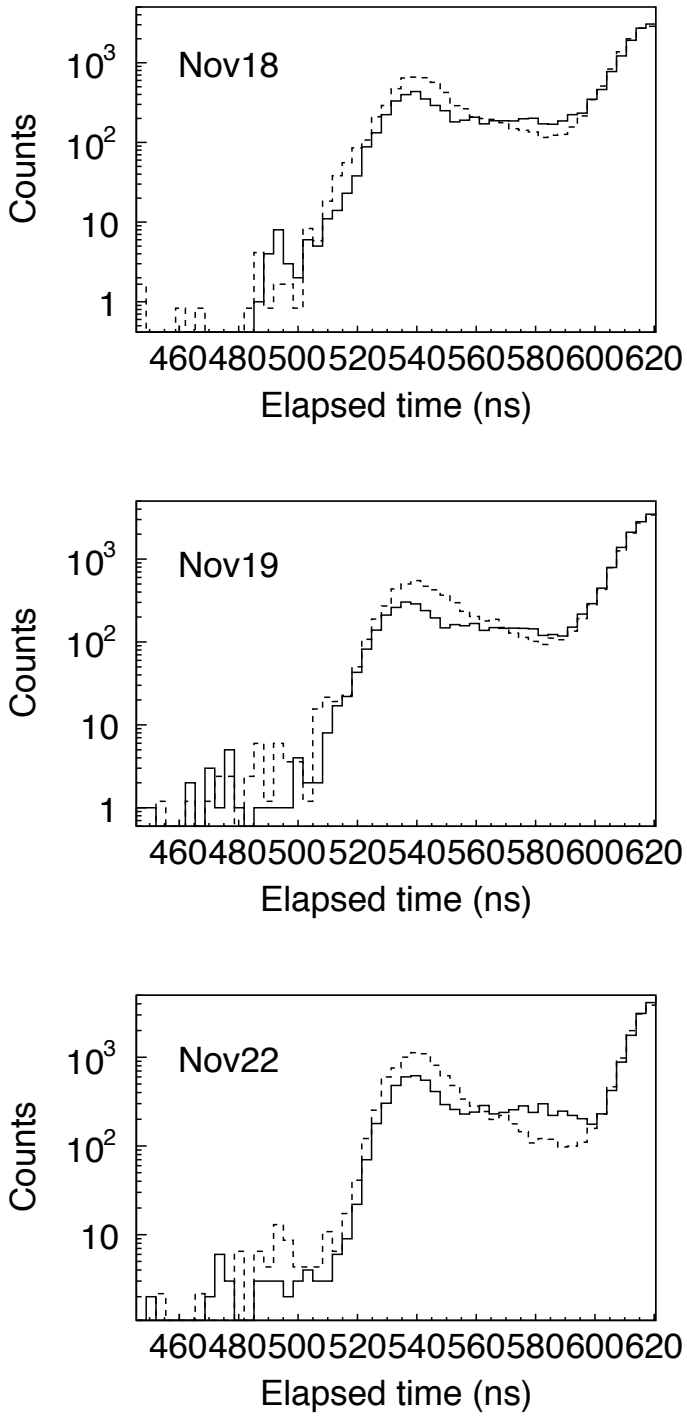

FIGURE 3.10: Normalized spectra in log scale to emphasize the rising edge of the spectra for each day

the dashed spectra for -1, 0 and +1 ns. Therefore we had three ratios for each timing, thus 18 points were calculated to study those uncertainties.

Fig. 3.11, 3.12 and 3.13 show the results. The horizontal axis shows the $t_{\rm start}$, the vertical axis represents the ratios ($\rm N_{anni}/N_{Ruth}$) on Nov18, Nov19 and Nov22. We found that the synchronization of $\pm$ 1 ns changed the ratio to a different value which can not be explained by its statistics. For example in Fig. 3.11, when the start timing was $t_{\rm start}$ was 517 ns the blue point and the other two points were not consistent within 1 σ. This is assumed to be caused by the unstable rising edge.

We evaluated the systematic error conservatively. For each day we took a mean value of these 18 points evaluated in a statistical way. In addition, we evaluated the difference of the ratio from the mean value to the farthest point. The difference was added as a systematical error. This made systematic error of $\sim$ 10% in maximum. In Table. 3.5 we represent the ratios for each day.

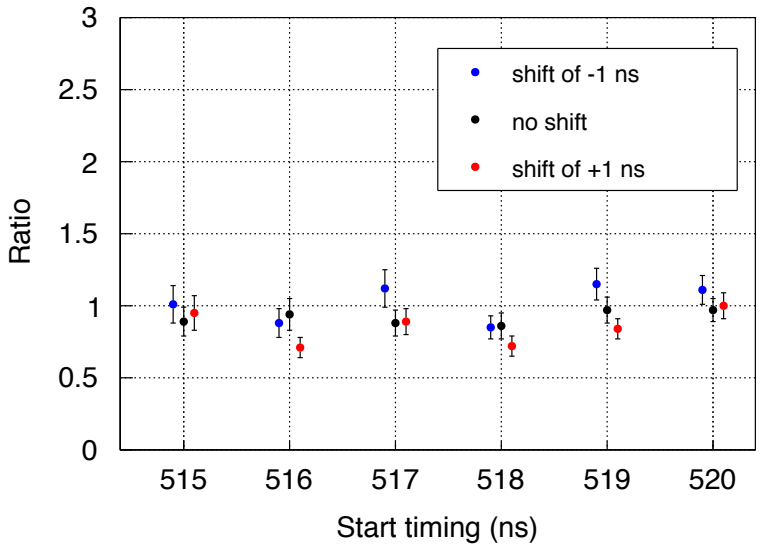

FIGURE 3.11: Fluctuations of the ratios ($\rm N_{anni}/N_{Ruth}$) on Nov18.

d

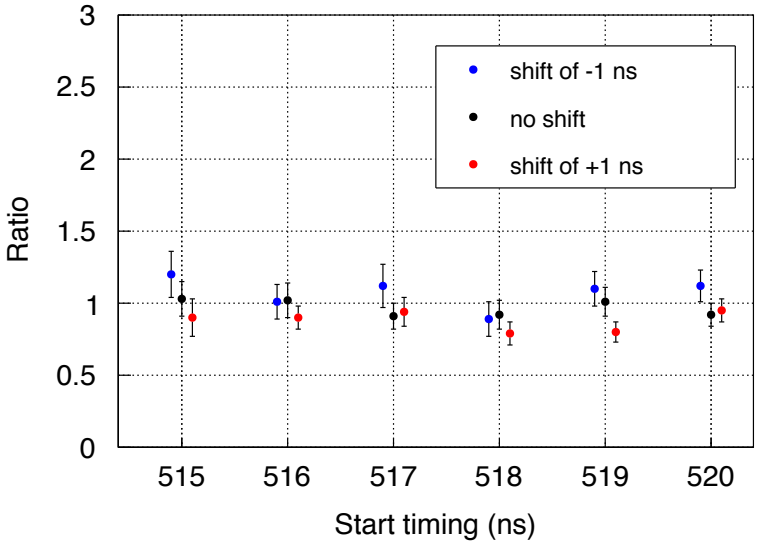

FIGURE 3.12: Fluctuations of the ratios (N_{anni}/N_{Ruth}) on Nov19.

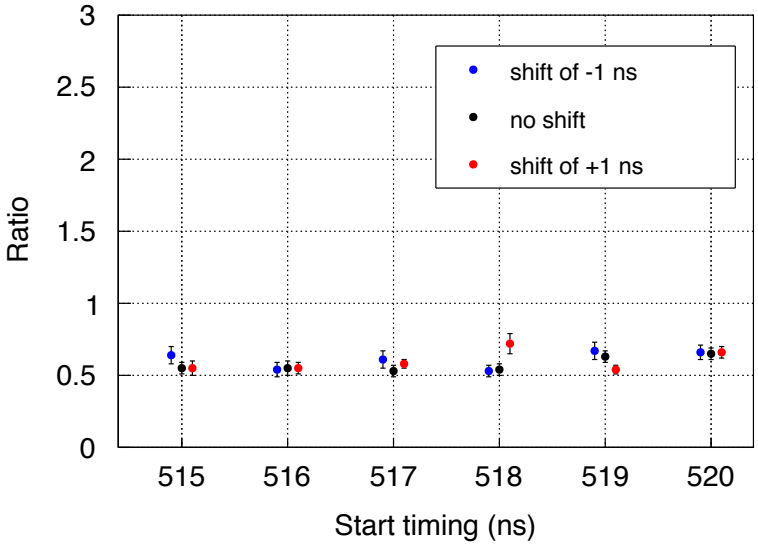

FIGURE 3.13: Fluctuations of the ratios (N_{anni}/N_{Ruth}) on Nov22.

	Ratio
Nov18	0.94±0.10(stat)±0.09(sys)
Nov19	0.98±0.10(stat)±0.08(sys)
Nov22	0.62±0.09(stat)±0.08(sys)

TABLE 3.5: The ratios of numbers of hits caused by annihilations on the 2nd ring ($\mathrm{N_{Ruth}}$) and on the target ($\mathrm{N_{anni}}$).

3.6 Antiprotons annihilated on the 2nd ring

The cross section of antiprotons scattered to the ring (σ_{Ruth}) was derived by the equation.

$$\sigma_{\mathrm{Ruth}} = \left(\frac{\mathrm{Z}\alpha\hbar\mathrm{c}}{2\mathrm{E}}\right)^2 \int \frac{\left[\cos\theta + \sqrt{1-(\frac{m}{M})^2\sin^2\theta}\right]^2}{\sin^4\theta\sqrt{1-(\frac{m}{M})^2\sin^2\theta}} d\Omega \tag{3.5}$$

In this equation, m and M represent masses of an antiproton and the carbon nucleus. Due to its symmetry around the axis of the beam trajectory, the formula can be rewritten as,

$$\begin{aligned} \sigma_{\mathrm{Ruth}} &= \left(\frac{\mathrm{Z}\alpha\hbar\mathrm{c}}{2\mathrm{E}}\right)^2 \int_{11.3}^{20.1} \frac{\left[\cos\theta + \sqrt{1-(\frac{m}{M})^2\sin^2\theta}\right]^2}{\sin^4\theta\sqrt{1-(\frac{m}{M})^2\sin^2\theta}} 2\pi\sin\theta d\theta \\ &= 1.46(\mathrm{barn}) \end{aligned} \tag{3.6}$$

The integration region for our experimental setup (distance from the target to the ring was 15 cm, and its inner diameter and outer diameter were 6 cm and 11 cm) was from 11.3 to 20.1 degrees.

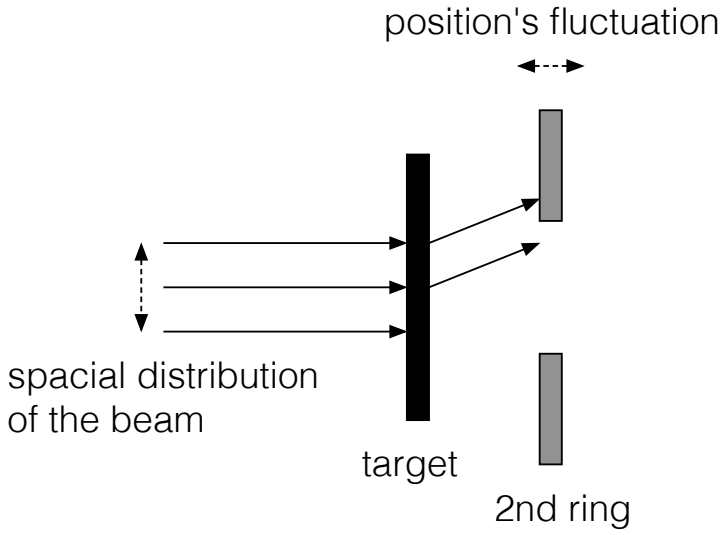

FIGURE 3.14: σ_{Ruth} can be derived numerically, but spatial distribution of the beam, uncertainties of positions of the target and the 2nd ring affected the σ_{Ruth} and introduced a systematic uncertainty.

3.7 Uncertainties associated to the elastic scattering

3.7.1 Spacial distribution of the beam

Eqn. 3.6 assumes a beam of small diameter passing through the center of the target. The actual beam has a finite size and may not pass through the target axis (Fig. 3.14). In order to evaluate this effect, spatial distributions of the beams were varied in a Monte-Carlo simulation, and changes of the number of hits on the ring were studied.

The spatial distributions measured by a GEM detector appear larger than they actually are due to multiple scattering of low energy ions in the vacuum window. The spatial resolution was tested by injecting a beam collimated to 3 mm; measured profile was 10 mm FWHM.

The spacial distribution of the beam which came into the target foil was measured by GEM45, which was just upstream of the target. Fig. 3.15

shows the horizontal and vertical distributions of the beam measured by GEM45. The distributions were fit with a Gaussians, the results of which are shown in Table. 3.6. The obtained standard deviations (sigmas) were typically 6 $\sim$ 7 mm, which implies that an actual size was $\sigma > 3$ mm. In addition the target position was downstream of GEM45, at the target position the sigma should be smaller since we focused the beam on the target position. Therefore we set the upper limit of the sigma of the beam to 3 mm and included it into simulations.

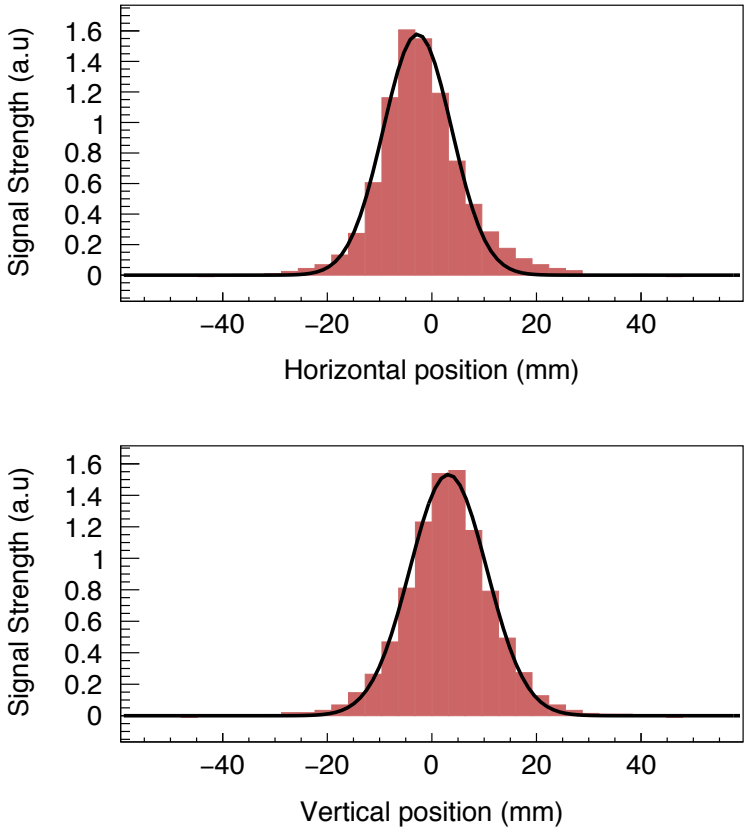

FIGURE 3.15: Horizontal and vertical positions and distributions measured by GEM45, which is just upstream of the entrance of the target chamber.

shot num	H-center (mm)	Hσ (mm)	V-center (mm)	Vσ (mm)
shot1	-0.17	6.78	-0.29	6.22
shot2	0.33	7.14	0.03	6.47
shot3	0.08	7.09	0.27	6.8
shot4	-2.6	6.43	4.0	7.2
shot5	-3.23	6.56	3.36	7.5
shot6	-2.7	6.56	3.14	7.37

TABLE 3.6: Measured positions and sigmas of the beam. H and V represent horizontal and vertical positions, and their one standard deviations (σ) were derived by fitting the obtained spectrum with a Gaussian function.

3.7.2 Validity of the Monte-Carlo simulation

The simulation was based on the Geant4 package [60]. At first we tested its validity and used it for the error estimations.

Geant4 has two libraries describing processes of the elastic scattering. One is G4MultipleScattering which describes the multiple scatterings. The library includes effects of the size of the target nucleus. As a comparison, the number of antiprotons scattered was calculated by using a simple formula of the Rutherford scattering (Eqn. 3.6). In the simulation a carbon target of 1 μm with the density of 2.0 g/cm^3 was used.

Those values are listed in Table. 3.7. Results with G4CoulombScattering follow the formula of the Rutherford scattering, while the number of hits with G4Multiple scattering do not since too few collisions would occur in a thin target of $\sim$ 1 μm. G4CoulombScattering was implemented to describe the elastic scatterings.

3.7.3 Estimation of uncertainties of the elastic scattering cross section

In the Monte-Carlo simulation the target and 2nd ring were reproduced and the beam which had a certain distribution was strike the target. The number of antiprotons scattered to the 2nd ring was investigated by changing the size

Implemented library	the number of hits on the ring (/$10^8\overline{\mathrm{p}}$)
G4MultipleScattering	1826
G4CoulombScattering	1489
Theoretical calculation	1484

TABLE 3.7: The number of antiprotons that scattered off the foil and strike on the 2nd ring. These values were estimated by simulations based on Geant4. Two types of libraries which describes the scatterings were compared.

in sigma of the beam from 0 to 3 mm, and changing the distance between a target and the 2nd ring from 14.86 cm to 15.14 cm. Table. 3.8 shows the maximum upper and lower uncertainties estimated in this way. The maximum upper error was obtained when the distance was 15.14 cm, and the sigma of the beam radius was 3 mm. The lower error was derived when the distance was 14.86 cm and the sigma was 0 mm. The derived error (6 %) was evaluated as an error associated to σ_{Ruth}.

Distance (cm)	Sigma (mm)	the number of hits (/$10^8\overline{\mathrm{p}}$s)
14.86	0.0	1446
15.14	3.0	1579
15	0.0	1489

TABLE 3.8: The number of antiprotons that elastically scattered and struck on the 2nd ring. The relationship between the number of hits on the ring and sigma(mm) of the Gaussian beam is shown.

3.7.4 Effects of scatterings via strong interactions

In the above sections we took care of only the Rutherford scattering, however we need to consider the contributions of the nuclear scatterings. However, the effects were assumed to be small comparing to the Rutherford scattering, especially in the case of scatterings at relatively forward angles. This is due to the fact that the imaginary part of the optical potential is larger than the real part, and the real part is almost negligible. For example

the black disk model, in which the target nucleus was treated as a complete black disk, does not the allow the nuclear scattering at the forward angle since when it close to the target nucleus it always absorbed the antiproton. Therefore we can assume that when antiprotons interact with nuclei via a strong interaction, they annihilate with surface nucleons for almost all the time.

A calculation of the nuclear scattering of an antiproton at 80 MeV/c on Be target was done by Andrea Bianconi in INFN. The result is shown in Fig. 3.16. The blue line represents differential cross section of the Rutherford scattering, and the blue line includes the scattering via the strong interaction additionally. The In the forward angle between 10 to 20 degrees like in our experiment, the contribution of the nuclear scattering was less than 1% thus it was negligible when it was compared to contributions from the Rutherford scatterings.

The calculation was carried out with the Be and one with a carbon target has not done. However, the optical potential used so far revealed that the real parts of the potential were negligibly small and almost same for all types of the target nuclei universally [2]. Therefore we expect that the contributions of nuclear scatterings would be small in the case of the carbon target too. In our experiment, we used the carbon target at the momentum of 100 MeV/c, therefore if we take into account the dependences of the Rutherford scattering on the momentum of the incident particle and the mass numbers of the target, the contributions of the nuclear scatterings becomes smaller in the case of the carbon target comparing to the beryillium target.

For these reasons, we concluded that the nuclear scatterings can be negligible and used only the Rutherford scattering formula to derive the σ_{Ruth}.

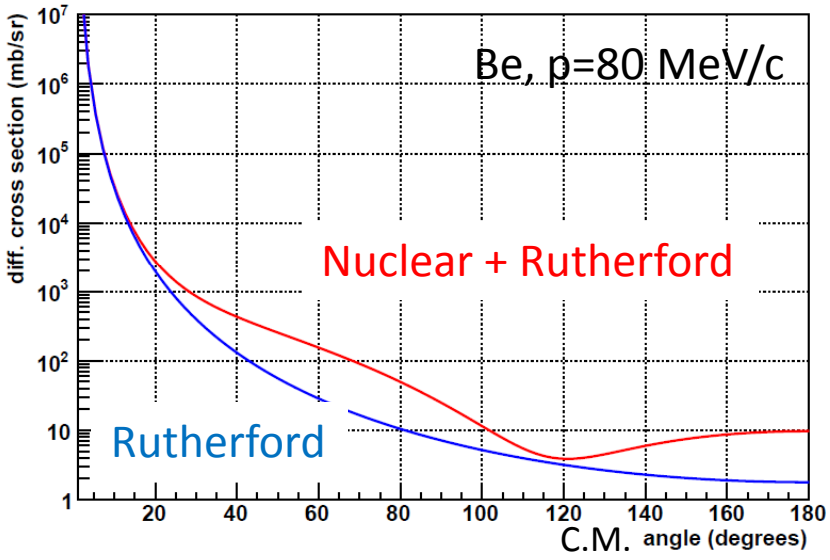

FIGURE 3.16: Rutherford and nuclear scattering of antiprotons at 80 MeV/c on Be target The blue line shows differential cross sections of the Rutherford scattering, and the red line represents both the Rutherford and nuclear scattering. This calculation was done by Andrea Bianconi in INFN.

3.8 Derivation of the cross section

The cross sections can now be derived by a following equation.

$$\begin{aligned} \frac{\mathrm{N_{anni}}}{\mathrm{N_{Ruth}}} &= \frac{\sigma_{\mathrm{anni}}}{\sigma_{\mathrm{Ruth}}} \\ \sigma_{anni} &= \frac{\mathrm{N_{anni}}}{\mathrm{N_{Ruth}}} \cdot \sigma_{\mathrm{Ruth}} \end{aligned} \tag{3.7}$$

$\mathrm{N_{anni}}$ and $\mathrm{N_{Ruth}}$ are listed in Table. 3.5. The elastic cross section was derived to 1.46(0.09) barn. These values were substituted in Eqn. 3.7, and the annihilation cross sections derived for each day are shown in Table. 3.9. In Table. 3.10 sources of the errors of the cross sections are listed. The error of normalizations by the Cherenkov signals was 2.3%, statistical error of $\mathrm{N_{anni}}$ and $\mathrm{N_{Ruth}}$ was 6%. Distributions of the beam caused an error 6% to the total error. The uncertainty of the t_{start} and synchronizations caused a systematic error of 10%.

Fig. 3.17 shows cross sections for each three day. The inner error represents statistical error and the outer error corresponds to the systematic error. A weighted average of three cross sections was applied to merge the data for statistic error, and the systematic error was just added to the total error. The cross section was derived to

$$\sigma_{\mathrm{anni}} = 1.21(0.31)\mathrm{barn}. \tag{3.8}$$

	Cross section (barn)
Nov18	1.37±0.15(stat)±0.24(sys)
Nov19	1.43±0.15(stat)±0.23(sys)
Nov22	0.91±0.13(stat)±0.23(sys)

TABLE 3.9: The ratios of numbers of hits caused by annihilations on the 2nd ring ($\mathrm{N_{Ruth}}$) and on the target ($\mathrm{N_{anni}}$).

Source	Uncertainty
Normalization of the spectra	2 %
Distribution of the beam	6%
Statistical error	6%
Uncertainties of t_{target} and synchronization	10%
Total	25%

TABLE 3.10: Sources of uncertainties of the annihilation cross section to derive cross sections for each day. The main source of the error was caused was caused by the uncertainty of t_{target} which related to the integration regions.

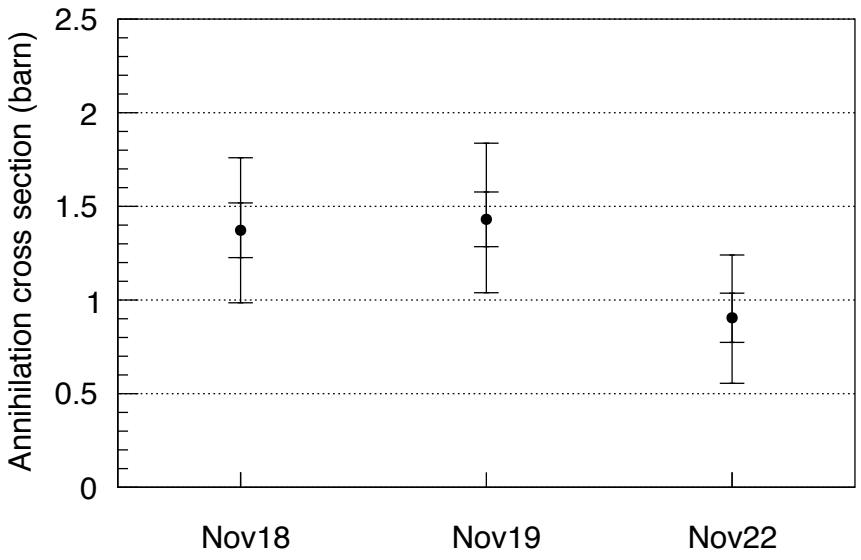

FIGURE 3.17: Annihilation cross sections derived for each day of the experiment. Exact values of each point are listed in Table. 3.9. The inner and outer error correspond to the statistical and statistical errors.

Chapter 4

Results and discussion

4.1 Annihilation cross section on carbon

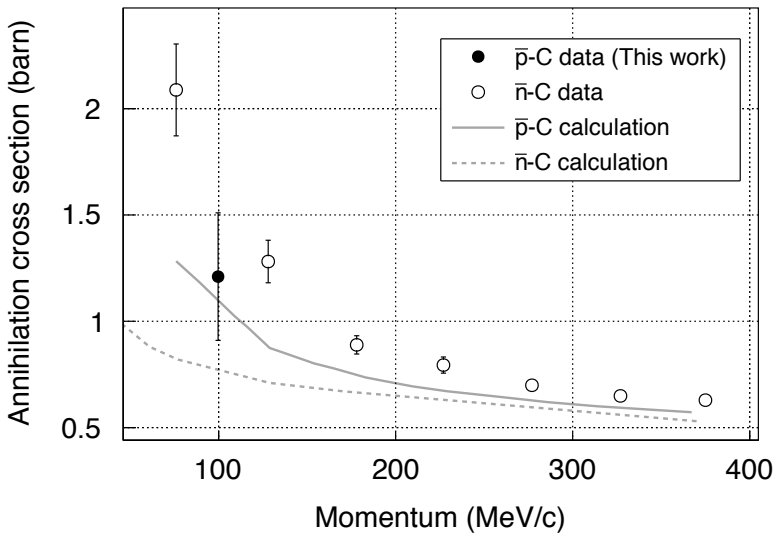

FIGURE 4.1: The $\overline{\mathrm{p}}$-annihilation cross section on carbon at 100 MeV/c, and comparisons to corresponding $\overline{\mathrm{n}}$-annihilation cross sections and theoretical calculations. The black circles represents the $\overline{\mathrm{p}}$-annihilation cross section, the white circles are $\overline{\mathrm{n}}$-annihilation cross sections, and theoretical calculation of $\overline{\mathrm{p}}$-annihilation cross section (a solid curve) and $\overline{\mathrm{n}}$-annihilation cross section (a dashed curve) are shown.

Fig. 4.1 represents the $\overline{\mathrm{p}}$-annihilation cross section ($\sigma_{\overline{\mathrm{p}}\mathrm{C}}$) on carbon at 100 MeV, and comparisons to corresponding $\overline{\mathrm{n}}$-annihilation cross sections ($\sigma_{\overline{\mathrm{n}}\mathrm{C}}$) and theoretical calculations. The black circles in Fig. 4.1 shows the

theoreticcal $\overline{\mathrm{p}}$-annihilation cross section on carbon obtained in this measurement. The white circles are $\overline{\mathrm{n}}$-annihilation cross sections. The solid line shows the theoretical $\overline{\mathrm{p}}$-annihilation cross sections based on the generalized optical potential. The dashed line corresponds to the theoretical $\overline{\mathrm{n}}$-annihilation cross section, which is also based on the same potential but without the Coulomb focusing effect.

The obtained $\sigma_{\overline{\mathrm{p}}\mathrm{C}}$ of 1.21 barn was consistent to the theoretical calculation within 1σ, and the optical potential well describes the result.

The $\sigma_{\overline{\mathrm{p}}\mathrm{C}}$ data is smaller than the $\overline{\mathrm{n}}$ data. This implies that the inversion observed in the case of Sn (Fig. 1.6) must also exist in the case of carbon. In the case of the antineutron, the theoretical calculation differ from the experimental by 5σ.

In this experiment, the obtained cross section had a large error of 30%, however within the error bar the cross section was consistent to the theoretical calculations. If the large enhancement of the antineutron data was caused by the strong interaction, it would be possible to see a same phenomena in the case of the our experiment since the antiproton and antineutron are isospin symmetry particles. This means that the $\overline{p}$ cross section would be ~ 5 barn. However the obtained cross section of the antiproton was 1.21 barn and differ from the such enhancement. It would be necessary to construct theories which just does not impose the reason of the enhancement to the strong interaction, but deals with the difference between the antiproton and antineutron, i.e, the difference of the charge. It is also necessary to take the antineutron data with different methods to confirm correctnesses of the past data.

The annihilation cross sections calculated by the optical potential, by the Black disk model and experimental data are shown in Table. 4.1. The theories agree with each other within 30%, and are consistent with the data obtained in this experiment. This also means that the assumption of the Black disk model in valid in this momentum region.

Optical potential	Black disk	Experimental result
1.10 barn	0.80 barn	1.21(0.31) barn

TABLE 4.1: The annihilation cross section of antiprotons on a carbon target at 100 MeV/c. Two different calculations based on the optical potential and the black disk model are shown. They are compared to the experimental value which was measured in this experiment.

4.2 Mass dependence of cross sections

The mass dependence of the $\overline{\mathrm{p}}$-annihilation cross sections at 100 Mev/c was studied by using the previous data the new result with carbon. For this the formula of the Black disk model of Eqn. 1.3 was used. Since Eqn. 1.3 derived by the Black disk model depends on the momentum of the incident antiproton, it becomes a geometrical cross section of the target nucleus in the high energy region.

In past studies, the mass dependence was studied by fitting the obtained data with the function $\sigma = \sigma_0 A^{\alpha}$, where σ_0 and α were parameters. However at 100 MeV/c, the contribution from the geometrical cross section and the Coulomb focusing effects are similar, and it is not possible to observe a clear A-dependence. Therefore the calculation with the Black disk model was directly compared to the experimental values. In order to describe the diffuseness of the target nucleus the radius of the target nucleus was parametrized as R = 1.84 + 1.12 $A^{\frac{1}{3}}$[2].

The mass dependence is shown in Fig. 4.2. Annihilation cross sections of Ni, Sn and Pt at 100 MeV/c [8] were indicated with white circles. The latest result of carbon was plotted together with a black circle. The dashed line corresponds to the calculation of the Black disk model. The past data had large errors of $\sim 50\%$, but the theoretical calculation describes the mass dependence well.

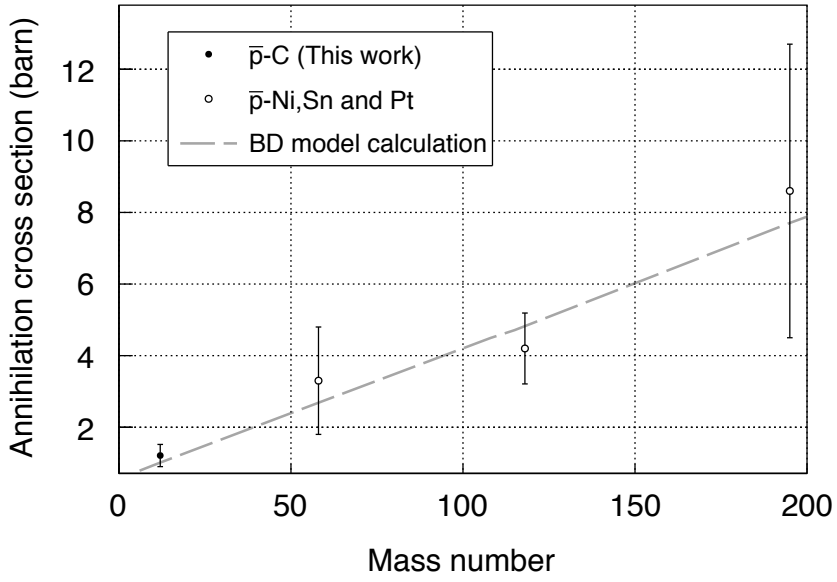

FIGURE 4.2: Mass dependence of $\overline{\mathrm{p}}$ annihilation cross sections at momentum 100 MeV/c. The cross section on carbon measured in this experiment is shown with a black circle. The data of Ni, Sn and Pt were taken from Ref. [8] and indicated by white circles. The cross section on carbon obtained in this experiment is also plotted, and they are compared to the theoretical curve according to the Black disk model.

4.3 Future outlook

The large systematic error of $\sim$ 25% was caused by the stabilities of the beam during the experiment. In order to deepen the discussion in this momentum region it is necessary to reduce the contribution.

The shape of the beam depended on the kicker timing, the lamp up timing of the AD and the super cycle of CERN. Especially at the rising edge, its shape and the amount of halo were affected by those effects strongly. Improvements of the beam shapes themselves will be difficult, and in spite of them the experimental method should be modified.

We propose to improve the target system to reduce the background. The manipulation arms used in this experiment needs $\sim$ 30 minutes to move in and out the target foils and 2nd ring for each operation. If we improve the system which can be operated automatically from the outside of the experimental area, and take the data with and without the 2nd ring one by one, the fluctuations of the beam shape during the data taking will be uniformed. This will reduce the systematic error about 10%.

The other systematic error was caused by the distributions of the beam and fluctuations of positions of each pulsed beam, and it was necessary to monitor it to obtain correct parameters to be input into Monte-Carlo simulations. However we used GEM based detector which made the distributions wider, and we had to use upper limits of the fluctuations and distributions as the input parameters, thus the systematic error is overestimated now. New non-destructive monitors, like ones used in the other ASACUSA experiment, will monitor the beam distributions with better resolutions. This will reduce the systematic error of 6 %.

Under these new conditions a measurement of the cross section with a precision better than 10% will be possible. Systematic data taking with other nuclei targets with such better accuracy will enable us to deepen the discussion of the antiproton annihilation cross sections at 100 MeV/c.

Chapter 5

Conclusion

A measurement of the $\overline{\mathrm{p}}$-annihilation cross section on carbon at 100 MeV/c was performed to study anomalous enhancement of the $\overline{\mathrm{n}}$-annihilation cross sections on some nuclei below 500 MeV/c. This experiment makes direct comparisons of experimental data of an antiproton and an antineutron possible.

Past measurements of $\overline{\mathrm{p}}$-annihilation cross sections were carried out with a tracking detector, but it suffered from difficulties of tracking the events correctly, and they had low statistics. At 100 MeV/c the annihilation cross sections on Ni, Sn and Pt were carried out but the errors associated to the obtained cross sections were $\sim$ 50 %. In our measurement we developed a method called "2nd frame method" which was dedicated to the cross section determination. A ring whose inner and outer diameters were 6cm and 11 cm was positioned downstream of the target foil. Some antiproton were scattered on the target and annihilated on the ring. Since the number of scattered antiprotons can be calculated by the usual Rutherford scattering formula, it is possible to derive the $\overline{\mathrm{p}}$-annihilation cross section from the ratio of the elastic scattering cross section measured in the same experimental setup. The emerging particles were detected with scintillation detectors developed and operated by a group of INFN in Italy.

The experiment was performed at the Antiproton Decelerator(AD) at CERN. For this experiment, the time width of the beam had to be narrower than usual $\sim$ 200 ns in order to reduce the background events caused by the annihilations at the lateral wall of the target chamber. A multiple extraction

mode was operated during the experiment, and by changing the timing of an AD's kicker a pulse width of $\sim$ 50 ns was achieved.

In order to normalize the spectra obtained with and without the 2nd ring, a Cherenkov counter was positioned close to the beam dump. It monitored the relative intensities of the antiproton beam. We developed a novel Cherenkov counter which aimed to monitor the intensities with a precision of a few percent. Photon yields of five types of radiators were studied and PbF2 crystals, which had the highest refractive index of 1.89 among those crystals, was selected. We tested two p-i-n photodiodes and an avalanche photodiode to study those behaviors against the antiproton pulsed beam. We found that the p-i-n photodiodes were saturated due to the nuclear counter effect which was caused by direct hits of charged particles to its depletion layers. Since the avalanche photodiode had a thinner depletion layer of $\sim$ 3 μm, and it had a function to multiply the number of Cherenkov photons via the avalanche amplification, the NCE was highly reduced.

The cross section of $\overline{\mathrm{p}}$ annihilation on carbon was derived as

$$\sigma_{\mathrm{anni}} = 1.21 \pm 0.31(\mathrm{barn}).$$

The $\overline{\mathrm{p}}$-annihilation cross section was consistent to theoretical calculations based on both the generalized optical potential and the Black disk model. The mass dependence of the cross section at 100 MeV/c was studied using the past data of Ni, Sn and Pt. Comparisons with the calculation based on the black disk model showed that it can reproduce the mass dependence at 100 MeV/c. However cross sections in the past experiment had large errors, so further study with data with better precisions is desired.

The error of the obtained cross section was improved by a factor of two comparing to the past measurements, and it is possible to apply the second frame method to other nuclei. Future experiments will be able to determine the cross sections with better precision, and the data will enable us to deepen the discussion of the comparisons and the study of its mass dependence.

Appendix A

OBELIX experiment

In this appendix, details setup of the OBELIX experiment are described. Its experimental setup is shown in Fig. A.1, and they measured annihilation cross section measurements of the antineutron listed in Fig. 1.1.

The OBELIX spectrometer was built as a multi-purpose detector used to detect both charged and neutral particles produced in antiproton-nucleus annihilations. It had been operated at CERN LEAR from 1991 to 1996. Experiments with this detector aimed to investigate antinecleon-nucleon dynamics and meson spectroscopy in the low momentum region [7, 61].

The detector in Fig. 1.4 consisted of 4 components. The most inner part was a barrel-shape array of 3 scintillators, $80 \times 3 \times 1$ cm^3. The other charged particles ($\pi^{\pm}$,K$^{\pm}$) produced in the annihilations were identified with a set of two Jet Drift Chamber (JDC), which tracked the charged particles and determined the annihilations' positions. An external barrel of scintillators identify the particle, especially neutrons by Time-Of-Flight (TOF) method. More details of the detector are shown in Ref. [7].

Inside the spectrometer a liquid hydrogen (LH_2) target was placed, and the antineutron was produced via a charge exchange reaction shown in the Eqn. 1.2. A sectional view of the target inside the OBELIX detector is shown in Fig. A.1. The LH_2 vessel was made by a cylinder of mylar, 175 μm thickness, with a diameter of 60 mm which was supported by a ring of stainless steel. The length of the target was 400 mm. As a result antineutrons which had continuous momenta were produced. A lead collimator selected only the antineutron which was emitted forward the target position.

A production rate of an antineutron was $\sim 36\ \overline{\mathrm{n}}\mathrm{s}/10^6\overline{\mathrm{p}}\mathrm{s}$. This low production rate makes the experiment more difficult statistically comparing to the measurements using antiprotons. Its momentum also have to be identified.

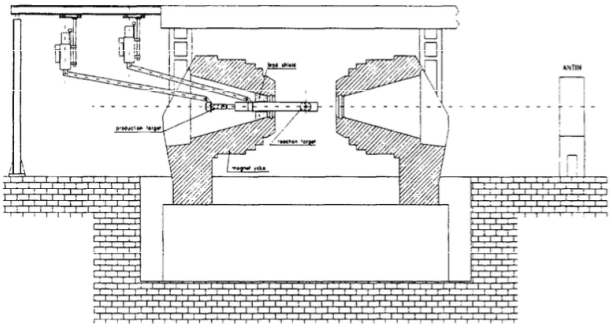

FIGURE A.1: A sectional view of the detector used for the OBELIX experiments. A cylindrical chamber represents a LH_2 target used for a production of $\overline{\mathrm{n}}$ beam via the charge exchange reaction. This figure is taken from Ref. [7].

The detector claims that contamination of antiprotons is not possible since they are stopped in the production target. In addition to that, they put additional materials (6 mm of scintillators, 5 mm of Pb and the reaction target) and it was hard to think that antiprotons could pass through all these materials. Other candidates making its background were $\pi^{\pm}$ and photons from π^0 decay, but its rate was estimated to 10^{-4}.

The momenta of the resulting antineutrons were from 80 MeV/c, which is a threshold momentum for the charge exchange reaction, to 400 MeV/c. Fig. A.2 shows the experimental momentum spectrum of antineutrons via the charge exchange reaction.

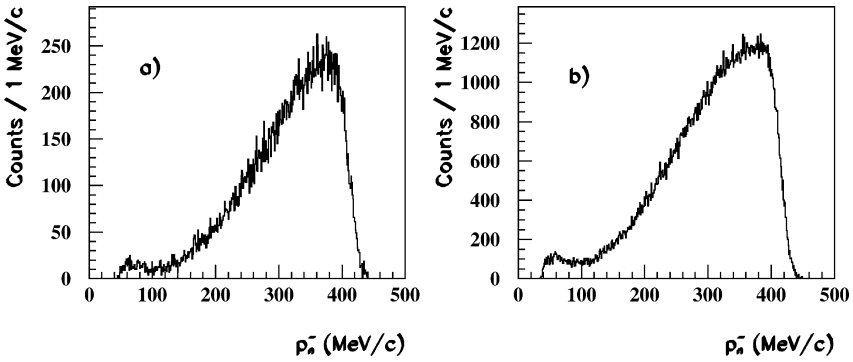

FIGURE A.2: Momentum distribution of the antineutrons obtained and measured by the OBELIX detector. Fig (a) shows a spectrum after corrections including resolutions and apparatus of the detector. Fig (b) shows raw spectrum. This figure is taken from Ref. [7].

Appendix B

Black disk model

The low energy Coulomb scattering was derived by Blair [25] which calculated a α-particle resonance. For strongly absorbed particle like antiprotons, the cross section can be approximately described by πR^2, which is a geometrical radius of the target. In addition, some partial waves which focused to the target nucleus by the Coulomb focusing effects are absorbed.

The equation of motion of antiprotons absorbed by the target nucleus can be written as a following.

$$E = \frac{mv_r^2}{2} + \frac{l^2}{2mr^2} - \frac{e^2}{4\pi\epsilon_0}\frac{Z}{r} \tag{B.1}$$

In Eqn. B.1, E is the energy of the incident antiproton, m is the mass of an antiproton, v_r is the velocity toward the target, l is the angular momentum, e is elementary charge, ϵ_0 is permittivity of vacuum, Z is the charge of the target nucleus and r is the distance between the antiproton and the target.

In quantum physics, the square of the angular momentum can be substituted by $\hbar^2 l(l+1)$. When the distance r becomes R which is the distance of closest approach, the v_r becomes 0. The angular momentum l becomes l_{max}, which is the largest number of angular momenta which is absorbed. $l_{\max}$ is typically ~ 10 when we calculate the cross section. Therefore, the Eqn. B.1 can be modified as below.

$$
\begin{aligned}
E &= \frac{\hbar^2 k^2}{2m} = \frac{\hbar^2 l_{\max}(l_{\max}+1)}{2mR^2} - \frac{e^2}{4\pi\epsilon_0}\frac{Z}{R^2} \\
l_{max}(l_{max}+1) &= \frac{2mR^2}{\hbar^2}\left(E + \frac{e^2}{4\pi\epsilon_0}\frac{Z}{R}\right) \\
&= \frac{2mR^2}{\hbar^2}\left(\frac{\hbar^2 k^2}{2m} + \frac{e^2}{4\pi\epsilon_0}\frac{Z}{R}\right) \\
&= (kR)^2\left(1 + \frac{Z\alpha\hbar c}{ER}\right) \qquad \text{(B.2)}
\end{aligned}
$$

In this equation we used $E = \frac{\hbar^2 k^2}{2m}$ and $\alpha = \frac{e^2}{4\pi\epsilon_0\hbar c}$.

On the other hand, the relationship between the annihilation cross section (σ_{anni}) and the angular momentum is a following [62][63].

$$
\sigma_{\text{anni}} = \frac{\pi}{k^2}\sum_{l=0}^{l_{\max}}(2l+1) = \frac{\pi}{k^2}\left(l_{\max} + \frac{1}{2}\right)^2 \qquad \text{(B.3)}
$$

By using Eqn. B.2 and Eqn. B.3 the σ_{anni} can be written as a following.

$$
\begin{aligned}
\sigma_{\text{anni}} &= \frac{\pi}{k^2}\left(l_{\max} + \frac{1}{2}\right)^2 \\
&= \frac{\pi}{k^2}\left(l_{\max}(l_{\max}+1) + \frac{1}{4}\right) \\
&\cong \frac{\pi}{k^2} l_{max}(l_{max}+1) \\
&= \frac{\pi}{k^2}(kR)^2\left(1 + \frac{Z\alpha\hbar c}{ER}\right) \\
&= \pi R^2\left(1 + \frac{Z\alpha\hbar c}{ER}\right) \qquad \text{(B.4)}
\end{aligned}
$$

The first term describes the geometrical cross section of the target nucleus, and the second term corresponds to the Coulomb focusing effect. In the momentum region above 100 MeV/c the cross section is dominated by the first term, and in the lower momentum region the second term becomes dominant.

In Eqn. B.4, the characteristics of nuclear density such as diffuseness and half radius are not included. They are taken into account by modifying the R in Eqn. B.4. The radius is calculated by using the following formula.

$$R = \frac{\int W(r)|\psi(\boldsymbol{r})|^2 r d\boldsymbol{r}}{\int W(r)|\psi(\boldsymbol{r})|^2 d\boldsymbol{r}} \tag{B.5}$$

where $\psi(\boldsymbol{r})$ denotes the $\overline{\mathrm{p}}$-nucleus scattering wave function scattering wave function as below.

$$\psi(\boldsymbol{r}) = \sum (2l+1)\frac{\psi_l(r)}{r} P_l(\cos\theta) \tag{B.6}$$

where $\psi_l(r)$ is a partial wave function and P_l is Legendre polynomial [2]. $W(r)$ is a function calculated by the optical potential as $W(r) = -\mathrm{Im}V_{\mathrm{opt}}(r)$.

The point is that we need to modify R by using the optical potential. Therefore the optical potential approach and the semi classical approach become identical at that point. The R calculated by using the Eqn. B.7 is described as a following.

$$R = 1.840 + 1.120A^{1/3}\mathrm{fm}. \tag{B.7}$$

Appendix C

Secondary particles

Branching ratios (%) for $\overline{\mathrm{p}}$ + p	
$2\pi^0$	0.0693±0.0043
nπ^0 (n≥1)	$4.1_{-0.6}{}^{+0.2}$
$\pi^+ + \pi^-$	0.307±0.013
$\pi^+ + \pi^- + \pi^0$	5.82±0.43
$\pi^+ + \pi^- + 2\pi^0$	9.3±3.0
$\pi^+ + \pi^- + 3\pi^0$	23.3±3.0
$\pi^+ + \pi^- + 4\pi^0$	2.8±0.7
$2\pi^+ + 2\pi^-$	6.9±0.6
$2\pi^+ + 2\pi^- + \pi^0$	19.6±0.7
$2\pi^+ + 2\pi^- + 2\pi^0$	16.6±1
$2\pi^+ + 2\pi^- + 3\pi^0$	4.2±1
$3\pi^+ + 3\pi^- + \pi^0$	1.85±0.15
$3\pi^+ + 3\pi^- + n\pi^0$ (n≥2)	0.3±0.1
$K^\pm + K^- + K^0$	0.237±0.016
$K^\pm + K^- + \pi^0$	0.237±0.015
$K^\pm + K^0 + \pi^\mp$	0.46±0.07
$K^\pm + K^0 + \pi^\mp + \pi^0$	0.47±0.06
$3\pi^+ + 3\pi^- + \pi^0$	0.3±0.1
$K^+ + K^-$	0.099±0.005

TABLE C.1: Secondary particles produced in a $\overline{\mathrm{p}}$ + p reaction,and their experimental branching ratios shown in percentages [32].

Branching ratios (%) for $\overline{\mathrm{p}}$ + n	
$\pi^- + n\pi^0$	16.4±0.5
(n≥1)	
$\pi^- + \pi^0$	∼0.8
$2\pi^- + \pi^+ + n\pi^0$	59.7±1.2
(n≥0)	
$2\pi^- + \pi^+$	3.4±0.2
$2\pi^- + \pi^+ + \pi^0$	17±2
$3\pi^- + 2\pi^+ + n\pi^0$	23.4±0.7
(n≥1)	
$3\pi^- + 2\pi^+$	4.2±0.2
$3\pi^- + 2\pi^+ + \pi^0$	15.1±1.0
$4\pi^- + 3\pi^+ + n\pi^0$	0.39±0.07
(n≥0)	

TABLE C.2: Secondary particles produced in a $\overline{\mathrm{p}}$ + n reaction, and their experimental branching ratios shown in percentages. [32].

Appendix D

Optical potential

D.0.1 tρ potential

An optical potential, so-called called tρ potential, has been used to discuss interactions between nucleus and hadrons, such as antiproton, pion and kaon. The potential is derived as followings. When a plane wave e^{ikr} is scattered by a particle which has no size (assuming that the size of the target is negligibly small), a wave function can be written as

$$\psi = e^{ikr} + f(\theta)\frac{e^{ikr}}{r}, \tag{D.1}$$

where ψ is the wave function, f(θ) is a scattering amplitude, r is the distance from the target position in the center of the mass frame. In the low energy region, the scattering amplitude can be substituted by s-wave scattering amplitude f_0. We next consider a scattering of a particle by medium consisting more than one particle, such as nucleus.By using an effective wave function $\psi_{\rm eff}$, which is an wave function at the scattering center perturbed by all surrounding scattering centers, the overall wave function can be written as a following.

$$\psi = e^{ikr} + \int \rho(\mathbf{r}')f_0\frac{e^{ikr}}{|\mathbf{r}-\mathbf{r}'|}\psi_{\rm eff}(\mathbf{r}'), \tag{D.2}$$

where ρ denotes the density of the scattering center. Applying ∇^2 to both side of Eq. D.2 and using the formula $\nabla^2\frac{1}{|\mathbf{x}-\mathbf{x}'|}$ = -4$\pi\delta(\mathbf{x}-\mathbf{x}')$, the following equation can be obtained.

$$(\nabla^2 + k^2)\psi(\mathbf{r}) = -4\pi f_0 \rho(\mathbf{r})\psi_{\text{eff}}(\mathbf{r}) \tag{D.3}$$

When only s-wave scattering is taken into account, the scattering amplitude f_0 can be substituted by a s-wave scattering length a_0. The effective wave function ψ_{eff} can be substituted by the incident wave function ψ in the Born approximation. If a modification ψ_{eff} from ψ can be put to the scattering length, the modified scattering length is named as a_0^{eff}, we obtain $\text{a}_0\psi_{\text{eff}}$ = $\text{a}_0^{\text{eff}}\psi$. Then Eq. D.3 can be written as a following.

$$(\nabla^2 + k^2)\psi(\mathbf{r}) = -4\pi a_0^{\text{eff}} \rho(\mathbf{r})\psi(\mathbf{r}) \tag{D.4}$$

$$\Leftrightarrow (\nabla^2 + k^2 + 4\pi a_0^{\text{eff}} \rho(\mathbf{r}))\psi(\mathbf{r}) = 0. \tag{D.5}$$

In Eq. D.5, the term $4\pi a_0^{\text{eff}} \rho(\mathbf{r})$ is a potential assuming that a_0^{eff} is a complex scattering length. This equation can be changed to the form of an usual Schroedinger equation can be obtained by dividing both sides of Eq. D.5 with $\frac{\hbar}{2\mu}$

$$V_{\text{opt}} = -4\pi \frac{\hbar}{2\mu} a_0^{\text{eff}} \rho(\mathbf{r}). \tag{D.6}$$

The potential V_{opt} is called tρ potential. This potential was extended to the form below in order to discuss isoscalar and isovector term of the potential.

$$2\mu V_{opt}(r) = -4\pi \left(1 + \frac{\mu}{M}\frac{A-1}{A}\right)[b_0(\rho_n + \rho_p) + b_1(\rho_n - \rho_p)] \tag{D.7}$$

where μ is the reduced mass of the antiproton, ρ_p and ρ_n are the neutron and proton density distributions normalized by the number of neutrons N and protons Z, A = N + Z, and M is the mass of the nucleon. $\left(1 + \frac{\mu}{M}\frac{A-1}{A}\right)$ is a factor to convert the system frame from the two-body CM system to the

$\overline{p}$-nucleus CM system. Earlier works showed that absorption of an antiproton is much larger than usual scattering, in other words the real part of the potential is negligibly small. An antiproton does not distinguish whether it annihilated with a proton or a neutron, this means that the isovector term, which related to a difference between a proton density distribution and a neutron's is negligible [6]. The Eqn. D.7 can be changed to

$$2\mu V_{opt}(r) = -4\pi \left(1 + \frac{\mu}{M}\frac{A-1}{A}\right) b_0(\rho_n + \rho_p)). \tag{D.8}$$

In order to describe ρ_p and ρ_n, a folded nuclear density distribution written as a following was used.

$$\rho_{(p,n)}(r) = \rho_{(p,n)0} \int \mathrm{d}^3\mathbf{r}' \frac{1}{\pi^{\frac{3}{2}} a_G^3} \frac{e^{-\frac{(r-r')^2}{a_G^2}}}{1 + e^{(r'-R)/a}}, \tag{D.9}$$

where a_G is a range parameter, R is the half radius of Woods-Saxon function and a is a diffuseness of the Woods-Saxon potential. $\rho_{(p,n)0}$ is a normalization factor determined by $\int \mathrm{d}^3\mathbf{r}\rho_{p,n} = A$, where A is the mass number of the target nucleus.

D.0.2 Validity of the potential

At first, the optical potential described above was applied for the antiprotonic atoms, where the total energy E<0, since there are sufficient data set. Then it was extracted to the scattering region where E>0 in order to calculate the annihilation cross sections of an antiproton. The parameters were adjusted to reproduce the results of the PS209 collaboration at CERN[6, 64].

It is known that a difference between proton and neutron radii affects strong-interaction level shifts and widths of $\overline{p}$ atoms. Assuming that the differences are parametrized by the following equation.

$$r_n - r_p = \gamma\frac{N-Z}{A} + \delta \tag{D.10}$$

where γ represents parameter describing dependence of the excess neutron skin. r_n and r_p correspond to radii of proton and neutron distributions. In order to describe ρ_p and ρ_n, two-parameter Fermi distributions are used [6, 24, 65].

Results of global fits to 90 data points obtained in the spectroscopy experiments of $\overline{p}$ atom are shown in Fig. D.1. The δ in Eq. D.10 was set to -0.035 fm. Three parameters, Reb_0, Imb_0 and a_G were adjusted for each value of the parameter γ of Eq. D.10, where a_G is the range parameter of a Gaussian.

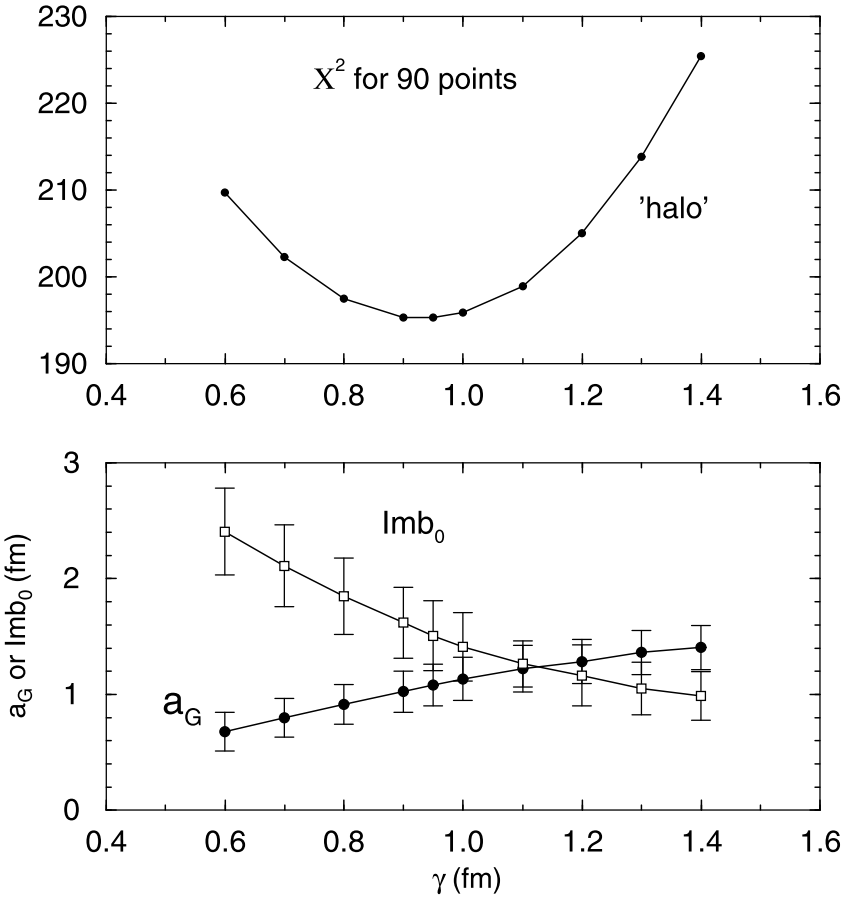

FIGURE D.1: Top: χ^2 values for 90 target nuclei as a function of γ (see text), bottom: Parameters Imb_0 and a_G obtained in this analysis. This figure is taken from Ref. [1].

D.0.3 Calculation of antiproton-annihilation cross sections

The annihilation cross sections of antiprotons were derived by calculating the phase shift δ_l for several partial waves which contributed to the total cross section. The annihilation cross section can be written as below.

$$\sigma_{\rm anni} = \frac{\pi}{k^2}\sum(2l+1)T_l \tag{D.11}$$

where k is the c.m. l is the number of a partial wave, and the transmission T_l is given by

$$T_l = 1 - \exp(-4{\rm Im}\delta_l). \tag{D.12}$$

Therefore in order to derive the annihilation cross section, the phase shift δ_l is necessary to be calculated. This δ_l is calculated numerically by using two Schrodinger equations. One is a Schrodinger equation in which a nuclear force derived by the optical potential affects a waveform. It is written as a following.

$$\left[\frac{\rm d}{{\rm d}r^2} - \frac{l(l+1)}{r^2} - V_{\rm Coulomb}(r) - V_{\rm opt} + k^2\right]\chi_l(r) = 0. \tag{D.13}$$

where $V_{\rm opt}$ represents the coulomb potential as described below.

$$V_{\rm Coulomb}(r) = -\frac{2\mu\alpha}{\hbar c}v_0\int_\infty^r {\rm d}r'\frac{1}{r^2}\int_0^{r'} 4\pi x^2\rho_{\rm charge}(x) \tag{D.14}$$

where μ denote the reduced mass of an antiproton and target nucleus. The equation was solved numerically and a numerical solution $\chi^{\rm Numerical}$ is derived.

When the wave function is at $r_{\rm max}$, where it is far enough not to be influenced by strong force of the target nucleus, the wavefunction can be solved analytically. A Schrodinger equation in this region is described as a following,

$$\left[\frac{\mathrm{d}}{\mathrm{d}r^2} - \frac{l(l+1)}{r^2} - V_{\mathrm{Coulomb}}(r) + k^2\right]\chi_l(r) = 0. \tag{D.15}$$

This equation can be solved analytically and the solution is described as a following,

$$\chi_l^{ana} = a_l^*(F_l(r)\cos\delta_l^* + G_l(r)\sin\delta_l^*) \tag{D.16}$$

where cofluent hypergeometric functions $F_l(r)$ and $G_l(r)$, a_l^* complex constant, δ_l^* is a complex phase shift and χ_l^{ana} is an analytical solution. By connecting these two solutions smoothly via the following equation, the phase shift can be derived.

$$\frac{1}{\chi^{\mathrm{Numerical}}}\frac{\mathrm{d}\chi^{\mathrm{Numerical}}}{\mathrm{d}r}|_{r=r_{\max}} = \frac{1}{\chi^{\mathrm{ana}}}\frac{\mathrm{d}\chi^{\mathrm{ana}}}{\mathrm{d}r}|_{r=r_{\max}} \tag{D.17}$$

Once parameters in the optical potential were determined at certain values, the phase shift and the annihilation cross section were determined automatically. Therefore, the annihilation cross section at a certain momentum region was derived by tuning those parameters in the optical potential to describe the cross sections in other momentum region, and extended it to a purpose region.

D.0.4 Annihilation cross section on carbon

At first, the parameters b_0, a_G were adjusted to reproduce the results of elastic scatterings of an 48 MeV antiproton on ^{12}C, ^{40}Ca and ^{208}Pb. As an example, differential cross section of an antiproton on ^{40}Ca fitted by the optical potential is shown in Fig. D.2. The resulting parameters were Reb_0 = (0.40 $\pm$ 0.04) fm, Imb_0 = (1.25 $\pm$ 0.05) fm and a_G = (1.34 $\pm$ 0.05) fm. The value of γ was set to 0.9 fm. potential was applied to 100 MeV/c where the experimental data of antineutrons exist, and Fig. 1.1 was made.

The tests of the calculations in the momentum region $\sim$ 100 MeV/c were carried out by using the existing data of antiprotons. Table. D.1 shows annihilation cross sections on Ne with corresponding momenta of the incident

antiprotons. Table. D.2 shows comparisons of annihilation cross sections on Ni, Sn, and Pt in the momentum region of 100 MeV/c with the calculation. In both tables the calculations well reproduce the experimental results.

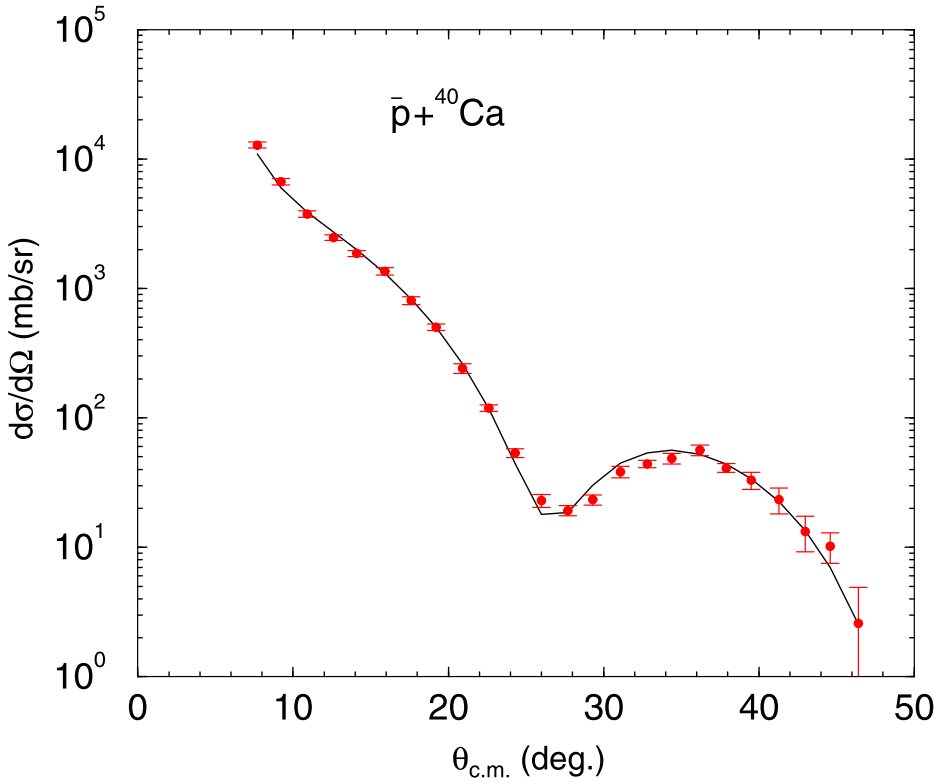

FIGURE D.2: Comparison between a calculation and experimental data of the elastic scattering of antiprotons of 48 MeV/c on the Ca target. This figure is taken from Ref. [1]

p_{lab} (MeV/c)	57	192.8	306.2	607.9
σ_{exp} (mb)	2210±1105	956±47	771±28	623±21
σ_{calc} (mb)	2760	1040	865	676

TABLE D.1: $\overline{p}$-annihilation cross section on Ne at various momenta

Target	Ni	Sn	Pt
σ_{exp} (mb)	3300±1500	4200±900	8600±4100
σ_{calc} (mb)	3170	5560	8620

TABLE D.2: $\overline{p}$-annihilation cross section on some nuclei at 100 MeV/c.

Appendix E

Multiplicity

A multiplicity is a type and the number of charged particles emerging from an antiproton-annihilation. In our measurement, the number of annihilations with a carbon target and with a stainless steel were necessary to be compared. The differences of each multiplicity needed to be compared.

The experiment was carried out by LEAR(Low Energy Antiproton Ring) at CERN. Antiprotons with a momentum of 200 MeV/c and an intensity of about $2\sim5 \times 10^4$ antiprotons/s were injected and stopped in following solid targets, ^{12}C, ^{27}Al, ^{28}Si, ^{40}Ca, ^{64}Cu, ^{92}Mo, ^{100}Mo, ^{108}Ag, , ^{165}Ho, ^{181}Ta, ^{197}Au, ^{209}Bi and ^{238}U. They used 5 scintillators positioned 144$\sim$271 cm from the target in order to detect charged particles. They also used other scintillators before and after the target. The time-of-flight from the target positions to the scintillators were used to monitor the energy of the beam. They detected emitted pions, kaons, protons, deuterons, tritons and neutrons.

The multiplicity of pions ($\pi^{\pm}$) is shown in Fig. E.1. Due to absorptions of emitted charged particles in the target, the multiplicity became smaller when the mass number increased. The multiplicities of other charged particles(kaons, protons, deuterons and tritons) also obeys to this behavior as shown in [40].

As shown in [39], the number of charged particles absorbed by a target can be parametrized by the solid angle of the target nucleus seen from the annihilation point. Eqn. E.1 describes the solid angle $\Omega(A)$ seen from the annihilation point. A is the mass number, δ = 2.3 fm is the diffuseness of the

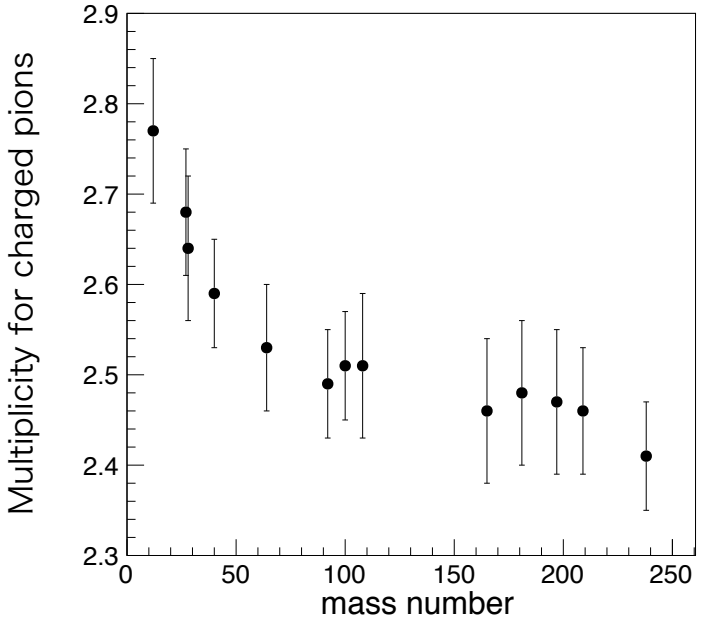

FIGURE E.1: Multiplicity for charged pions. Those data and this figure are taken from Ref. [38].

surface. r_0 is radius of the target, and it was assumed that the annihilation occurd at $r_0 A^{\frac{1}{3}} + \frac{1}{2}\delta$.

$$\frac{\Omega(A)}{4\pi} = \frac{1}{2}\left[1 - \sqrt{1 - \frac{A^{\frac{1}{3}}}{A^{\frac{1}{3}} + \frac{\delta}{2r_0}}}\right] \tag{E.1}$$

Using this solid angle the multiplicity $< M_{\pi\pm} >$ is given by

$$< M_{\pi\pm} > = < M_{\pi\pm}^{prim}\left(1 - \frac{\Omega}{4\pi}\right) > \tag{E.2}$$

with $< M_{\pi}^{prim} >$ = 3.1 is the number of particles emitted when an antiproton annihilated with a nucleon.

Appendix F

X-ray Photoelectron Spectroscopy

The composite of the eco-glass (S-TIH53W) was investigated by using a method called X-ray Photoelectron Spectroscopy (XPS) [66]. The experimental setup is schematically shown in Fig. F.1.

The XPS was carried out by injecting high energy X-ray to a sample material. The X-ray excite an electron at a certain energy level. The excited electron was emitted and we could observe an existence of a certain atom. The numbers of each atom can be identified by counting the numbers of emerging electrons, and observing their energies.

The XPS equipment in this measurement (JPS-9010MC) used $K\alpha$ ray ($h\nu$=1253.6 eV) of Mg as the incident X-ray. An incident electron was emitted from a heated filament and hit a magnesium foil. The emerging $K\alpha$ ray was used to excite the atoms in the sample material. When they de-excite an electron with a characteristic energy was emitted. The energies of those electrons were identified by an analyzer consisted of electrodes. Electrons were detected by a multi-pixel photon counter. By changing the voltage applied to the analyzer, the binding energy of the atoms were obtained.

We measured a composite of the eco-glass (S-TIH53W). As a reference the composite of an acrylic plate (CLAREX) was also shown. The acrylic plate is mainly made of carbon and oxygen, and clearly seen in Fig. F.2. The eco-glass was made of some other composites. It contained Ba, Ti and Nb not like the other usual artificial glasses.

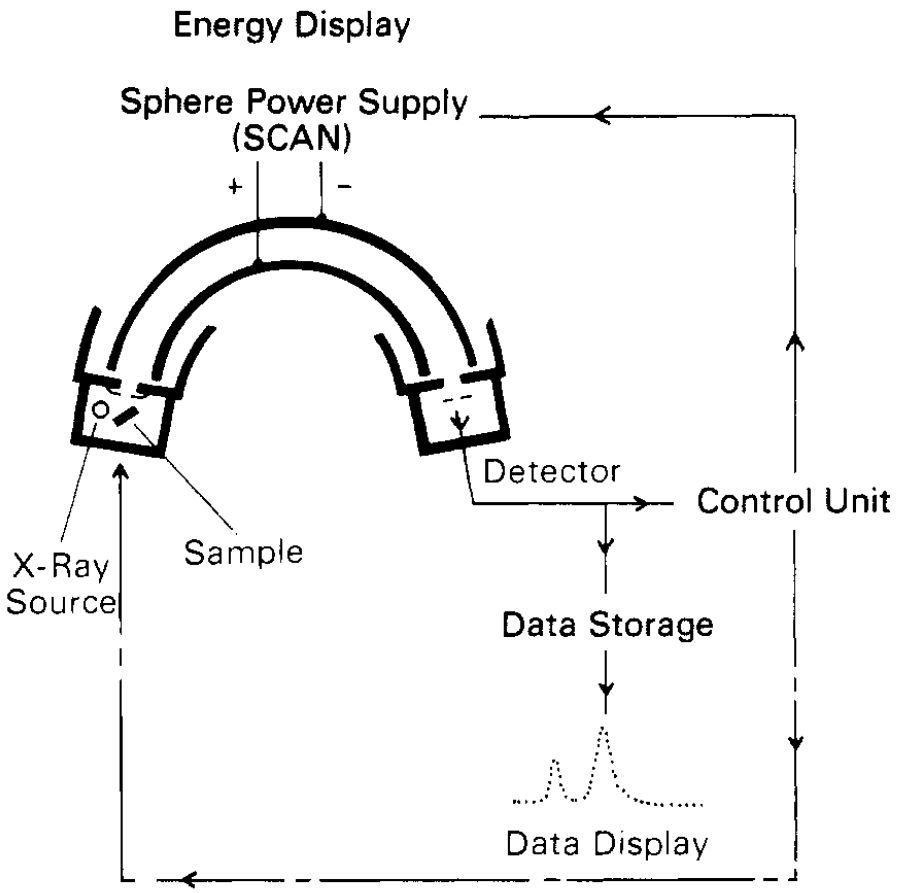

FIGURE F.1: Schematic layout of the X-ray Photoelectron Spectroscopy (XPS). This figure is taken from Ref. [66].

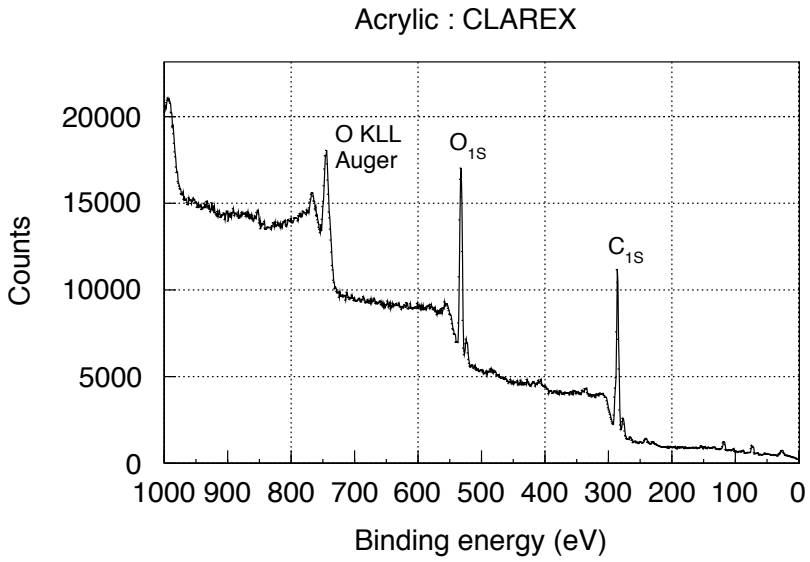

FIGURE F.2: Composites of CLAREX measured by the X-ray photoelectron spectroscopy.

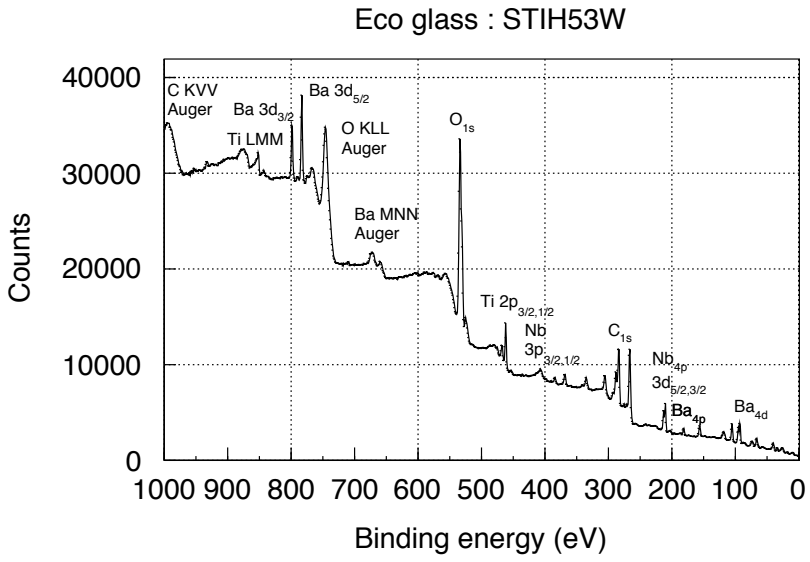

FIGURE F.3: Composites of the eco-glass (S-TIH53W) measured by the X-ray photoelectron spectroscopy.

Appendix G

Gain shift of the avalanche photodiode

Errors associated to the intensities measured by the Cherenkov counter were discussed in Chapter. 3. Here some plots which were used to determine each error were shown.

Fig. G.1 shows the relation ship between a temperature of the avalanche photodiode used in this experiment (S8664-1010) and its gain. Tis figure corresponds to the data when the avalanche photodiode was biased with 330 V. The black points were taken from a handbook of Hamamatsu-photonics G.1. The points were fitted by an exponential function which is described with a black solid line.

The temperature was controlled at 20 degrees with a fluctuation of 0.2 degrees, but a fluctuation of $\pm$ 0.5 degrees was used to estimate the error conservatively. The gain at 20 degree was 26.7, and it becomes 27.3 and 26.7 when the temperature becomes 19.5 degrees and 20.5 degrees. The error of 0.19 % was included in the total error of the beam intensity.

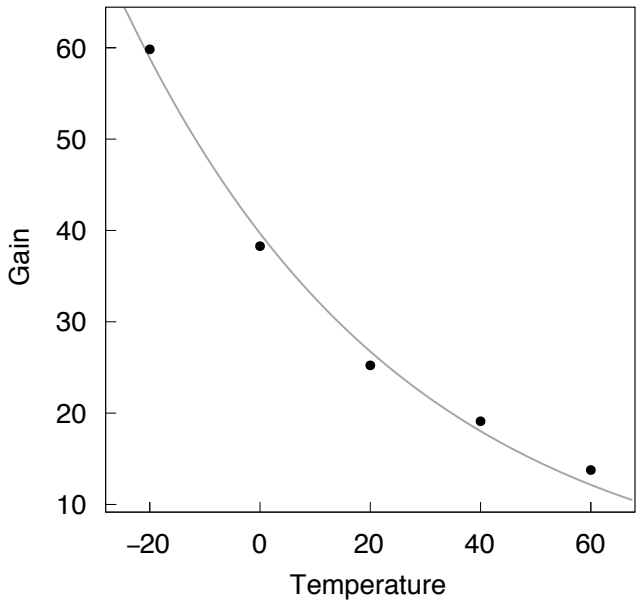

FIGURE G.1: Gain shift due to fluctuations of APDs' temperatures. The horizontal axis shows a temperature of an avalanche photodiode in this measurement (S8664-1010) and the vertical points show gain of each temperature. The black points were taken from a catalog of Hamamatsu-photonics [57]. The black points were fitted by an exponential function.

Bibliography

[1] E. Friedman. In: *Nucl. Phys. A* 925 (2014), pp. 141 –149.

[2] C.J. Batty, E. Friedman, and A. Gal. In: *Nucl. Phys. A* 689.3 (2001), pp. 721 –740.

[3] M. Astrua et al. In: *Nucl. Phys. A* 697.1 (2002), pp. 209 –224.

[4] F. Iazzi et al. In: *Physics Letters B* 475.3–4 (2000), pp. 378 –385.

[5] A. Antonelli et al. In: *Nucl. Phys. B* 517.1–3 (1998), pp. 3 –35.

[6] E. Friedman, A. Gal, and J. Mareš. In: *Nuclear Physics A* 761.3 (2005), pp. 283 –295.

[7] M Agnello et al. In: *Nucl. Inst. A* 399.1 (1997), pp. 11 –26.

[8] A. Bianconi et al. In: *Physics Letters B* 704.5 (2011), pp. 461 –466.

[9] W. Brückner et al. In: *Zeitschrift für Physik A Atomic Nuclei* 335.2 (1990), pp. 217–229.

[10] A Bertin et al. In: *Physics Letters B* 369.1 (1996), pp. 77 –85.

[11] A. Benedettini et al. In: *Nucl. Phys. B* 56.1 (1997), pp. 58 –65.

[12] A Zenoni et al. In: *Physics Letters B* 461.4 (1999), pp. 405 –412.

[13] A Zenoni et al. In: *Physics Letters B* 461.4 (1999), pp. 413 –416.

[14] T. Kalogeropoulos and G. S. Tzanakos. In: *Phys. Rev. D* 22 (11 1980), pp. 2585–2594.

[15] R. Bizzarri et al. In: *Il Nuovo Cimento A (1965-1970)* 22.2 (1974), pp. 225–250.

[16] A. Bianconi et al. In: *Physics Letters B* 492.3–4 (2000), pp. 254 –258.

[17] F. Balestra et al. In: *Physics Letters B* 149.1 (1984), pp. 69 –72.

[18] A. Bianconi et al. In: *Physics Letters B* 481.2–4 (2000), pp. 194 –198.

[19] Claude Amsler and Frank E. Close. In: *Phys. Rev. D* 53 (1 1996), pp. 295–311.

[20] Claude Amsler. In: *Rev. Mod. Phys.* 70 (4 1998), pp. 1293–1339.

[21] K. Nakamura et al. In: *Phys. Rev. Lett.* 52 (9 1984), pp. 731–734.

[22] D. Garreta et al. In: *Physics Letters B* 149.1 (1984), pp. 64 –68.

[23] M. Hori and J. Walz. In: *Progress in Particle and Nuclear Physics* 72 (2013), pp. 206 –253.

[24] A. Trzci ńska et al. In: *Phys. Rev. Lett.* 87 (8 2001), p. 082501.

[25] J. S. Blair. In: *Phys. Rev.* 95 (5 1954), pp. 1218–1222.

[26] V.F. Kuzichev, Yu.B. Lepikhin, and V.A. Smirnitsky. In: *Nuclear Physics A* 576.4 (1994), pp. 581 –602.

[27] P. Belochitskii, T. Eriksson, and S. Maury. In: *Nucl. Inst. B* 214 (2004). Low Energy Antiproton Physics (LEAP'03), pp. 176 –180.

[28] Ryugo S Hayano et al. In: *Reports on Progress in Physics* 70.12 (2007), p. 1995.

[29] S. van der Meer. In: *Rev. Mod. Phys.* 57 (3 1985), pp. 689–697.

[30] Helmut Poth. In: *Physics Reports* 196.3 (1990), pp. 135 –297.

[31] S Duarte Pinto et al. In: *Journal of Instrumentation* 7.03 (2012), p. C03001.

[32] M. Hori et al. In: *Nucl. Inst. A* 496.1 (2003), pp. 102 –122.

[33] H. Aghai-Kozani et al. "Limits on the antiproton-nuclei annihilation cross section at 125 keV, to be submitted". In: *EPJ, to be submitted* (2016).

[34] *New results of the antiproton-carbon annihilation cross section measurement at low energies, leap 2016, proceeding*. 2016.

[35] H. Aghai-Kozani et al. "Experimental Apparatus for Antiproton-Nucleus Annihilation Cross Section Measurements at Low Energy". In: *Leap 2016 proceeding* (2016).

[36] M. Corradini et al. In: *Hyperfine Interactions* 233.1 (2015), pp. 53–58.

[37] S. P. Møller et al. In: *Phys. Rev. Lett.* 88 (19 2002), p. 193201.

[38] D. Polster et al. In: *Phys. Rev. C* 51 (3 1995), pp. 1167–1180.

[39] J. Cugnon et al. In: *Phys. Rev. C* 63 (2 2001), p. 027301.

[40] J. Cugnon, P. Deneye, and J. Vandermeulen. In: *Nucl. Phys. A* 500.3 (1989), pp. 701 –730.

[41] P. Achenbach et al. In: *Nucl. Inst. A* 465.2–3 (2001), pp. 318 –328.

[42] Guohao Ren et al. In: *Journal of Crystal Growth* 247.1–2 (2003), pp. 141 –147.

[43] Guohao Ren et al. In: *Journal of Crystal Growth* 243.3–4 (2002), pp. 539 –545.

[44] P. Achenbach. In: *IEEE Transactions on Nuclear Science* 48.1 (2001), pp. 144–149.

[45] A Satpathy et al. In: *Nucl. Inst. A* 391.3 (1997), pp. 423 –426.

[46] C. L. Woody et al. In: *IEEE Transactions on Nuclear Science* 40.4 (1993), pp. 546–551.

[47] R.D. Appuhn et al. In: *Nucl. Inst. A* 350.1 (1994), pp. 208 –215.

[48] D.B. Cassidy and A.P. Mills Jr. In: *Nucl. Inst. A* 580.3 (2007), pp. 1338 –1343.

[49] Harrach. "Measurement of parity violating electron scattering on hydrogen". In: *Proposal for an experiment A4/1-93, Mainz Microtron MAMI* (2000).

[50] D.F. Anderson et al. In: *Nucl. Inst. A* 290.2 (1990), pp. 385 –389.

[51] A.T. Fienberg et al. In: *Nucl. Inst. A* 783 (2015), pp. 12 –21.

[52] Masaki Hori et al. In: *Nature* 475.7357 (July 2011), pp. 484–488.

[53] Masaki Hori et al. In: *Science* 354.6312 (2016), pp. 610–614.

[54] Masaki Hori. In: *Review of Scientific Instruments* 76.11 (2005).

[55] M. Hori. In: *Nuclear Instruments and Methods in Physics Research Section A: Accelerators, Spectrometers, Detectors and Associated Equipment* 522.3 (2004), pp. 420 –431.

[56] Hamamatsu Photonics. *Hamamatsu Photonics Si Photodiode Handbook Chapter 2*. Hamamatsu Photonics.

[57] Hamamatsu Photonics. *Si, APD, MPPC, Chapter 3*. Hamamatsu Photonics.

[58] W. Budde. "Multidecade linearity measurements on Si photodiodes". In: *Appl. Opt.* 18.10 (1979), pp. 1555–1558.

[59] Klaus D. Mielenz and Ken L. Eckerle. In: *Appl. Opt.* 11.10 (1972), pp. 2294–2303.

[60] I. Antcheva et al. In: *Computer Physics Communications* 182.6 (2011), pp. 1384 –1385.

[61] A. Adamo et al. In: *Nuclear Physics A* 558 (1993), pp. 13 –26.

[62] E Friedman and A Gal. In: *Nuclear Physics A* 658.4 (1999), pp. 345 –361.

[63] E. Friedman and A. Gal. In: *Physics Letters B* 459.1–3 (1999), pp. 43 –48.

[64] A. Trzcińska et al. In: *Nuclear Physics A* 692.1 (2001), pp. 176 –181.

[65] E. Friedman. In: *Hyperfine Interactions* 193.1 (2009), pp. 33–38.

[66] William E. Swartz. In: *Analytical Chemistry* 45.9 (1973), 788A–800a.

Acknowledgements

This thesis carries my name but would not be possible without guidances and supports from my friends and colleagues. The days with them are my fortunes I got in this five years.

First and foremost, I would like to express my sincere gratitude to Prof. R.S. Hayano, my supervisor. He gave me a number of opportunities to go abroad, see interesting things in foreign countries. Thanks to him I could start working as a member of the ASACUSA collaborations, and my experiences there made my world wider. During this five years, his overwhelming intelligence has been looked glowing for me.

I am deeply grateful to Dr. M. Hori for a countless number of valuable advices. It is not possible to thank him for all I got in this short space. I had seen his sincerity attitude and great passions toward the physics and science. It has been my ideal model as a scientist. He had not been carried out same experiment but always tried to introduce new methods and technics, and I learned that the science will not last without learning new technologies.

I would like to express my great thanks to my colleagues in Italy. First I would like to thank to Professor L. Venturelli. He allowed me to work for the antiproton annihilation cross section measurements. Thanks to him I got an experiment to work for the experiment from writing a proposal to the analysis. I would like to thank to V. Mascagna for his great helps concerning the analysis, preparing for necessary items for me extremely in a short time. I would like to all of the other colleagues, M. Corradini, M. Leali, and E. Lodi-Rizzini for their many helps and acceptance of me as a member of this antiproton annihilation experiment.

My gratitude goes to collaborators of the ASACUSA experiment who carried out spectroscopy-experiments of exotic atoms. I would like to thank to A. Soter in Max Planck Institute. She had been leading the antiprotonic and pionic helium experiment, and told us a number of experimental technics. Her brightness and friendliness were our pleasures. I also want to show my gratitude to H. Aghai-Hozzani, D. Barna and Andreas Dax. They

helped me in various ways when we worked at CERN and at PSI together. My poor english improved during the days with them.

I am deeply indebted to all of the members in the nuclear physics experiment (NEX) group in the university of Tokyo: Prof. R. S. Hayano, Dr. Takatoshi Suzuki, Dr. Masaharu Sato, Dr. Hideyuki Tatsuno, Mr. Yuya Fujiwara, Dr. Hexi Shi, Dr. Tadashi Hashimoto, Dr. Koichi Todoroki, Dr. Takumi Kobayashi, Mr. Hiroyuki Yamada, Mr. Yuni Watanabe, Mr. Hiroshi Horii, Mr. Takashi Ando, Dr. Hiroyuki Sakurai, Dr. Megumi Niikura, Dr. Zhengyu Xu, Dr. Nobuyuki Kobayashi, Mr. Ryo Taniuchi, Mr. Keishi Matsui, Mr. Takuya Miyazaki, Mr. Satoru Momiyama, Mr. Shunpei Koyama, Mr. Takeshi Saito, Mr. Shunsuke Nagamine, Dr. Kathrin Wimmer and Dr. Yosuke Watanabe for their kind supports. Among the members I would like to express special thanks to my Japanese colleagues who worked together at CERN. I would like to thank to Takumi Kobayashi. He gave me a lot of advices during my first two years. Thanks to his advices my life at CERN was comfortable. His sincere attitude toward physics impressed me. I am deeply grateful to Kochi Todoroki. It is not possible for me to thank to him enough. It is my great pleasure that I had my senior colleague who had been participated in the annihilation cross section measurements. I learned a lot about the experiment, and his advices always lead me to correct ways. Not only physics but also his kind personality had been my emotional support. I would like to express my deepest appreciation to Hiroyuki Yamada. We had been working at CERN and PSI for five years. It was fortune that I had a Japanese colleague who could alway share troubles and hard days together. I could not accomplish my works alone in an unknown foreign country.

Last but not least, I would like to express gratitude to my parents, Junichi and Hiroko, for their continuous supports and encouragements.